

ENGINEERED NEAR-INFRARED NANOMATERIALS FOR CANCER
THERANOSTICS: INTEGRATION OF PHOTOPHYSICAL COMPONENTS

By

AMIT KUMAR SINGH

A DISSERTATION PRESENTED TO THE GRADUATE SCHOOL
OF THE UNIVERSITY OF FLORIDA IN PARTIAL FULFILLMENT
OF THE REQUIREMENTS FOR THE DEGREE OF
DOCTOR OF PHILOSOPHY

UNIVERSITY OF FLORIDA

2011

© 2011 Amit Kumar Singh

To
The art of drawing bullseye around an errant arrow

ACKNOWLEDGMENTS

First and foremost, I thank my mentor and guide, Dr. Brij Moudgil for giving me an opportunity to work in an interdisciplinary environment at Particle Engineering Research Center (PERC). Directly and indirectly, he has taught me far more things than what can be articulated in this note of acknowledgement. Dr. Scott Brown additionally deserves acknowledgement to help me expose to multidisciplinary research environment. I thoroughly enjoyed working with him. I would like to thank my committee members Dr. Paul Holloway, Dr. Scott Perry, Dr. Chris Batich and Dr. Hugh Fan for their time and valuable inputs during the various stages of this research work. Special thanks to all PERC staff members: Jo-Anne Standridge, Greg Norton, Jamie Anders, Gill Brubaker, Gary Scheiffele, Donna Jackson.

Appreciation is extended to all past and present Moudgil, El-Shall group and Powers group members: Drs Parvesh Sharma, Vijay Krishna, Megan Hahn, Angelina Georgieva, Georgios Pyrgiotakis, Debamitra Dutta, Rhodney Guico, and graduate students Ajoy Saha, Mike Fenn without whose invaluable help, it would be very difficult to complete this work in time.

TABLE OF CONTENTS

	<u>page</u>
ACKNOWLEDGMENTS.....	4
LIST OF TABLES.....	8
LIST OF FIGURES.....	9
LIST OF ABBREVIATIONS.....	11
ABSTRACT.....	13
CHAPTERS	
1 INTRODUCTION.....	15
1.1 Scope of the Thesis.....	15
1.2 Cancer Nanotechnology.....	18
1.2.1 Towards Early Diagnosis.....	19
1.2.1.1 NIR fluorescence (NIRF) imaging / optical imaging.....	22
1.2.1.2 NIR fluorescence probes: current status.....	22
1.2.2 Towards Improved Therapy: Theranostic Nanoparticles.....	24
1.3 Biological Consideration of Theranostic Nanoparticles.....	27
1.4 Gap Analysis.....	28
1.5 Specific Objectives.....	30
2 MATERIALS, METHODS AND PROTOCOLS.....	32
2.1 Selection of Materials.....	32
2.2 Materials Used.....	33
2.3 Synthesis of Multifunctional Nanoparticles.....	34
2.3.1 Acid-Conjugated Dye Synthesis.....	34
2.3.2 Aminosilane Conjugated NIR-Dye.....	35
2.3.3 NIR Fluorescent Dye Doped Silica Nanoparticles.....	35
2.3.3.1 Microemulsion method.....	35
2.3.3.2 Sol-Gel synthesis.....	38
2.3.3.3 Mesoporous nanoparticle synthesis.....	39
2.3.4 Synthesis of Gold Speckled Silica Nanoparticles.....	40
2.3.4.1 Synthesis of dye doped silica core.....	41
2.3.4.2 Silica coating for prevention of quenching.....	41
2.3.4.3 Removal of ammonia from microemulsion.....	41
2.3.4.4 Gold coating on dye doped silica core.....	42
2.3.4.5 Separation of gold coated silica nanoparticles.....	42
2.3.5 Synthesis of Internally Gold Speckled Silica Nanoparticles.....	42
2.3.5.1 Gold encapsulation in silica nanoparticles.....	43

2.3.5.2	Reduction of gold-ammonia complex inside IGSS nanoparticles.....	43
2.3.6	Synthesis of Multiple Dye Doped Silica Nanoparticles	44
2.4	Particle Dispersion and Surface Conjugation.....	44
2.4.1	Amine Functionalization of Silica Surface.....	45
2.4.2	PEGylation of Gold Speckled Silica Nanoparticles	45
2.5	Performance Evaluation of Multifunctional Nanoparticles	46
2.5.1	Imaging Experiments.....	46
2.5.1.1	Confocal fluorescence imaging (<i>in vitro</i>)	47
2.5.1.2	Bioluminescence and fluorescence imaging	48
2.5.1.3	Photoacoustic imaging (<i>in vitro</i>)	48
2.5.1.4	Photoacoustic imaging (<i>in vivo</i>)	49
2.5.2	Photothermal Efficiency Measurements	50
2.5.2.1	Nanoparticles uptake quantification using flow cytometry	50
2.5.2.2	Photothermal ablation (<i>in vitro</i>)	51
2.5.2.3	Photothermal ablation (<i>in vivo</i>).....	51
2.5.2.4	Photothermal ablation using bioluminescence model	52
3	NIR DYE DOPED LUMINESCENT SILICA NANOPARTICLES	54
3.1	Research Approach	55
3.2	Results and Discussion.....	57
3.2.1	Particle Formation by Stöber Method	58
3.2.2	Particle Formation by Surfactant Template Method.....	60
3.2.3	Particle Formation by Reverse Micelles Method	61
3.2.4	Stability and Detection Limit of the Particles in Biological System.....	64
3.2.5	Tumor Targeting Using NIR Nanoparticles.....	65
3.3	Summary	65
4	PLASMONIC GOLD SPECKLED SILICA NANOPARTICLES	75
4.1	Photothermal Materials: Current Status and Limitations	75
4.2	Proposed Approach: Controlled Deposition of Plasmonic Materials	76
4.3	Controlled Deposition: Current Status.....	77
4.4	Controlled Deposition: A New Approach.....	78
4.5	Results and Discussion.....	79
4.6	Summary	83
5	APPLICATION OF GSS FOR OPTICAL IMAGING AND PHOTOTHERMAL THERAPY.....	91
5.1	Therapeutic Properties of GSS	92
5.1.1	Selection of Particle Size for Photothermal Applications	92
5.1.2	NIR Photothermal Ablation Properties of GSS(<i>in vitro</i>)	92

5.1.3	NIR Photothermal Ablation (<i>in vivo</i>).....	93
5.2	Optical Imaging Properties of GSS Nanoparticles	94
5.2.1	Photoacoustic Imaging	94
5.2.2	Photoacoustic Imaging: Limitations	96
5.3	Luminescent GSS Nanoparticles	96
5.3.1	<i>in vitro</i> Fluorescence Experiments.....	98
5.3.2	<i>in vivo</i> Fluorescence Experiments.....	98
5.4	Next Generation of GSS: Inverse Architecture for 3D Plasmon Coupling.....	99
5.5	Summary	102
6	NON-PLASMONIC PHOTOTHERMAL AND LUMINESCENT NANOPARTICLES	119
6.1	Non-Plasmonic Photothermal and Luminescent Materials.....	120
6.1.1	Incorporation of Optical Imaging Modality	121
6.1.2	Incorporation of Therapeutic Modality	122
6.1.3	<i>in vivo</i> Experiments	124
6.2	Summary	125
7	CONCLUSIONS AND FUTURE WORK	135
7.1	Conclusions	135
7.2	Suggestions for Future Work	140
	LIST OF REFERENCES	144
	BIOGRAPHICAL SKETCH.....	152

LIST OF TABLES

<u>Table</u>		<u>page</u>
1-1	Selected NP-based therapeutics approved or in clinical trials	31
4-1	Zeta potential of GSS nanoparticles	90
6-1	Effect of laser irradiation on different nahthalocyanine dyes	134

LIST OF FIGURES

<u>Figure</u>	<u>page</u>
3-1 Quantum yield of NIR dyes.....	67
3-2 Characterization of silica nanoparticles	68
3-3 Normalized quantum yield and fluorescence of nanoparticles.....	69
3-4 Absolute photoluminescence of silica nanoparticles.....	70
3-5 Fluorescence image of mice upon injection of nanoparticles	71
3-6 Comparison of photoluminescence of NIR dye doped silica nanoparticles with invitrogen QDs	72
3-7 In vivo demonstration of sensitivity of NIR dye doped nanoparticles with invitrogen QDs.....	73
3-8 Demonstration of in vivo targeting using TEM8 receptor	74
4-1 Characterization of GSS nanoparticles.....	85
4-2 Gold-silica composite nanoparticles synthesized by using different methods	86
4-3 Schematic demonstrating proposed GSS formation mechanism.....	87
4-4 GSS nanoparticles synthesized using different molarity of gold chloride solution	88
4-5 GSS nanoparticles synthesized using different amount of gold chloride solution	89
5-1 Particle size distribution of GSS nanoparticles	104
5-2 Increase in temperature of PEGylated GSS nanoparticles suspension in water.....	105
5-3 In vitro photothermal ablation	106
5-4 Photothermal ablation of tumor using GSS nanoparticles	107
5-5 Photoacoustic images of GSS nanoparticles in tissue like phantom	108
5-6 Photoacoustic imaging of mouse tumor.....	109
5-7 Fluorescence images of NIR dye doped silica nanoparticles	110

5-8	Confocal microscope images of A549 cells labeled with the FITC doped GSS nanoparticles.	111
5-9	Uptake of Pegylated GSS nanoparticles by breast cancer cells	112
5-10	Fluorescence imaging of mouse tumor after intratumoral injection of NIR GSS nanoparticles.....	113
5-11	TEM images of IGSS nanoparticles.....	114
5-12	Increase in temperature of nanoparticle suspension upon laser irradiation	115
5-13	Fluorescence spectra of NIR luminescent IGSS.....	116
5-14	Photothermal ablation and fluorescence imaging of IGSS nanoparticles	117
5-15	Quantification of bioluminescence signal.....	118
6-1	Normalized absorbance and fluorescence spectra of NIR fluorescent mesoporous silica nanoparticles.....	127
6-2	Characterization of MDT nanoparticles	128
6-3	Change in fluorescence and heating properties of MDT nanoparticles	129
6-4	Bioluminescence and fluorescence images of mice	130
6-5	Quantification of bioluminescence signal.....	131
6-6	Histological sections of tumor	132
6-7	Quantification of fluorescence signal	133

LIST OF ABBREVIATIONS

CT	Computed Tomography
DDS	Dye Doped Silica
FG	Fulminating Gold
FITC	Fluoresceine Isothiocyanate
FL	Fluorescence
GSS	Gold Speckled Silica
ICG	Indocyanine Green
IGSS	Internally Gold Speckled Silica
MDT	Multiple Dye Therapeutic
MNP	Multifunctional Nanoparticle
MRI	Magnetic Resonance Imaging
NIR	Near Infrared
NIRF	Near Infrared Fluorescence
NP	Nanoparticle
NPs	Nanoparticles
OI	Optical Imaging
PA	Photoacoustic
PAI	Photoacoustic Imaging
PAT	Photoacoustic Tomography
PDT	Photodynamic Therapy
PET	Positron Emission Tomography
PL	Photoluminescence
PTA	Photothermal Ablation
QD	Quantum Dot

SEM	Scanning Electron Microscopy
SPECT	Single Photon Emission Computed tomography
TEM	Transmission Electron Microscopy
TEOS	Tetraethylorthosilicate
US	Ultrasound

Abstract of Dissertation Presented to the Graduate School
of the University of Florida in Partial Fulfillment of the
Requirements for the Degree of Doctor of Philosophy

ENGINEERED NEAR-INFRARED NANOMATERIALS FOR CANCER
THERANOSTICS: INTEGRATION OF PHOTOPHYSICAL COMPONENTS

By

Amit Kumar Singh

May 2011

Chair: Brij Moudgil

Major: Materials Science and Engineering

Engineered nanomaterials hold great promise for the development of next generation nanomedicine, such as image-guided-therapy, early-stage-detection and therapeutic monitoring of diseases. Current research efforts are focused on the development and application of these nanomaterials for cancer treatment. The ultimate goal in this research field is to develop multifunctional nanoparticles (MNPs) that can specifically locate and selectively destroy cancer cells. The focus of present studies was on the development of engineered MNPs to overcome the limitations associated with mono-functional imaging and therapeutic agents. The MNPs were strategically engineered by integrating photophysical components such as fluorphores for optical imaging and photothermal materials for ablative therapy.

Molecular assembly of organic fluorophores was controlled inside an inorganic matrix to attain hybrid nanoparticles with enhanced optical properties. The high detection sensitivity of these near-infrared fluorescent (NIRF) nanoparticles (size 40nm) was demonstrated *in vivo* by fluorescence imaging at 10 time lower concentration than quantum dots. Surface modification strategies, involving functionalization of NPs (utilizing biotin-avidin chemistry) with small tumor targeting proteins, were employed to

deliver these nanoparticles to uniquely identified sites in tumor environment with ~10% efficiency.

Subsequently, these NIRF nanoparticles were modified to exhibit photothermal properties by integration of either photothermal materials within the NIRF particulate structure. Conventionally used plasmonic photothermal materials due to their size and shape restrictions could not be incorporated in the NIRF nanoparticles. A novel strategy based on interplasmon coupling between sub 4nm gold nanoparticles was developed to overcome this limitation. Surface of NIRF NPs was decorated either externally or internally with small gold nanoparticles in a controlled fashion (surface coverage 6-14%, size 0.7, 1.2, and 3.8nm). The gold speckled silica nanoparticles thus formed exhibited both optical luminescence and photothermal properties. Another strategy to incorporate photothermal properties in NIRF NPs was based on mixed micelles mediated synthesis of organic-inorganic hybrid structures. Molecular photothermal agents such as metal-naphthalocyanine dyes were incorporated inside the pores of NIRF NPs (photothermal: fluorescence dye 4:1). The high optical absorbance cross-section and optical imaging properties of MNPs were utilized for image guided photothermal ablation (tumor necrosis > 90%) of a human breast cancer tumor inside mice.

CHAPTER 1 INTRODUCTION

1.1 Scope of the Thesis

The future of medicine can be truly described by the prophetic science-fiction, *Fantastic Voyage*, published in 1966 by Isaac Asimov. Following is the excerpt from the most incredible adventurous thriller of that time:

“Four men and one woman reduced to a microscopic fraction of their original size, boarding a miniaturized atomic sub and being injected into a dying man’s carotid artery. Fighting their way past giants antibodies, passing through the heart itself, entering the inner ear where even the slightest sound would destroy them, battling relentlessly into the cranium. Their objective...to reach a blood clot and destroy it with the piercing rays of a laser gun. At stake...the fate of entire world.”

With several decades of advancement in nanotechnology, scientists have now begun to bridge the seemingly surreal gap between Asimov’s fiction and its realization. However, unlike Asimov’s top-down strategy, nanobiotechnologists are exploring bottom-up approaches for developing miniaturized submarines called nanoparticles to be sent for navigation into our bloodstream on vital health missions. These nanoparticles are being designed to evade immune system (white blood cells, antibodies etc.) while locating the diseased site by specific bio-recognition events during their voyage. Upon reaching the site of interest, the signal transmitted by these nanoparticles can reveal their position. Furthermore, like Asimov’s submarine these nanoparticles can be equipped to either repair or destroy the diseased cells upon external stimulus. After completing their task they would either disintegrate or escape through natural biological pathways, leaving the human body unharmed. The current

research efforts in this direction are focused on the treatment of cancer and it is envisioned that subsequent objective will be towards encountering the diseases like Alzheimer's.

The present studies were geared towards the engineering design of such nanoparticles for cancer treatment, utilizing photophysical properties of optically active materials. The current chapter of this dissertation provides an introduction to cancer nanotechnology along with the rationale of using optical nanomaterials for early stage diagnosis of cancer. The advantages of combining therapy with diagnosis are also discussed. The issues associated with conventionally used optical nanomaterials are analyzed followed by a gap analysis to put the current research efforts in perspective. Next, the specific objectives for this work have been outlined.

Chapter 2 presents a detailed description of the materials, methods and protocols used for the synthesis of nanoparticles developed during the execution of objectives outlined in chapter 1. Wherever necessary, brief descriptions of the underlying principles are provided. The protocols used for the demonstration of particles imaging and therapeutic properties are described in details.

It is well established now that for *in vivo* biological application of optical materials, their optical properties should lie within the near infrared region (NIR region: wavelength 650 nm – 900 nm) of electromagnetic spectra. In chapter 3, a brief overview of existing NIR optical probes and their limitations are discussed. The need for developing NIR dye doped nanoparticles is emphasized along with the justification for selecting new materials for their synthesis. It has been established that for increasing the photoluminescence of the particles, the dispersion of dye molecules and their

surrounding environment in the encapsulated state play a crucial role. Novel strategies for controlling the dispersion of dye molecules inside a silica matrix were developed to enhance the optical, photophysical and photochemical properties of the hybrid organic-inorganic nanoparticles. The ultra bright photoluminescence property of these nanoparticles was demonstrated by *in vivo* fluorescence imaging at ten time lower concentration than the current gold standard for optical imaging, quantum dots. Surface modification strategies were employed to deliver these nanoparticles to uniquely identified sites in tumor vasculature through active targeting.

The next step was to equip these nanoparticles with therapeutic modalities such as photothermal properties. Photothermal materials upon photoexcitation generate heat, thereby increasing the localized temperature high enough to destroy the cancer cells. However, due to the size and shape restrictions on conventionally used photothermal materials their integration within near-infrared fluorescent (NIRF) nanoparticles faced severe challenges. In order to overcome this limitation, a novel approach based on interplasmonic coupling between sub 4 nm gold nanoparticles was developed (chapter 4). A new method for the synthesis and controlled deposition of nanometer size gold on silica nanoparticles was developed and employed successfully to impart photothermal properties to NIRF nanoparticles. In addition, due to the absorbance properties of gold, the composite nanoparticles can be imaged using several other methods making these nanocomposites multimodal. One such method is photoacoustic imaging that was used to demonstrate the detection capability of these nanoparticles in addition to fluorescence imaging properties. Detailed discussion on *in vivo* application of these particles for multimodal imaging and therapy is presented in Chapter 5.

Although size tunable nanoparticles designed in this work could potentially enhance the tumor accumulation and targeting efficiency due to size selectivity, their distribution inside the complex tumor architecture remain uncertain. Ideally, therapeutic agents should be dispersed in such a way that their effect can be experienced homogeneously by all the cells present in the tumor. The limited mobility of these nanoparticles inside tumor due to their relatively large size (compared to molecular probes) and hydrophilic nature could limit their otherwise well established therapeutic potential. In order to overcome this limitation of plasmonic nanoparticles, a different type of nanoparticle that can be used as a carrier vehicle for the delivery of molecular photothermal agents at the site of interest is needed. Upon reaching the desired site such as tumor, the release of molecular therapeutic agents could be triggered to cover at least entire tumor region. In Chapter 6, based on the knowledge developed so far, the design and synthesis of non plasmonic photothermal nanoparticles equipped with fluorescence imaging is described. These particles were tested *in vivo* for image guided therapy applications. The conclusions and the significance of this research work along with recommendations for future work are presented in Chapter 7.

1.2 Cancer Nanotechnology

Over the past quarter century as a result of fundamental research in cancer biology new details of how cancer develops are being unraveled. However, clinicians lack the technological tools to utilize these findings for cancer detection, therapy and ultimately prevention. The major stumbling block remains the ability to detect tumor at an early stage in spite of the discovery of several molecular biomarkers that are known to express specifically on tumor cells¹. The advent of nanotechnology in cancer research has significantly enhanced the efforts for early stage detection of diseases².

Cancer research is becoming more and more reliant on nanotechnology augmented bioimaging for the diagnosis of diseases, the identification of physiological abnormalities, and the selection of therapeutic interventions. Nanoparticle-based contrast agents are quickly becoming valuable and potentially transformative tools for enhancing medical diagnostics for a wide range of *in vivo* imaging modalities. Compared with conventional molecular scale contrast agents, nanoparticles (NPs) promise improved abilities for *in vivo* detection and potentially enhanced targeting efficiencies through prolonged circulation times, designed clearance pathways, and multimeric binding capacities. Several nanomaterials are being investigated as suitable contrast agents for different imaging modalities to detect diseases at early stages through identification of molecular targets³. In addition to imaging alone, nanoparticles are prominently being developed for simultaneous tumor imaging and therapy⁴⁻⁶. These multifunctional nanoparticles (MNPs) serve both as a contrast enhancement agent and as a mediator for providing localized therapy, commonly utilizing photothermal ablation (PTA). In the next sub-sections role of nanotechnology in early diagnosis as well as in localized therapy is described.

1.2.1 Towards Early Diagnosis

The potential of X-rays for medical diagnosis was realized soon after their discovery by William Rontgen in 1895. The advancement of X-rays based imaging techniques was continued for next several decades and resulted in the development of computed tomography (CT), an indispensable tool for medical imaging. During this period other imaging techniques e.g. MRI, ultrasound and nuclear imaging (PET, SPECT) based on different physical principles have been developed. These imaging modalities have been employed clinically and in research to visualize the anatomical

structures and to obtain information about the physiological function of various tissues and organs. The continuous development in the field of medical imaging is enabling the detection of diseases at earlier stages than ever before. There is a need for earlier detection and characterization of disease development and determining treatment effectiveness, rather than the end effects of disrupted molecular processes (e.g., malignant cancers and metastases). In an attempt to understand the development of diseases and evaluation of the effect of therapeutic interventions, the research in bioimaging has recently become more focused on the visualization of cellular and molecular activities in real time for an intact organism. However, commonly used imaging modalities such as CT, US and MRI are not suitable for the direct observation of these processes at the desired level, due to the high (millimolar) concentration requirement for the contrast agents employed for these imaging modalities. Currently, nuclear imaging techniques, with their femto to pico molar sensitivity, remain the only clinically used modality for molecular imaging applications. However, issues related to the half-life of radionuclide limits the use of nuclear imaging for applications such as long term tracking of imaging probes. Other drawbacks include high cost, limited accessibility and logistical considerations associated with radionuclide. Moreover, only one molecular target can be detected at a given time (lacks multiplexing)⁷.

In order to overcome the limitations associated with nuclear imaging techniques, researchers have recently started developing *in vivo* optical imaging techniques that are capable of molecular imaging applications. Optical imaging is a rapidly growing field for the advancement in noninvasive *in vivo* imaging of biological processes at cellular and molecular level^{8,9}. The most distinguishing aspect of optical imaging is its non-invasive

nature and extremely high femto molar detection sensitivity. The wavelength dependent interactions of light generate contrast in an image by means of various mechanisms based on differences in absorption, scattering and fluorescence between sample and background. Recently fluorescence based optical imaging has emerged as a major technique for bioimaging due to the extensive research on fluorophores enabling fast, sensitive and reliable non-invasive study of large number of biological processes¹⁰. Fluorescence imaging is a powerful molecular imaging technique, wherein certain probes (i.e., fluorophores) are excited by incident radiation usually in the visible or NIR and emit energy at usually lower energy than that with which it was excited. Despite its extremely high sensitivity to detect and visualize the localization of individual cells, mRNA, DNA, proteins, peptides, receptors, low-expressing cellular markers, and epitope distributions, it lacks the ability to provide anatomical resolution. In fact, its resolution is limited to 2-3 mm. However, fluorescence and autofluorescence thoracoscopic and endoscopic techniques are emerging as powerful diagnostic tools for identifying disease and abnormal structural features on body cavity surfaces. Different information like spectra, quantum efficiency, lifetime and polarization obtained from fluorescence microscopy can be used to monitor the chemical and dynamical properties of the system of interest. Owing to the high signal to noise ratio, ultra low concentration of samples can be analyzed using fluorescence microscopy. Fluorescence imaging is emerging as powerful diagnostic tool for the identification of diseases and abnormal structural features on body cavity surfaces^{7,11-13}. For *in vivo* noninvasive imaging, fluorescence in the visible region is used only for thin tissue samples; the requirement

for deeper penetration depths for most clinical applications is driving fluorescence based techniques into the NIR region (650-900 nm)¹⁴⁻¹⁷.

1.2.1.1 NIR fluorescence (NIRF) imaging / optical imaging

In the NIR window, the absorption of water, hemoglobin, and lipids are at their minimum, autofluorescence and tissue scatter is low, with light penetration at its maximum; therefore, low signal-to-noise ratios (SNRs) and sensitive detection limits are achievable. Typically less than 1 cm, light penetration depth depends on what type of tissue is being imaged: skin and muscle are more transparent than organs having lots of vasculature (e.g., liver and spleen) due to hemoglobin absorption. The fluorophores must be bright with preferably large Stokes shifts and high fluorescence quantum yields in the NIR region, photostable, and resistant to degradation in biological systems. Currently used NIR fluorescence probes and their limitations are described in the next section.

1.2.1.2 NIR fluorescence probes: current status

Organic dyes are the most versatile molecular labels for their use in visible range, however, their poor photostability and extremely low quantum yield in the NIR region severely limits their use for *in vivo* applications. In spite of the availability of various cyanine or cyanine based dyes there is a limited use of these dyes for *in vivo* systems due to low water solubility, low photostability and extremely low quantum yield¹⁸. Moreover, these dyes tend to lose their fluorescence property upon exposure to harsh chemical environment such as those encountered inside tumor.

Quantum dots are the most preferred class of fluorescent probes for cellular and molecular imaging because of their small size, high molar absorption coefficient, high photostability, and large Stokes shift. However, several shortcomings limit the use of

quantum dots particularly for long term *in vivo* applications. Inherent cytotoxicity, low fluorescence quantum yield in aqueous environment and difficulties in surface functionalization are among the primary limitations for the use of quantum dots^{19,20}.

In order to overcome the limitations imposed on quantum dots a different class of nanomaterials, called dye doped silica (DDS) nanoparticles (FloDots²¹ and Cornell Dots²²) were developed by several groups. These biocompatible DDS nanoparticles, were synthesized by incorporation of dye molecules in silica matrix^{23,24}. For these nanoparticles, covalent incorporation of dye is generally preferred as it eliminates the possibility of dye leaching out in a biological medium. Encapsulation of a large number of dye molecules in a nanoparticle matrix results in enhanced optical properties thereby provides an opportunity to further increase the sensitivity and contrast in imaging. Silica surface is highly hydrophilic and amenable to surface modification using well established silane chemistry.

Covalent encapsulation of NIR absorbing dyes within silica matrix has been experimentally challenging due to the harsh chemical environment encountered during the synthesis of nanoparticles (NIR dyes generally possess poor chemical stability). Also, there are limited number of reports on the incorporation of NIR dyes in the silica matrix, the most common choice for such incorporation being Indocyanine green, a FDA approved dye²⁵. However, in absence of conjugation sites, ICG is mostly incorporated either by physical encapsulation or by electrostatic attraction between negatively charged dye and a positively charged matrix²⁶. These methods although result in the successful incorporation of ICG, the overall photoluminescence of the particles remains extremely low²⁵.

1.2.2 Towards Improved Therapy: Theranostic Nanoparticles

In addition to merely imaging, theranostic NPs are prominently finding their way into cancer research; they provide the diagnostic capability using an imaging modality to detect a tumor, while also facilitating localized therapy, commonly utilizing photothermal ablation (PTA) or photodynamic therapy (PDT). PTA works by exciting a NP with a large absorption cross section (e.g., gold) causing localized heating that may kill the tumor cells. Nanoparticle-mediated photothermal ablation of tumors is an important non-invasive treatment methodology that offers advantages over conventional therapeutic procedures (e.g., radio frequency, radiation therapy, conventional chemotherapeutics) by providing the ability to perform site-selective localized therapy—thus greatly minimizing toxic side effects. Engineered nanomaterials having near infra red (NIR) absorption are being actively developed and pursued for cancer therapy²⁷⁻²⁹ by photothermal ablation as they provide more efficient and selective photothermal effects. Novel nano-constructs such as carbon based materials (carbon nano tubes), gold (spherical, nanorods, nanocages, agglomerates, hollow, polyherdal) and composite materials (silica gold nanoshells, SPIO-nanoshells, Fe₃O₄-gold nanorods) have provided a fresh impetus to this area of research³⁰⁻³⁴. Amongst these, gold based nanomaterials have attracted particular attention due to their size and shape dependent plasmonic properties that allow them to absorb and scatter light in the visible to NIR region. Additionally, due to prevalent use of gold-based compounds in medicine (e.g., chrysotherapy), the benign toxicity profile of nanoparticles and some ongoing clinical trials gives them high possibility could lead to their approval for clinical applications. Moreover, the well established bio-conjugation strategies of gold permit necessary surface modifications to bind specific ligands (peptides, antibodies, aptamers,

polyethylene glycol, ligand) for their targeted delivery to the diseased site and to enable rapid clearance of non-targeted particles.

Gold nanoshells surrounding a silica core have been used in photoablative therapies, and an approach using optical coherence tomography (OCT) in combination with PTA has been used with gold nanoshells and nanocages. Iron oxide NPs with a gold shell allow for combined MRI and PTA. Additionally, single wall carbon nanotubes (SWCNTs) have been used for PTA. Imaging strategies utilizing high absorption cross section of gold NPs are likely to see tremendous growth in the future, as gold nanoshells are already in clinical trials for cancer therapy. The uptake/monitoring of gold nanoparticles has been done using a variety of approaches such as those based on their absorbance properties (e.g., reflective confocal microscopy, multi-photon Plasmon resonance microscopy, optical coherence tomography (OCT) including phase sensitive OCT, scattering, diffused optical spectroscopy) as well as through radiolabeling (e.g., positron emission tomography) and conventional microscopic techniques for optical imaging.

Another approach for achieving localized therapy is by performing photodynamic therapy (PDT) at the location of tumor. This method uses photosensitizers that, when excited by light, react with molecular oxygen in the biological environment to produce reactive oxygen species (ROS), which are cytotoxic to cells. Weissleder et al. have developed a multifunctional NP combining MRI, NIRF, and PDT. If the photosensitizer requires visible excitation, two-photon absorption is an option to increase the penetration depth of the excitation source. Even x-rays can be utilized as the energy required for PDT: researchers have applied lanthanide-based materials and porphyrins

with PDT derived from x-ray bombardment, which releases UV photons. Gold NPs can also be applied as radiosensitizers at realistic doses with low energy x-ray sources; originating from these ionizing x-rays, Auger electrons directly cause single- and double-stranded breaks in DNA or produce free radicals when interacting with water molecules, both resulting in local inactivation of tissue and cells.

Theranostic NP probes can be used as the therapeutic itself (e.g., gold nanoshells) or simply as the drug delivery vehicle (e.g., liposomes). One material that may prove useful in combining a dual imaging and therapeutic motif is mesoporous silica NPs; with their large surface areas and pore volumes, one modality can be incorporated into the silica matrix while loading the other modality into its pores. This approach has already been realized with an optical imaging agent and an anticancer drug. NP therapeutics can revive drugs that were previously discontinued because of toxicity or solubility issues, and have the potential to mitigate side effects of the free drug by delivering it directly to the site of interest. By encapsulating a concentrated drug payload, NPs can prevent exposure of healthy cells to the cytotoxic drug molecules and may prove more beneficial (e.g., lower toxicity and fewer side effects) at lower doses than the free drug.

Reviews on nanomaterials used for multimodal imaging and theranostic applications can be found by Kim et al³⁵. and Jarzyna et al³⁶. Table 1-1 summarizes information about NP-based imaging agents and therapeutics either approved or in clinical trials. Additional information can be found in articles by Adisheshaiah et al.³⁷ and McNeil³⁸. Although, a wide variety of imaging and photothermal ablation experiments have been performed using aforementioned nanomaterials, combining both properties

in a single nanoconstruct remained challenging. For example, gold nanoparticles could not be combined with fluorescence imaging probes due to quenching of fluorescence in the proximity of metals. Currently used absorption based imaging methods, used to image gold nanoparticles, left many biologically relevant questions unanswered. For instance, there is lack of information about the quantity of cellular uptake, dosimetry response, movement of particle within cells in *in vitro* studies and establishing distribution of the particles in the tumor vasculature, capillaries, within the necrotic zone, etc., in *in vivo* systems³⁹. For comprehensive investigations of these or other materials in biological systems it is essential to track and image the particles at all times. This could imply monitoring particle uptake at the cellular level, tissue (delivery) and/or the whole body levels. In context of photothermal ablation studies, one of the main limitations of these materials is the ability to image the particles in the tumor region post treatment, delivered either by systemic delivery or by direct intratumoral injections. In addition, some of the above mentioned approaches for imaging require specialized instruments for investigations. New materials are required to overcome these limitations enabling particle monitoring utilizing widely available instrumentation for the advancement of nanoparticle-mediated photothermal therapies to clinical applications.

1.3 Biological Consideration of Theranostic Nanoparticles

Important considerations when developing a theranostic probe are routes of delivery and bioavailability. Most delivery routes now consist of intravenous injection; therefore, circulation time is a crucial parameter to optimize. The functionalized NPs must be able to pass through the bloodstream and reach their desired target intact. The necessary functionalization of their surfaces may result in NPs that are larger than their “core” components, especially if very thick shells of silica, PEG, or polymers are used to

render them well dispersed in aqueous solutions. This size increase may be crucial depending on the type of cancer, stage of cancer, location of tumor, and vasculature permeability. Steric interactions of these larger NPs may allow for only a small fraction of them to bind to the target, as well as affect bloodstream circulation: passing through thicker veins or arteries is much different than passing through thinner capillaries.

In addition to intravenous administration, intramuscular injections, oral, transdermal, and inhalation routes are also possible, depending on the desired target (Table 1-1). The NPs being used must be able to survive their particular route of delivery; for example, oral routes require particles that can withstand the highly acidic environment of the stomach. If a region of the brain is the desired target, the NP agent must be able to cross the blood–brain barrier if administered intravenously. Any loss of biological activity of the component conjugated to the NP surface must be determined. The probe will not be effective if it cannot perform the deliver function or bind properly to the desired target. In addition, NPs must remain intact until they reach the tumor site and then perform the desired task—issues that will require further research and development.

1.4 Gap Analysis

Several kind of optical nanomaterials are under investigation as potential contrast agents for *in vivo* fluorescence imaging^{40,41} and as photothermal agents⁴²⁻⁴⁴. These materials share a common property that they need to be photoexcited to accomplish the desired task and their optical properties should remain in NIR region of electromagnetic spectra. Although these materials can be engineered to have the desired NIR optical properties they lack the size tunability. In other words, for a given optical property (e.g., absorption or emission at 600 nm versus 800 nm), the nanomaterials size or shape

must be changed to obtain the desired characteristic; for example, the shape of a gold nanoparticle must be changed to obtain an absorption of 600 nm compared to 800 nm, while a change in the size of a QD is necessary to obtain an emission of 600 nm vs. 800 nm. In all likelihoods different applications would require different size and shape of nanoparticles. For example, preferred size for applications requiring renal clearance is less than 7 nm^{45,46}, on the other hand particle uptake by tumor cells is high for gold nanoparticles in the size range of 30-50 nm⁴⁷⁻⁴⁹.

As mentioned earlier, nanomaterials available for NIRF optical imaging suffer from either poor optical properties (organic dyes) or are inherently toxic (quantum dots)⁵⁰. The optical properties of organic dyes can be enhanced by their encapsulation in a nanoparticle matrix²⁴. However, the poor chemical stability of NIR dyes such as ICG (Indo cyanine green)¹⁸, results in the degradation of dye during its incorporation in a matrix- due to the harsh chemical environment used during synthesis of nanomaterials. Consequently, achieving optical image guided therapy by integration of fluorophores with plasmonic materials has faced severe challenges. Moreover, quenching of fluorescence by metallic surface also needs to be resolved. As a result, currently used approaches for incorporating fluorescence in plasmonic materials have made the already complicated synthesis protocol even more complex. The size of overall nanoparticle increased beyond their ability to harvest nanoscale properties such as enhanced size dependent uptake and renal clearance. The limited diffusivity due to the larger size of these nanoconstructs may also limit their dispersion inside complex tumor architecture thus compromising the effectiveness of photothermal therapy. Although the notion of image guided therapy using nanoparticles having both optical imaging and

photothermal ablation properties was conceptualized long time ago⁵¹, to date its realization in an *in vivo* system remains elusive⁵².

1.5 Specific Objectives

The overall objective of the present study was “*select and design nanoparticles that integrate NIR photophysical components for enhanced optical properties for biological applications.*” The major tasks to achieve this objective are as follows:

1. Development of size/shape independent nanoparticle system for optical fluorescence imaging.
2. Development of size / shape independent nanoparticle constructs for photothermal ablation therapy.
3. Integration of above two features in a single nanoparticle system without compromising the properties of individual system.
4. Performance assessment in above mentioned systems to validate the design strategy.

Table 1-1. Selected NP-based therapeutics approved or in clinical trials^{38,53}

Product	Nanoparticle Drug Component	Delivery Route	Indication	FDA Status	Company
Doxil	PEGylated liposome/doxorubicin hydrochloride	IV	Ovarian cancer	Approved 11/17/1995 FDA050718	Ortho Biotech
Amphotec	Colloidal suspension of lipid-based amphotericin B	Subcutaneous	Invasive aspergillosis	Approved 11/22/1996 FDA050729	Sequus
Estrasorb	Micellar NPs of estradiol hemihydrate	Topical emulsion	Reduction of vasomotor symptoms	Approved 10/9/2003 FDA021371	Novavax
Macugen	PEGylated anti-VEGF aptamer	Intravitreal	Neovascular age-related macular degeneration	Approved 12/17/2004 FDA021756	OSI Pharmaceuticals
Abraxane	Nanoparticulate albumin/paclitaxel	IV	Various cancers	Approved 1/7/2005 FDA021660	American Pharmaceutical Partners
Triglide	Nanocrystalline fenofibrate	Oral tablets	Lipid disorders	Approved 5/7/2005 FDA021350	SkyePharma PLC
Megace ES	Nanocrystal/megestrol acetate	Oral suspension	Breast cancer	Approved 7/5/2005 FDA021778	Par Pharmaceutical Companies
Combidex	Iron oxide	IV	Tumor imaging	Phase III	Advanced Magnetics
Aurimune	Colloidal gold/TNF	IV	Solid tumors	Phase II	CytlImmune Sciences
NB-00X	Nanoemulsion droplets	Topical	Herpes labialis caused by herpes simplex I virus	Phase II	NanoBio
AuroShell	Gold-coated silica NPs	IV	Refractory head and neck cancer	Phase I	Nanospectra Biosciences
CALAA-01	Cyclodextran-containing siRNA delivery NPs	IV	Various cancers	Phase I	Calando Pharmaceuticals
Cyclosert	Cyclodextran NP	IV	Solid tumors	Phase I	Insert Therapeutics
INGN-401	Liposomal/FUS1	IV	Lung cancer	Phase I	Introgen
SGT-53	Liposome Tf antibody/p53 gene	IV	Solid tumors	Phase I	SynerGene Therapeutics

CHAPTER 2 MATERIALS, METHODS AND PROTOCOLS

2.1 Selection of Materials

The incorporation of imaging and therapeutic properties in a single nanoparticle system necessitates the use of multiple materials. Advances in nanoscale engineering have provided researchers with valuable tools to allow fabrication of hybrid materials (consist of organic, inorganic and metallic materials) yielding increasingly complex functionalities. In this chapter synthesis, characterization and functional evaluation of such nanomaterials is described. A brief description of the selected materials and rationale behind their selection is provided below.

Silica was chosen as a base material for the design of multicomponent particles. Silica is water dispersible, resistant to microbial attack and a nontoxic material. Silica particles are also resistant to swelling which allows their fabrication in a wide selection of solvents without altering their size, shape and porosity. Silica is an optically transparent material that means it enables incorporation of optically active components without any alteration in their properties such as emission and absorption of fluorophores. In addition, for targeted delivery of nanoparticles several biomolecules such as proteins, peptides, antibodies, oligonucleotides can be conjugated to the silica surface utilizing silane based chemistry. Silica nanoparticles of size varying from ~3 nm to several micrometers and different morphology such as sphere, nanotubes, and mesoporous structures can be synthesized using established synthesis protocols.

For optical imaging, fluorescent heptamethine cyanine organic dyes were selected for their incorporation in a silica matrix. These biocompatible dyes can be modified chemically to enhance their photostability and photoluminescence. Furthermore, unlike

commonly used NIR Indocyanine dye, these dye molecules can be covalently incorporated inside silica nanoparticle, which prevents dye leakage from the silica matrix. Moreover, these dyes possess inherent large Stokes shift (more than 100 nm) that makes them ideal candidate for circumventing energy transfer (fluorescence resonance energy transfer) upon encapsulation.

For photothermal therapy, metallic gold was employed for plasmonic heating and inorganic metallo-naphthalocyanine dyes were used for non-plasmonic heating. Gold nanoparticles possess size and shape dependent plasmonic properties that allow them to absorb in NIR region. Additionally, due to prevalent use of gold-based compounds in medicine (e.g., chrysotherapy) and the benign toxicity profile of gold nanoparticles renders them to be potentially more acceptable for clinical applications. The well established bio-conjugation strategies to the gold permit necessary surface modifications to bind specific ligands (peptides, antibodies, aptamers, polyethylene glycol, ligand) for targeted delivery to the diseased site and to enable rapid clearance of non-targeted particles. Metallo-naphthalocyanine dyes are available in wide range of absorbance wavelength including NIR region. The therapeutic potential of these dyes have already been established for photodynamic therapy. In addition *in vitro* biological assays show only benign toxicity associated with these dyes.

2.2 Materials Used

All reagents employed for the synthesis of multimodal nanoparticles were reagent-grade and used without further purification. Tetraethylorthosilicate (TEOS), 3-(aminopropyl)triethoxysilane (APTS), Triton X-100 (TX-100), n-hexanol, O-[2-(3-Mercaptopropionylamino)ethyl]-O'-methylpolyethylene glycol (PEG), β -alanine, 12-aminododecanoic acid and cyclohexane were purchased from Aldrich Chemical Co.

Inc.; Gold chloride, hydrazine hydrate, and dimethylformamide were obtained from Acros Organics; Ammonium hydroxide (NH₄OH, 28-30 wt %), triethyl amine and chloroform were obtained from the Fisher Scientific Co.; Fluorescein isothiocyanate (FITC), Isomer I, O-[2-(3-Mercaptopropionylamino)ethyl]-O'-methylpolyethylene glycol [SH-Peg (5000)], 2-[2-[2-Chloro-3-[(1,3-dihydro-3,3-dimethyl-1-propyl-2H-indol-2-ylidene)ethylidene]-1 cyclohexen-1-yl]ethenyl]-3,3-dimethyl-1-propylindolium iodide (IR 780), 2-[2-[2-Chloro-3-[[1,3-dihydro-1,1-dimethyl-3-(4-sulfobutyl)-2H-benzo[e]indol-2-ylidene]-ethylidene]-1 cyclohexen-1-yl]-ethenyl]-1,1-dimethyl-3-(4-sulfobutyl)-1H-benzo[e]indolium hydroxide inner salt, sodium salt (IR 820), 2,3-Naphthalocyaninato-bis(trihexylsiloxy)silane, Bis(trihexylsiloxy)silicon 2,3-naphthalocyanine (Si-dye), Zinc 2,11,20,29-tetra-tert-butyl-2,3-naphthalocyanine (Zn-dye), Manganese(III) phthalocyanine chloride, Iron(III) phthalocyanine chloride, cetyltrimethylammonium bromide were purchased from Sigma Aldrich Chemical Co.; EDC (1-Ethyl-3-[3-dimethylaminopropyl]carbodiimide Hydrochloride) and (NHS) N-hydroxysuccinimide were obtained from Thermo Fisher Scientific; Deionized (DI) water (NANOpure, Barnstead) was used for the preparation of all solutions.

2.3 Synthesis of Multifunctional Nanoparticles

2.3.1 Acid-Conjugated Dye Synthesis

300 mg of IR-780 dye was dissolved in 10 ml of anhydrous DMF in a 100 ml round bottom flask. To this solution, triethylamine (200 µl) and 12-aminodecanoic acid (263 mg) were added and the solution was heated for 3 h at 85 °C under nitrogen atmosphere. The green dye solution turned blue upon completion of meso-chlorine replacement reaction. This acid conjugated dye solution was stored at room temperature in a closed polypropylene container for further use. Simillar protocol was

used for the conjugation of dye with either β -aniline (108 mg) or 6-aminocaproic acid (160 mg) instead of 12-aminodecanoic acid.

2.3.2 Aminosilane Conjugated NIR-Dye

Carboxylic acid group of acid- conjugated dye, synthesized using above protocol was coupled with primary amine of an organosilane (APTS) using EDC/NHS coupling reaction. Briefly, 20 mg of NHS was dissolved in 1 ml of acid- conjugated dye solution in DMF. 60 mg of EDC solution in 1000 μ l (25 mM) MES buffer was added to the dye solution. After 15 min of stirring 50 μ l of APTS was added to this solution and the reactants were allowed to stir for 3-4 hours.

2.3.3 NIR Fluorescent Dye Doped Silica Nanoparticles

For the synthesis of NIR dye doped silica nanoparticles three different methods were used. NIR dye was covalently incorporated in the silica matrix. A brief description of principle underlying these methods and the protocols developed or modified are described below.

2.3.3.1 Microemulsion method

A common approach for synthesizing dye-doped silica nanoparticles is by using water-in-oil (w/o) microemulsions sometimes referred to as reverse microemulsions⁵⁴⁻⁵⁸. In reverse microemulsions, surfactant stabilized aqueous nanodroplets are formed in a bulk organic phase. Particle synthesis is nucleated and carried out within the constrained “water pools” (also referred to as reverse micelles), hence particles resulting from this method are typically of nanodimensions. The size of these water droplets or nanoreactors can be carefully changed by manipulating water to surfactant molar ratio, known as W_0 ⁵⁹⁻⁶². However, it must be noted that the overall reaction and particle formation process within the microemulsions is influenced by collision rates and

inter-droplet reactant exchange as well as reaction kinetics and resulting surface chemistries. Further, the selection of surfactant/co-surfactant, oil, water, temperature etc. can have profound effects on the size and shape of the synthesized particles. One of the key features of using reverse micelles approach is that it enables the production of nanoparticles with a narrow particle size distributions distribution. Because of this feature, microemulsions have been used exhaustively for the synthesis of highly regular nanoparticles, such as dye doped silica, gold and quantum dots. Another advantage of using the reverse micelles is the ability to fabricate particles that are readily water dispersible, which is an important requirement for the majority of biological applications. Reverse micelles also enable fabrication of core-multiple shell particles in a one pot reaction. The fundamentals and scope of microemulsion mediated nanoparticle synthesis have been covered exhaustively in the literature⁶³⁻⁶⁶. The applications of microemulsions for synthesis of fluorescent and gold speckled silica nanoparticles as contrast agents for bio imaging applications in the present investigation is discussed in the following sections.

The water-in-oil (w/o) microemulsion was prepared by mixing 1.77 g Tx-100, 7.7 ml cyclohexane, 1.6 ml n-hexanol and 480 μ l water. This solution was stirred on a magnetic stirrer for 10 minutes. To this solution upon dropwise addition of 480 μ l of nanopure water, optically transparent water in oil (w/o) microemulsion formed. Varying amounts (20-150 μ l) of NIR dye-APTS conjugate solution was added to the above microemulsion and stirred for 10 more minutes. Next, 50 μ l of TEOS was added to the microemulsion and allowed to equilibrate for 30 minutes. After 30 minutes of stirring, 100 μ l of NH_4OH was injected into the microemulsion to initiate TEOS hydrolysis and

polymerization. As mentioned earlier, the size of the silica nanoparticles, prepared in w/o microemulsions can be changed by varying the W_0 and /or reactant concentrations. In general, the decrease in W_0 in Tx-100/cyclohexane/water microemulsions has been shown to increase the size of the silica nanoparticles.

It should be noted that upon mixing if the microemulsion solution is not optically clear, modifications to the protocols are necessary to ensure the production of monodisperse particles. Because of variations in the chemical properties of conventional TX-100, which is a polydisperse nonionic surfactant, we have noticed that, on occasion, additional water may need to be added to the microemulsion to achieve clarity (e.g., 480 μ l instead of 340 μ l of water). Alternatively, the TX-100 surfactant concentration may be reduced to obtain clarity at the same water content. Titration experiments may be performed to determine where the water in oil suspension transits from a whitish emulsion to a clear microemulsion. It is advantageous to be at lower water loadings within the clear microemulsion regime. The amount of water that can be added to microemulsions is limited; otherwise once a certain threshold is reached microemulsions will revert back to thermodynamically unstable emulsions.

Nanoparticles were extracted from the microemulsion by addition of ~4-5 ml of 200 proof ethanol with continuous stirring. Stirring was stopped after approximately 5 minutes and the resulting mixture was allowed to stand for 10 minutes. Additions of ethanol lead to complete destabilization of the reverse micelles and resulted in the formation of two immiscible layers of ethanol and oil (cyclohexane). Nanoparticles accumulated in bottom ethanol layer and were separated by centrifugation. The top layer of surfactants, ethanol, and oil was carefully removed, and replenished with 200

proof ethanol. The solution was vortexed and sonicated to redisperse the particles followed by another round of centrifugation. For complete removal of the surfactant the particles were washed four times with ethanol and five times with water. After final water washing the nanoparticles were redispersed in double deionized water.

A quick check to ensure that the surfactants have been sufficiently removed is to assess suspension foamability in water. In the presence of small amounts of TX-100 relatively stable, surfactant induced foaming occurs with mechanical agitation. Additional washing steps are necessary if a noticeable and relatively stable foam layer appears after vigorously shaking the washed nanoparticle suspension in water. It should also be noted that depending on the conditions used during synthesis, surfactants may leach out of the silica particles over time. Hence foamability should be evaluated again after 24 h. If foaming is noticed, the samples should be re-washed and then rechecked for surfactant leaching. Typically, all of the washable surfactant is removed by the second washing procedure step.

2.3.3.2 Sol-Gel synthesis

Sol-gel based method for synthesizing monodisperse silica nanoparticles was first developed by Stöber⁶⁷. This method has been widely used for synthesizing spherical, monodisperse and electrostatically stabilized silica particles in the range from tens of nanometers to submicron regime. In this method hydrolysis and condensation reactions of alkoxy silane compounds (tetraethylorthosilicate (TEOS), tetramethylortosilicate (TMOS)) are performed in ethanol solution in the presence of water and ammonia which is used as a catalyst. In this study, a modified Stöber's method was used to covalently incorporate organic fluorophores to silica matrix by coupling them with reactive organosilicates.

Heptamethine cyanine dyes are hydrophobic in nature and hence their incorporation in hydrophilic silica matrix was achieved by modification of dye. For example, IR780 dye can be chemically modified with an amine containing silane agent (e.g. APTS, aminopropyltriethoxy silane) and then this conjugated dye is allowed to hydrolyze and condense to form FITC conjugated silica particles. Briefly, 11.4 ml ethanol (200 proof) and 570 μ l of ammonium hydroxide (28 wt% solution) were mixed by stirring. To this solution 570 μ l of TEOS and varying amount (20-200 μ l, 10 mg/ml in DMF) of silane conjugated dye was added. This solution was allowed to react for 5-6 h before washing the particles with ethanol (2 times) and water (3 times) followed by centrifugation and resuspension.

2.3.3.3 Mesoporous nanoparticle synthesis

Hybrid materials based on cooperation of organic-inorganic structures have long attracted interest of scientific community as these materials possess desirable properties of both inorganic and organic materials. Mesoporous materials are particularly attractive class of inorganic materials that can be employed as a mechanically robust scaffold for the synthesis of hybrid materials. Supramolecular self assembly of ionic surfactants forms lyotropic liquid-templates for the formation of mesostructured silica nanoparticles during the condensation of silica precursor. Synthesis in alkaline medium provides highly condensed, stable and ordered particles. Silica based mesoporous organic-inorganic hybrid nanoparticles with a variety of shapes and size ranging from 20 to 500 nm and pore size from 2 to 10 nm can be synthesized using methods developed by Lin et al.⁶⁸. These researchers produced particles with well defined cylindrical pores arranged in a hexagonal structure which give rise to high surface areas (900-1500 m^2/gm) and large pore volumes (0.5-1.5 cm^3/gm).

Recent advancements in modifying the internal as well as external surfaces of mesoporous silica nanoparticles have made these materials attractive for biological and biomedical applications.

In this work, mesoporous silica nanoparticles were synthesized by condensation of TEOS in presence of cetyltrimethylammonium bromide (C₁₆TAB) as structure directing template, under basic pH conditions at an elevated temperature. Briefly, 0.5 gm of C₁₆TAB and 1.75 ml of 2 M NaOH were added to 240 ml of nanopure water and the surfactant solution was heated to 80 °C. Once the equilibrium is reached, 2.5 ml of TEOS was added dropwise to this solution. After 2-3 minutes the transparent solution turned milky due to the nucleation of silica nanoparticles. At this time the desired amount of APTES- conjugated dye (100-2000 µl) was added. The particle suspension was allowed to stir for 3 h at constant temperature of 80 °C.

For the removal of surfactant, particles were dispersed in 2 wt% methanolic solution of CaCl₂ and the suspension was stirred for 4 h at 60 °C. For 1 g particles, 100 ml of CaCl₂-methanol solution was used. These particles were centrifuged and re-suspended in the CaCl₂-methanol solution with the aid of sonication. The centrifugation/resuspension step was repeated 3 times in order to completely remove the surfactant from the pores. Finally, these particles were suspended in nanopure water by centrifugation and resuspension using sonication.

2.3.4 Synthesis of Gold Speckled Silica Nanoparticles

Synthesis of gold-silica composite nanoparticles was carried out by a one pot method utilizing reverse micelles of a quaternary microemulsion system described above. The complete synthesis can be divided in two steps, first core silica

nanoparticles were synthesized and then gold specks were deposited on the surface of silica nanoparticles.

2.3.4.1 Synthesis of dye doped silica core

Microemulsion was prepared using Triton-X 100 (surfactant), n-hexanol (cosurfactant), cyclohexane (continuous oil phase) and water (dispersed phase) as described above. Nucleation of silica nanoparticles was initiated in the aqueous core of reverse micelles by the addition of 50 μl of tetraethyl orthosilicate and 100 μl of ammonia (catalyst). Varying amounts (10-30 μl) of APTS was added for functionalizing nanoparticle surface by free amine groups. Microemulsion was stirred for 24 hrs to allow the formation of silica nanoparticles. The synthesis of NaOH catalyzed silica nanoparticles was carried out in the same microemulsion system using NaOH (0.1 M, 100 μl) as a catalyst instead of ammonia.

2.3.4.2 Silica coating for prevention of quenching

In order to prevent the quenching of fluorescence by gold nanoparticles, a thin layer of silica was coated on NIR dye doped silica nanoparticles prior to the deposition of gold specks. Briefly, after the synthesis of dye doped core, 100 μl of TEOS and equal amount of ammonia was added in the microemulsion for the formation of thin shell of silica. The microemulsion system was continuously stirred for 24 h to allow for uniform silica coating.

2.3.4.3 Removal of ammonia from microemulsion

In order to study the role of ammonia in the formation of GSS nanoparticles, their synthesis was performed in absence of ammonia. Removal of ammonia from microemulsion was achieved by purging the microemulsion with N_2 gas for 30 min. Ammonia was removed from the microemulsion after the silica nanoparticle formation

and prior to the gold deposition. The removal of ammonia was verified by measuring the pH of the microemulsion using litmus paper.

2.3.4.4 Gold coating on dye doped silica core

After the silica nanoparticle formation, aqueous gold chloride solution (0.25-1 M, 125 μ l) was added slowly to the microemulsion. Addition was done in steps of 25 μ l at a time. After complete addition of gold chloride, microemulsion was allowed to stir for additional 3 h for the completion of deposition of gold-ammonia precipitate on silica nanoparticle surface. A dilute (2 wt%) solution of reducing agent, hydrazine hydrate, was added slowly in steps of 50 μ l to this microemulsion until all the gold was reduced. Upon addition of reducing agent microemulsion changed from yellow to greenish in color. The suspension was stirred for another 12 h for the complete reduction of gold-ammonia precipitate to metallic gold.

2.3.4.5 Separation of gold coated silica nanoparticles

Microemulsion was destabilized by the addition of approximately 10 ml of ethanol (200 proof). After few minutes GSS nanoparticles settled down at the bottom of glassware. These particles were washed 3 times with ethanol and 4 times with nanopure water by centrifuging and redispersing them. Surfactant free washed particles were finally dispersed in 10 ml of nanopure water.

2.3.5 Synthesis of Internally Gold Speckled Silica Nanoparticles

For the synthesis of these nanoparticles, small sub 4 nm gold nanoparticles were encapsulated inside the silica nanoparticle matrix. This synthesis was also performed in reverse micelles of an o/w microemulsion. In a typical microemulsion preparation 1.77 g of Triton-X 100 surfactant was mixed with 1.6 ml of n-hexanol and this mixture was added to 7.7 ml of cyclohexane. This solution was stirred on a magnetic stirrer for 10

minutes. To this solution upon dropwise addition of 400 μ l of nanopure water, transparent microemulsion formed.

2.3.5.1 Gold encapsulation in silica nanoparticles

Varying amounts (0.5M, 20-100 μ l) of gold chloride solution was added dropwise to the microemulsion. After complete addition of gold chloride, microemulsion was stirred for 1 h. To this microemulsion, upon addition of 100 μ l ammonia, gold-ammonia precipitate formed in the aqueous core. This microemulsion was stirred for additional 30 minutes to obtain homogeneous distribution of gold-ammonia precipitate. Each aqueous core contains several sub 4 nm size spherical particles made of gold-ammonia precipitate. In the next step these multiple nanoparticles were encapsulated/embedded inside a silica matrix. Nucleation of silica nanoparticles around the precipitate was initiated in the aqueous core of reverse micelles by the addition of 100 μ l of TEOS. After 1 h, 100 μ l of silane conjugated dye solution was added to the microemulsion. This microemulsion was stirred for 24 h for the complete formation of luminescent IGSS nanoparticles. Microemulsion was destabilized as described above and particles were washed and finally dispersed in 10 ml of nanopure water.

2.3.5.2 Reduction of gold-ammonia complex inside IGSS nanoparticles

Gold-ammonia complex encapsulated inside IGSS nanoparticles was reduced to metallic gold in a controlled manner. To the aqueous dispersion of 10 mg particles, 300 μ l of 2 M NaBH₄ was added. The color of the dispersion changed from pale yellow to brown-black over the period of five minutes. These particles were immediately washed three times with nanopure water to remove remaining reducing agent.

2.3.6 Synthesis of Multiple Dye Doped Silica Nanoparticles

For the synthesis of these nanoparticles, first, NIR dye doped mesoporous silica nanoparticles were synthesized as described above (section 2.3.3.3). After removing the surfactant from the pores, these particles were dispersed in chloroform to encapsulate the photothermal dyes inside the pores. In a typical synthesis, NIR-mesoporous silica nanoparticles (10 mg) were dispersed in 8 ml chloroform. 2 mg of Si-naphthalocyanine dye in chloroform (concentration 1 mg/ml) was added to the nanoparticle dispersion. The dispersion was stirred overnight to allow for the maximum loading of the dyes in the pores of nanoparticles. Particles were washed by centrifugation method and were redispersed in water for further experiments. The supernatant was used to estimate the amount of dye incorporated inside the pores of particles, by measuring its absorbance. Alternatively, these particles can be synthesized by adding the fluorescent and heating dye together during the nucleation and growth of the particles. However, addition of heating dye during the synthesis caused change in the shape of mesoporous nanoparticles. Hence, synthesis protocol needs to be modified in order to obtain spherical mesoporous nanoparticles from this method.

2.4 Particle Dispersion and Surface Conjugation

Further particle surface modification may be required to improve the dispersion of the particles in biological media as well as for attaching functional groups which would enable bioconjugation of targeting molecules such as antibodies, peptides and receptor specific ligands. For nanoparticles with external silica surface, silane chemistry was used to modify their surface by amine groups. In case of gold deposited on particle surface, gold-thiol chemistry was used to attach dispersing agents such as polyethylene glycol.

2.4.1 Amine Functionalization of Silica Surface

Particles were first dispersed in ethanol by centrifugation and redispersion method in order to completely remove the water from the particles suspension. These particles were then refluxed at 60 °C for 30 min before the addition of aminosilane (APTS). Amount of APTS sufficient to coat 5 monolayers on silica nanoparticles was added in the reaction mixture, which was refluxed for at least 12 h. After refluxing, particles were washed with water several times and dispersed in nanopure water. Zeta potential measurement of these particles verified the presence of amine functionality on their surface.

For the microemulsion mediated synthesis of nanoparticles, amines were directly co-condensed with TEOS to make the particles positively charged. It was observed that for 50 µl of TEOS, addition of up to 15 µl of APTS was required to obtain amine coated and well dispersed nanoparticles. Increasing the amount of APTS beyond 20 µl results in the loss of dispersibility of the particles.

After amine conjugation, suitable coupling reagents (e.g. EDC/NHS) were used to attach the bio-recognition molecules to nanoparticle surface⁶⁹. In some experiments nanoparticles were coated with biotinylated molecules that are well known to specifically bind with avidin conjugated bio-recognition molecules. For these reactions, excess of molecules (typically 3-5 times in number) that stoichiometrically needed were used. Complete surface coverage by coating molecules was assumed and the amount added to the reaction solution was calculated accordingly.

2.4.2 PEGylation of Gold Speckled Silica Nanoparticles

GSS nanoparticles were conjugated with thiol functionalized poly ethylene glycol (SH-PEG, MW=5000) acid following the procedure of Bergen et al⁷⁰. Briefly, ca.15 mg

of the GSS nanoparticles were dispersed in degassed nanopure water with sonication. The particles were then reacted with an excess of hetero bi- functional SH-PEG (MW 5000) at 25 °C for approximately 12 h to conjugate to speckled gold nanodeposits on GSS nanoparticles. The PEGylation step was carried out in the dark to prevent photodegradation of the dye. The particles were separated by centrifugation and washed thrice with PBS buffer, maintaining sterile and dark conditions.

2.5 Performance Evaluation of Multifunctional Nanoparticles

Several new protocols and methods were developed for the functional evaluation of multifunctional nanoparticles *in vitro* as well as *in vivo*. A mouse tumor model was used for *in vivo* experiments. Approval for animal studies was obtained from the University of Florida Institutional Animal Care and Use Committee (IACUC), and their strict animal care procedures followed for all experiments, as per NIH guidelines for the Care and Use of Laboratory Animals.

2.5.1 Imaging Experiments

For *in vitro* experiments, the A549 lung cancer cell line was used (from ATCC; cell line number CCL-185, <http://www.atcc.org/>). The growth media was prepared according to ATCC specifications (89% RPMI-1640 with L-glutamine (from Cellgro; Cat #: 25-053-CI), 10% Fetal Bovine Serum (four times filtered through 0.1 µm filter, from Hyclone; Cat. #: SH30070.03) and 1% antibiotic-antimycotic solution (from Cellgro; Cat. #: 30-004-CL)) The cells were cultured and harvested according to ATCC and the final cell suspension was prepared at $\sim 3 \times 10^6$ cells/ml and viability ratio above 95%. The cell viability and concentration determination was done using a ViCell Cell counter from Beckmann-Coulter (Fullerton, CA). The cell suspension was used to plate in various

culture vessels in concentration that reached 80% confluence after two days in complete media.

2.5.1.1 Confocal fluorescence imaging (*in vitro*)

A549 cells were plated in confocal dishes (from Matek Corporation; Cat. #: P35GC-1.5-14-C) following the culture guidelines established above. Cells at 80% confluency (after 24hrs of incubation) were dosed with GSS nanoparticles (20 $\mu\text{g/ml}$) and incubated for another 12 h. Four hours prior to dosing, the cells were aspirated and washed with Mg and Ca free HBSS, then incubated with 1mL of RPMI 1640 media with 1% FBS. The nanoparticles suspended in RPMI with 1% FBS were carefully administered to the A549 cells grown in the confocal dish to provide a final dose of GSS nanoparticles of 20 $\mu\text{g/ml}$ (6.23 mg/cm^2). After dosing the cells were returned to the incubator for 12 h. Internalization of the nanoparticles was determined by confocal microscopy. Prior to the confocal microscopy experiments, cells were rinsed with Ca and Mg free HBSS twice, to help remove free and cell surface bound nanoparticles, and finally 2 ml of growth media was added to the cells. The nucleus was stained with the HOECHST 33342 agent (1 μM) approximately 1 h prior to the fluorescence measurements. For the particle tracking in the cells, FITC doped nanoparticles were used. FITC has absorption maximum at wavelength 480 nm and fluorescence emission at 520 nm (pH range 5-9). An Olympus FluoView 1000 Laser Scanning Confocal Microscope System was used for all confocal imaging. Control cell cultures (without GSS nanoparticles) were used to appropriately set the confocal photomultiplier tube gains to ensure that background autofluorescence would not be registered in the images.

2.5.1.2 Bioluminescence and fluorescence imaging

Imaging was performed using the IVIS Spectrum *in vivo* Bioluminescence and Fluorescence Imaging System (Caliper Life Sciences). Image acquisition and analysis was performed with Living Image 3.2 or 4.0 software (Caliper Life Sciences). For imaging experiments, mice were anesthetized using 2–3% isoflurane. Bioluminescence was measured after 10–15 min following the intraperitoneal injection of luciferin (0.1 ml, 15mg/ml). For NIR nanoparticle imaging experiments, mice were injected intratumorally with nanoparticles (20 μ L, 1.5 mg/ml). Bioluminescence and fluorescence imaging was performed on the whole animal. In addition, imaging with shielding of the primary signal with mice in the ‘Gator’ Mouse Suit (GMS) and without the GMS was performed. Examples of shielding with conventional rigid constructs included Strathmore Artagain Paper, XMD-2 Manifold Divider (Caliper Life Sciences) and XAS-3 Animal Shield Kit (Caliper Life Sciences).

2.5.1.3 Photoacoustic imaging (*in vitro*)

A mechanical scanning photoacoustic system, with single transducer to collect the acoustic signals, was utilized. The light source was a tunable pulsed Ti:sapphire laser working at 700–950 nm with 10 ns pulse duration, 10 Hz repetition rate and 120 mJ maximum pulse energy. The diameter of the laser beam was expanded to 30 mm with a concave lens. An immersion acoustic transducer with 1 MHz nominal frequency was driven by a motorized rotator to receive acoustic signals from the samples over range of 360° (3° interval). A total of 120 measurements were performed for each scan.

The scanning plane was adjusted along the z-axis by mounting the rotator and the transducer on a platform driven by a linear stage. The phantom containing the samples and the acoustic transducer were immersed in the water tank, with the phantom at the

center of the tank where it was illuminated by the laser. Light-induced electronic signals from the transducer were collected with a receiver and a high-speed PCI data acquisition board. PAT images were reconstructed based on the finite element solution to the photoacoustic wave equation in the frequency domain, which can provide stable inverse solutions.

Phantoms for imaging were constructed using intralipid, India ink, distilled water, and 2% agar powder. The diameter of the phantom was 25 mm. The optical absorption and reduced scattering coefficients of the phantom were 0.007 and 0.5 mm⁻¹, respectively.

2.5.1.4 Photoacoustic imaging (*in vivo*)

In vivo experiments were carried out with mouse tumor model. Six to eight week old BALB/c nude mice (CAnN.Cg-Foxn1nu/Crl) were purchased from Charles River and acclimated for 7 to 10 days. Supplemental estrogen (2µg of 17β-estradiol valerate/week) was placed subcutaneously at least 1 week prior to tumor implantation. Mice were subcutaneously inoculated with 2 x 10⁷ BT474 cells on the abdominal wall. Experiments were conducted 7–10 days following implantation, after the tumors had grown to approximately 10 mm in size.

Mice were anesthetized using intraperitoneal injection of pentobarbital. A volume of 30µl of nanoparticle suspension (10 mg/ml GSS) or control saline solution was injected into the mouse tumor. The anesthetized mouse was placed in the water tank on an inclined plane with its head above the water surface. The PAT instrumentation for *in vivo* experiments was similar to that described for *in vitro* experiments, except that acoustic signals were collected over 300° range, giving a total of 100 measurements for

each trial. PAT images of mouse tumor were obtained before and after injecting nanoparticles.

2.5.2 Photothermal Efficiency Measurements

Photothermal efficiency of different nanoparticles was compared by measuring the temperature rise of their suspension in water upon laser irradiation. A fiber-coupled continuous wave laser source (B&W TEK Inc, BWF2-785-5-400-0.22-SMA) with a center wavelength of 785 nm was used. The output power of laser was kept constant at 500 mW (350 mA laser diode current) in all the experiments. An optical fiber was used to transfer the NIR laser radiation from laser source to the sample cell (Fisher Brand, 1.5 ml methacrylate cuvette, cat no. 14-955-128). The end of the optical fiber was positioned 2 cm above the liquid level in the sample cell. The sample cell was filled with 1 ml of nanoparticles suspension at the required concentration in nanopure water. A thermocouple was placed away from the laser path in the sample cell for the temperature measurements.

2.5.2.1 Nanoparticles uptake quantification using flow cytometry

The flow cytometry experiments were done following the same nanoparticle dosing protocols as above. Briefly, cells (3.0×10^6 /well) were seeded into 6 well tissue culture plates and allowed to adhere for 24 hours. Cells were exposed to dye doped PEGylated nanoparticles (20 μ l or 40 μ l) for 24 h. Cells were harvested by 0.25% trypsin with EDTA, washed with PBS, centrifuged (at 500 g for 5 min) and resuspended in PBS. Uptake of dye doped PEGylated nanoparticles was analyzed using a BD LSR flow cytometer (Becton Dickinson Biosciences, CA) with computer-assisted data analysis (BD FACSDiva). At least 10,000 cells were analyzed in each sample and all experiments were performed at least in duplicate.

2.5.2.2 Photothermal ablation (*in vitro*)

A549 cells were grown on MgF₂ plate (5 mm x 5mm) in a 6 well plate and dosed with GSS nanoparticles. The MgF₂ chips were then moved on a Delta T Culture Dish (from Biotechs; Cat #: 04200415C), and 2 mL of RPMI 1640 were added. The dish was placed onto a heating stage (Delta T4 Culture Dish Controller, Biotechs, Butler, PA) and temperature was maintained at 37 °C. The NIR laser (diode laser 785 nm, 58 mW through the 63x lens) attached to the Renishaw InVia Confocal micro-Raman Instrument (Hofman Estates, IL) was scanned over the labeled cells in a nearly straight path. Next, Trypan Blue solution in phosphate buffer was added to the cells, incubated for 15 minutes, and imaged using Olympus BX60 with SPOT Insight Digital Camera (Central Valley, PA, USA).

2.5.2.3 Photothermal ablation (*in vivo*)

Six to eight week old BALB/c nude mice (CAAnN.Cg-Foxn1nu/Crl) were purchased from Charles River and acclimated for 7 to 10 days. Supplemental estrogen (2µg of 17β-estradiol valerate/week) was placed subcutaneously at least 1 week prior to tumor implantation. Mice were subcutaneously inoculated with 2×10^7 BT474 cells on the abdominal wall. Experiments were conducted 7–10 days following implantation, after the tumors had reached approximately 10 mm in size. 300 µg GSS nanoparticle suspension or control saline solution was injected into an anesthetized mouse tumor directly. The anesthetized mouse was placed on an inclined plane with the tumor exposed. Photothermal ablation experiments were carried out with 785 nm (B&W TEK Inc, BWF2-785-5-400-0.22-SMA), continuous wave laser at 500 mW output power (power density 325 mW/cm²) for 10 minutes. The distance between the optical fiber and the tumor was maintained at 15 mm for all *in vivo* experiments. The mice were

sacrificed using approved methods 24 hours after exposure to near-infrared laser irradiation. Tumors were harvested and fixed in formaldehyde solution. Tissue sections were stained with Hematoxylin and Eosin and subsequently analyzed. Percentage of necrosis was analyzed in tumor specimens in treated and control tumors by pathologists blinded to the treatment. Tissue handling and preparation for fluorescence microscopy involved fixing the tumor tissue in 4% paraformaldehyde by reperfusion fixation at 4°C, and subsequent immersion for 6 hours at room temperature, followed by washing in phosphate-buffer saline (PBS) for 48 hours at 4°C. These were subsequently embedded in OCT compound (Sakura Finetechnical, Tokyo, Japan) and stored at -80°C until further analysis. Sections were rehydrated in PBS and stained by 10 µM HOECHST 33342 (AnaSpec, CA) prior to observing the tissue under fluorescence microscope (Olympus IX71).

2.5.2.4 Photothermal ablation using bioluminescence model

The 4T1 murine mammary tumor cell line expressing the firefly luciferase enzyme was orthotopically implanted (10^6 cells) into female BALB/c mice. On post-implantation day 8, mice were imaged via fluorescence (710 nm excitation/820 nm emission) and bioluminescence (image obtained 10 minutes post 100 µl luciferin (15 mg/ml) intraperitoneal injection) with the IVIS Spectrum (Caliper Life Sciences). Mice were randomly distributed to 3 groups including NPs/+ablation, NPs/-ablation, and control/+ablation. Mice underwent NPs intratumoral injection (15 mg/ml, 20 µl) or 0.9% NaCl (20 µl). Fluorescent imaging was conducted on all mice after intratumoral injection. Mice then underwent photothermal ablative therapy (continuous wave laser, 785 nm, 500 mW, 5 minute duration, 1.5 cm source-tumor distance) followed by fluorescence imaging. All mice underwent bioluminescent imaging. In addition, a luciferin-luciferase

enzyme reaction kinetic study was performed. Luciferin intraperitoneal injection versus intratumoral injection (10 μ l, 15 mg/ml) was performed to investigate the mechanistic response to photothermal ablation. On post-ablation day 1, mice underwent fluorescent/bioluminescent imaging and subsequently were sacrificed. A subset of mice was studied for 8 days after NPs injection to determine photostability of NPs after photothermal ablation. Tumors were harvested and sectioned in half for freshly frozen ex-vivo confocal microscopy imaging (Leica TCS SP5, Leica Microsystems) or preserved in 10% neutral buffered formalin for histological analysis. Confocal microscopic specimens were mounted with DAPI or HCS CellMask Orange (Invitrogen). Histological tumor analysis was performed in a blinded fashion and quantified as percent necrosis by a board certified pathologist. Region of interest (ROI) quantification of fluorescent and bioluminescent signals was performed at all imaging points with Living Image 3.2 software (Caliper Life Sciences).

CHAPTER 3

NIR DYE DOPED LUMINESCENT SILICA NANOPARTICLES

In chapter 1, the advantages associated with early stage detection of disease such as cancer were discussed. It was concluded that NIR fluorescence optical imaging, due to its extremely high sensitivity, could play an important role in the development of next generation of early stage cancer diagnosis and therapy methods^{25,40,71}. Fluorescence imaging often requires use of contrast agents such as organic and inorganic fluorophores that upon photoexcitation emit photons (imaging signal) at longer wavelengths. In this chapter current status of NIR imaging probes and their limitations are discussed. Conventionally used NIR optical fluorescent probes either have inferior photophysical and photochemical properties (organic dyes) or exhibit heavy metal toxicity (inorganic QDs)⁵⁰. In order to overcome these limitations a new class of NIR dyes, heptamethine cyanine dyes, was chemically modified for their incorporation into a silica nanoparticle matrix. A significant decrease in photoluminescence due to aggregation of dye molecules was observed, when these dye molecules were dissolved in aqueous solvents for their incorporation into nanoparticles. It became apparent that dye aggregation and self-assembly in solvents could deleteriously impact fluorescence performance. In order to maximize the photoluminescent properties of these materials, several strategies were developed for minimizing the aggregation of these dye molecules during their incorporation in silica nanoparticles. New approaches were developed to integrate dye molecules in three different classes of silica nanoparticles, commonly used for biological applications: Stöber silica (sol-gel method), mesoporous silica (surfactant template method), and microemulsion silica (reverse micelles method). Incorporation mechanisms of heptamethine cyanine dyes in all three methods were

investigated and the resulting photoluminescence was compared. In this study, it was established that both quantum yield and molar absorptivity of the dye doped nanoparticles must be considered for maximizing their photoluminescence properties.

3.1 Research Approach

Past attempts for developing NIR fluorescent nanoparticles have primarily focused on encapsulation of an organic dye- Indocyanine Green (ICG) into NPs. Like other organic dyes in its class (cyanine dyes), ICG has low quantum yield, is prone to photobleaching and has low stability under harsh chemical environments. The inferior photophysical/photochemical properties and lack of conjugation ability of ICG dye has severely impacted their incorporation in a nanoparticle matrix. In order to overcome some of the limitations associated with ICG, a subclass of cyanine dyes has recently been developed by modifying the original cyanine dyes. Heptamethine cyanine dyes have been synthesized by introducing the chlorocyclohexenyl ring in the methine chain of cyanine dyes. Addition of this ring provides structural rigidity, enhanced photostability and high fluorescence quantum yield and most importantly an opportunity for chemical modification by replacing the chlorine group⁷²⁻⁷⁴. The meso-chlorine atom of these next generation of ICG dyes have been replaced by enol, thioenol or amino linkers⁷⁵. In comparison to enol or thioenol ether bonds, robust C-N bond on the methine chain gives these dyes desirable properties like chemical stability, photostability, stronger fluorescence compared to ICG, and a conjugation site that could potentially be used for their incorporation inside a matrix by covalent incorporation.

In this study, we have modified heptamethine cyanine dyes at the meso-chlorine position with carboxy terminal amino linkers of varying chain lengths. Conjugation of these dyes with acid group resulted in large Stokes shift, a much sought after property

for enhancing the signal to noise ratio in imaging. Although these dyes have several fold increase in quantum yield (QY) compared to ICG in aqueous solvents, the overall value of QY is low (2-3% compared to 100% for an ideal fluorophore). Cyanine dyes are well known for low quantum yield in aqueous solvents due to the aggregation induced by their highly conjugated chemical structure. Absence of polar chemical groups on heptamethine cyanine dyes further promotes their aggregation. Most commonly used dyes in this class are IR780, IR820 (also known as next generation ICG) and their derivatives. In order to fully realize the potential of these dyes, their photophysical properties were examined in aggregation free medium. Different solvents of varying polarity were selected and it was observed that unlike ICG, QY of heptamethine cyanine dyes is significantly higher (up to 35 times) in non aqueous solvents (figure 3-1). The high QY in nonaqueous solvents is due to (1) high solubility of dyes in non aqueous solutions, and (2) structural rigidity of the dyes due to the cyclic ring at the center position.

Although these dyes possess superior photoluminescence, their use in biological applications remain limited primarily due to their hydrophobic nature. Incorporation of these dyes into a solid matrix could potentially render them suitable for use in biological medium. However, the covalent encapsulation of NIR chromophores inside a nanoparticle matrix is a long standing and challenging task. To the best of our knowledge, none of these dyes have been covalently incorporated in a rigid matrix such as that of silica nanoparticles. Hence, one of the goals of this investigation was to incorporate these structurally rigid dye molecules in a matrix of biocompatible

nanoparticles such that, during and after their incorporation, the dye molecules remain in dispersed state and are not prone to leaching.

3.2 Results and Discussion

The photophysical behavior of an individual dye molecule can be enhanced by modifying its physicochemical environment^{76,77}. For example, quantum yield of a fluorophore can be increased by encapsulating it inside a rigid matrix. Previously, attempts have been made to increase the overall brightness of dye doped nanoparticles by enhancing the quantum yield (QY) of encapsulated dye molecules^{26,78}. While high QY could be important for applications such as single particle tracking, fluorescence imaging requires high photoluminescence from the particles and not only high quantum yield. Unlike organic dyes and inorganic quantum dots the brightness of inorganic-organic hybrid dye doped silica nanoparticles can be enhanced by increasing their molar absorptivity i.e. by increasing the number of dye molecules incorporated inside the particles. In an ideal case, when there is no interaction amongst the dye molecules inside silica matrix, the brightness of an individual particle is directly proportional to its molar absorptivity and quantum yield. However, the quantum yield of encapsulated dye molecules decreases with the increase in their number. The decrease in QY is attributed to energy transfer between closely spaced dye molecules and aggregation due to their highly conjugated chemical structure^{56,79,80}. As a result, at higher concentration of encapsulated dye molecules, the overall brightness of the particles becomes much lower than the expected value.

Clearly, the dispersion of dye molecules, inside the NP matrix, plays major role towards determining their final photoluminescence properties. However, there have been only limited studies for controlling the spatial dispersion of dye molecules inside a

solid matrix. In this work we have shown that dispersion of dye molecules within silica nanoparticles can increase their photoluminescence properties by several orders of magnitude. We have developed various strategies to disperse dye molecules inside silica matrix in such a way that upon encapsulation, decrease in the quantum yield of the dye is minimized. Most commonly used methods for the synthesis of silica nanoparticles were employed to enable incorporation of dye molecules. The different mechanisms of particle formation offered by these methods present an opportunity to control the dye incorporation in different ways. Although the proposed strategies were employed to encapsulate heptamethine cyanine dyes in silica matrix, these methodologies can be extended to other dyes and matrix systems.

3.2.1 Particle Formation by Stöber Method

In the Stöber method, ammonia-catalyzed hydrolysis and condensation of tetraethylorthosilicate (TEOS) in a mixture of ethanol and water is employed to synthesize monodispersed silica nanoparticles⁶⁷. Addition of a heptamethine cyanine dye conjugated with a silane (3-aminopropyltriethoxysilane, APTS) resulted in co-incorporation of dye molecules in the silica matrix. Different amount of dye were encapsulated inside the particles by varying the concentration and rate of addition of dye in the reaction mixture. However, the fast kinetics of hydrolysis and condensation reactions permitted only partial control on the incorporation of dye molecules. Moreover, the limited solubility of heptamethine cyanine dyes (employed in this study) in ethanol limited their use at high concentrations. Higher concentration of dye resulted in the formation of non fluorescent aggregates in the solution. Encapsulation of these aggregates inside silica matrix resulted in the inferior photoluminescence of dye doped particles. These problems were overcome by controlling the hydrolysis reaction of

TEOS. In the presence of dimethylformamide (DMF) hydrolysis of TEOS is slowed due to the hydrogen bonding of DMF with water molecules⁸¹. Hence limited amount of water is available for the hydrolysis of TEOS. It is hypothesized that addition of heptamethine cyanine dyes in the reaction mixture results in increased availability of water for hydrolysis of TEOS due to preferred solubilization of dye in DMF (heptamethine dyes have high solubility in DMF compared to their solubility in ethanol). This hypothesis is in accordance with the experimental results that indicated: (1) At the same water concentration yield of the particles can be increased by the addition of acid in the reaction mixture. TEOS molecules are known to undergo complete hydrolysis in the acidic environment. (2) Addition of water in the reaction mixture causes sudden increase in particle yield. The availability of water results in the increased hydrolysis of TEOS and therefore particle yield increases. (3) Addition of APTS in the reaction mixture results in the increase in particle yield. Unlike TEOS, APTS has considerably high solubility in water and under suitable conditions such as those used in this experiment could initiate the nucleation for particle formation. It is clear from above three experimental results that hydrolysis of TEOS in presence of DMF can be controlled by adding one of the following in the reaction mixture: acid, water or APTS. Addition of acid could result in the degradation of organic dye and it was observed that addition of water in the reaction mixture increases the polydispersity of the synthesized particles. Hence, incorporation of dye in silica matrix was controlled by varying the amount of APTS conjugated dye and DMF in the reaction mixture. Figure 3-2(a) shows the representative TEM image of silica particles synthesized by Stöber method and their corresponding absorbance and fluorescence characterization.

3.2.2 Particle Formation by Surfactant Template Method

In the Stöber method homogeneous incorporation of dye is limited by the solubility of the dye in the reaction mixture (water-ethanol). Solubility of a hydrophobic dye in an aqueous environment can be enhanced with the aid of surfactants. For example, heptamethine cyanine dyes can be solubilized in the core of cetyltrimethylammonium bromide (C₁₆TAB) micelles at relatively high concentrations. These micelles not only protect the dye molecules from the bulk chemical environment but also help the dye molecules remaining dispersed during their covalent incorporation in the silica matrix. Incorporation of dye in the surfactant micelles was confirmed by the observed blue shift in the absorbance (640 to 500 nm) and fluorescence (760 to 540 nm) of these dyes. Supramolecular self assembly of these mixed micelles forms lyotropic liquid-crystalline phases that serve as a template for the formation of dye-doped mesostructured silica nanoparticles during the condensation of silica precursor. Because of the well-dispersed (or evenly distributed) dye molecules in the silica matrix, the resulting nanoparticles possess high photoluminescence and quantum yield. Details of the protocol developed for the synthesis of these nanoparticles are provided in chapter 2.

In this approach chain length of the conjugated acid group plays an important role. It was experimentally observed that when a small chain length acid (β -alanine) was conjugated to NIR dye, the resulting incorporation of dye in the mesoporous silica was minimal (optical density= 0.005 per mg of particles). Upon increasing the aminolinker chain length to 6 carbon (6-aminocaproic acid) results in the efficient incorporation of dye (optical density= 0.2 per mg of particles). Using 12 carbon chain (12-aminododecanoic acid) did not yield any higher incorporation of the dye molecules. However, this behavior changes with the type of the dye employed as the conformation

of dye molecules inside the micelles depends on their structure and polarity. For example, fluorescein isothiocyanate and rhodamine isothiocyanate dyes can be incorporated in the framework of mesoporous silica without adding any linker molecules. It is hypothesized that due to the highly hydrophobic nature of heptamethine cyanine dyes, they solubilize towards the center of the hydrophobic core of C₁₆TAB micelles. Hence a longer chain linker is required to enable their incorporation in silica framework that is constructed on the micellar template. FITC and rhodamine isothiocyanate dyes have relatively high solubility in water under basic pH condition, hence, their incorporation into silica network can be achieved directly from the water phase. For further experiments, 12 carbon chain linked dye molecules were incorporated in the framework of mesoporous silica. The size of nanoparticles as measured by SEM and TEM images was 105±18 nm. A normalized absorbance and emission spectra of mesoporous nanoparticles is presented in figure 3-2(b). The photoluminescence of these particles was maximized by optimizing the amount of dye present inside the silica matrix.

3.2.3 Particle Formation by Reverse Micelles Method

A modified reverse micelles method was used to harness advantages of both Stöber (slow kinetics) as well as surfactant template (dye dispersion) method. This method employs nanosize water droplets, stabilized by surfactants in the oil medium, for the nucleation and growth of silica nanoparticles. In this method, oil soluble TEOS molecules hydrolyze at oil-water interface prior to their condensation in the water droplets. The limited availability of water is responsible for the slow kinetics of particle formation in the reverse micelles. Further, the overall reaction and particle formation process is also influenced by collision rates and inter-droplet reactant exchange. In a

reverse micelles system, typical time for the complete synthesis of silica nanoparticles is ~24 h as compared to 2-3 h in modified Stöber synthesis described above.

The dispersion of silane conjugated dye molecules at the surfactant stabilized oil-water interface was controlled by tailoring the hydrophobicity of dye molecules. Based on the hydrophobicity of the dye molecule, their transport from oil phase to the oil-water interface can be controlled. When a heptamethine cyanine dye with polar groups (IR783) was used, the resulting silica nanoparticles had much lower photoluminescence as was the case also in the Stöber process. The decrease in fluorescence is hypothesized due to the formation and encapsulation of dye aggregates. A hydrophilic dye immediately goes into the water core upon its introduction in the microemulsion system, resulting in the encapsulation of dye aggregates when silica nanoparticles are formed in the water core. Similar behavior was observed for other dyes such as FITC and Rhodamine. For these dyes upon encapsulation their QY decreased from ~95% to ~2%. In order to slow down the transport of silane conjugated dye to the oil-water interface, the chain length of amino linkers was varied. Upon increasing the chain length from 3 to 12 carbon atoms, the brightness of the particles increased by ~8 times. Photoluminescence of these nanoparticles was further optimized by varying the total amount as well as dispersion of dye encapsulated inside the silica matrix.

TEM images and corresponding photophysical properties (absorbance and fluorescence) of particles in all three cases is presented in figure 3-2(a-c). For all three particles, dye molecules retain their large Stokes shift property even after their encapsulation inside silica matrix. Quantum yield of dye molecules encapsulated inside silica nanoparticles was measured for all nanoparticles using integrating sphere. Figure

3-3(a-c) represents the quantum yield as a function of increased concentration of encapsulated dye per mg of particles. The decrease in the quantum yield is attributed to the aggregation of dye molecules. Further, it is shown that for all three processes, quantum yield of the particles decreases logarithmically with increase in the amount of dye incorporated in the particles. The equations for the logarithmic decay in quantum yield and linear increase in number of dye molecules were solved graphically to obtain photoluminescence of NIR particles. The calculated photoluminescence of particles accurately predicts the existence of experimentally observed maxima for all three types of particles. It is evident from this analysis that quantum yield alone does not determine the brightness of dye doped nanoparticles; another important parameter, their molar absorptivity, must be considered. Particles are brightest when product of these two parameters (quantum yield and molar absorptivity) is highest. The position of maxima indicates the concentration until which dye molecules can be incorporated in silica matrix with minimal aggregation. After that the observed decrease in photoluminescence is due to increased aggregation of dye molecules inside silica matrix. The absolute photoluminescence of all three nanoparticles as a function of increased amount of encapsulated dye is compared in figure 3-4. It is clear from the plot that particles synthesized using microemulsion method has much higher photoluminescence compared to other two particles. The enhanced photoluminescence is attributed to (1) aggregation free dispersion of dye molecules in oil phase, (2) slow transport of TEOS and dye molecules from oil phase to the oil-water interface, and (3) dispersion of dye molecules in surfactant core of reverse micelles during their incorporation into silica matrix. For further biological studies, NIR dye doped silica

nanoparticles synthesized by microemulsion method were used due to their highest photoluminescence.

3.2.4 Stability and Detection Limit of the Particles in Biological System

Particles with the highest photoluminescence were injected in a nude mouse intratumorally and intradermally and their fluorescence was monitored over a period of 2 weeks. Figure 3-5(a-b) shows that for the intradermal injection there was negligible change in the fluorescence. For particles injected intratumorally, about 20% loss in their fluorescence intensity occurred. This loss in fluorescence is believed to be due to particle excavation from the tumor site. Indeed, post mortem analysis of the mice indicated the presence of NIR particles at distant metastatic sites. That said, a partial loss of signal could also occur due to chemical degradation within the dynamic chemical environment inside the tumor. However, even after losing 20% of the fluorescence intensity, fluorescence signal from the particles was about 10 times higher than the background signal.

Photoluminescence of the NIR particles was compared with that of Invitrogen QDs- a commercially available benchmark. For the same photoluminescence about 50 times less NIR particles are required compared to QDs (figure 3-6). Although NIR particles have lower quantum yield compared to QDs, they have higher photoluminescence due to their extremely high molar absorptivity (10^6 vs. 10^8). Figure 3-7 compares the *in vivo* detection limit of ultrabright NIR particles with the Invitrogen quantum dots. NIR particles and quantum dots were injected intradermally in a mouse. It was demonstrated that subfemtomolar concentration of particles can be detected that is one order of magnitude lower than the minimum concentration required for QDs detection.

3.2.5 Tumor Targeting Using NIR Nanoparticles

After establishing the superior photophysical and photochemical properties of NIR dye doped silica nanoparticles synthesized in this study, these particles were used for the detection of tumor in mice. Active tumor targeting of nanoparticles was achieved by functionalizing NP surface with a protein that targets tumor endothelial marker 8 (TEM8: a protein known to express within tumor endothelium). For this purpose, surface of nanoparticles was modified with aminosilanes using the procedure described in chapter 2. The amine groups were used to attach heterobifunctional PEG with amine reactive functional group on one side and biotin on the other end. In the next step, avidin functionalized TEM8 receptor was attached to the particles using biotin-avidin interaction. The TEM8 receptor functionalized particles were delivered systemically through the tail vein in mice and monitored using fluorescence imaging at different time intervals for up to 48 h. Accumulation of particles in the tumor was observed after 24 h (figure 3-8). Semi-quantitative fluorescence based analysis showed ~8% particle accumulation in tumor. Majority of the particles went to liver through RES clearance. Uptake of nanoparticles by RES system is well known and one of the main cause that plagues the targeting efficiency of nanoparticles in any biological system. The seemingly low targeting efficiency achieved in this work is comparable with the targeting efficiencies reported in literature in various biological studies.

3.3 Summary

In summary, ultra bright NIR fluorescent nanoparticles were developed by the incorporation of organic fluorophores in an inorganic matrix. Photophysical properties of these organic-inorganic hybrid nanocomposites were enhanced through controlled dispersion of dye molecules inside silica nanoparticle matrix. Due to the incorporation of

large Stoke shift dyes in nanoparticle matrix, the decrease in quantum yield as a result of energy transfer amongst the dye molecules was eliminated. In absence of fluorescence resonance energy transfer, the observed decrease in quantum yield was attributed to the presence of aggregates of dye molecules when incorporated at high concentrations. The most distinct feature of these nanoparticles is that they possess both optical tunability as well as size tunability. Surface of these nanoparticles was modified using silane chemistry and coupling reagents to target tumor through biorecognition event. Fluorescence property of these particles was utilized to demonstrate their active targeting potential as the particles locate tumor within 24 h, when introduced in the blood circulation.

The next step, as discussed in chapter 1, was to employ these specifically targeted nanoparticles for the selective destruction of targeted cells using localized therapy such as photothermal ablation. The exposure of photothermal materials to light causes conversion of absorbed photon into phonons, leading to high enough rise in local temperature that is sufficient to kill tumor cells. The next chapter describes the development of a novel approach for the incorporation of plasmonic photothermal materials in silica nanoparticles.

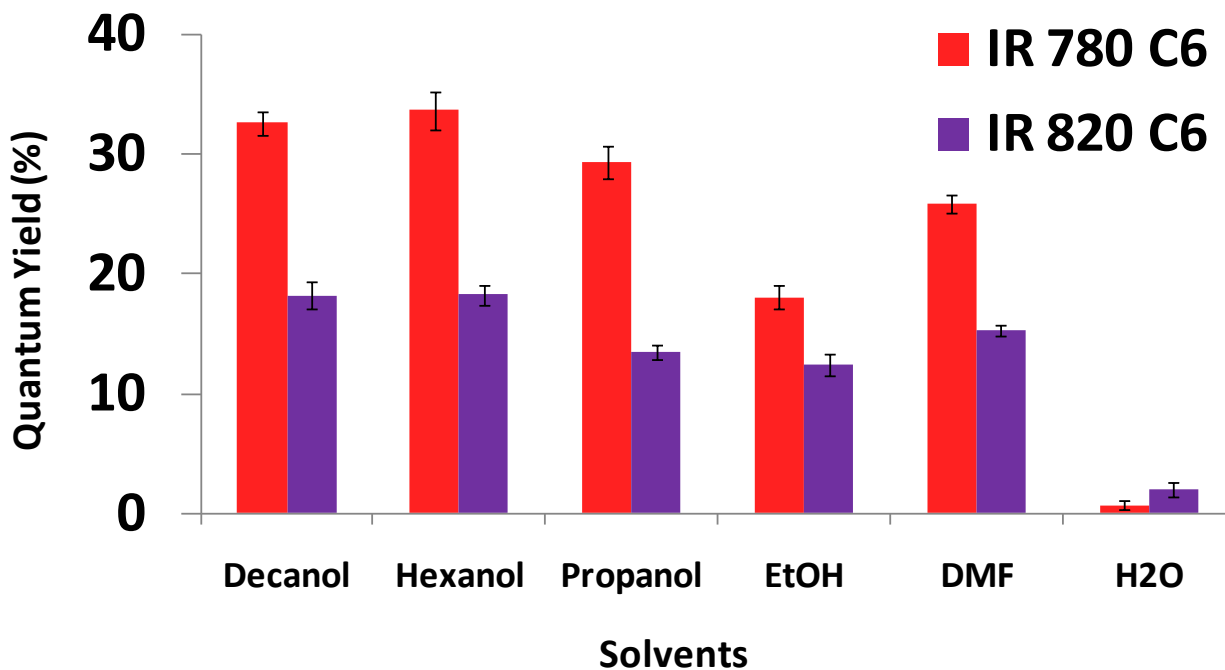


Figure 3-1. Quantum yield of IR 780 and IR 820 dyes, after conjugation with aminocaproic acid, measured in different solvents

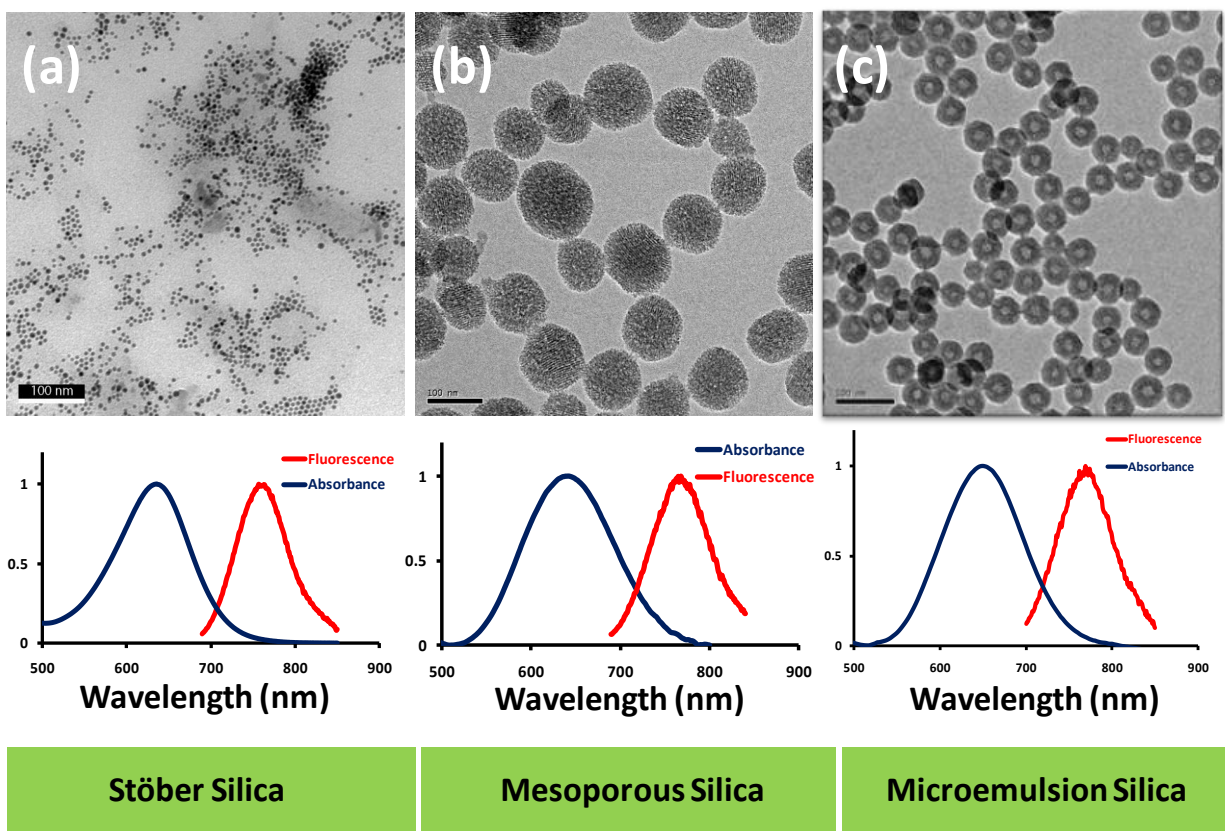


Figure 3-2. TEM images and corresponding photophysical characterization of (a) Stöber silica nanoparticles, (b) mesoporous silica nanoparticles, and (c) microemulsion silica nanoparticles.

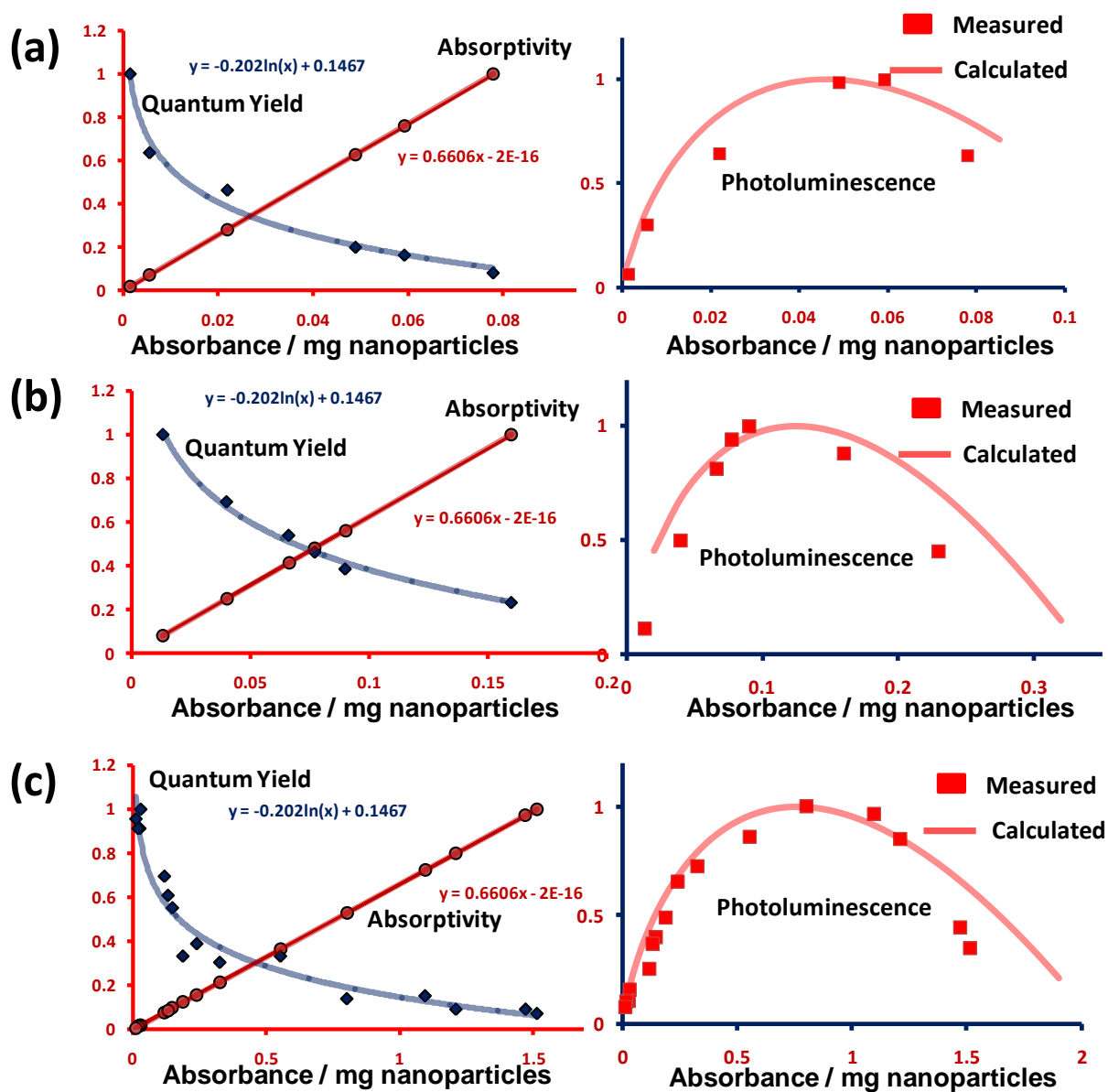


Figure 3-3. Left column: Normalized quantum yield and absorbptivity, right column : corresponding calculated and measured photoluminescence for (a) Stöber silica nanoparticles (b) mesoporous silica nanoparticles and (c) microemulsion silica nanoparticles.

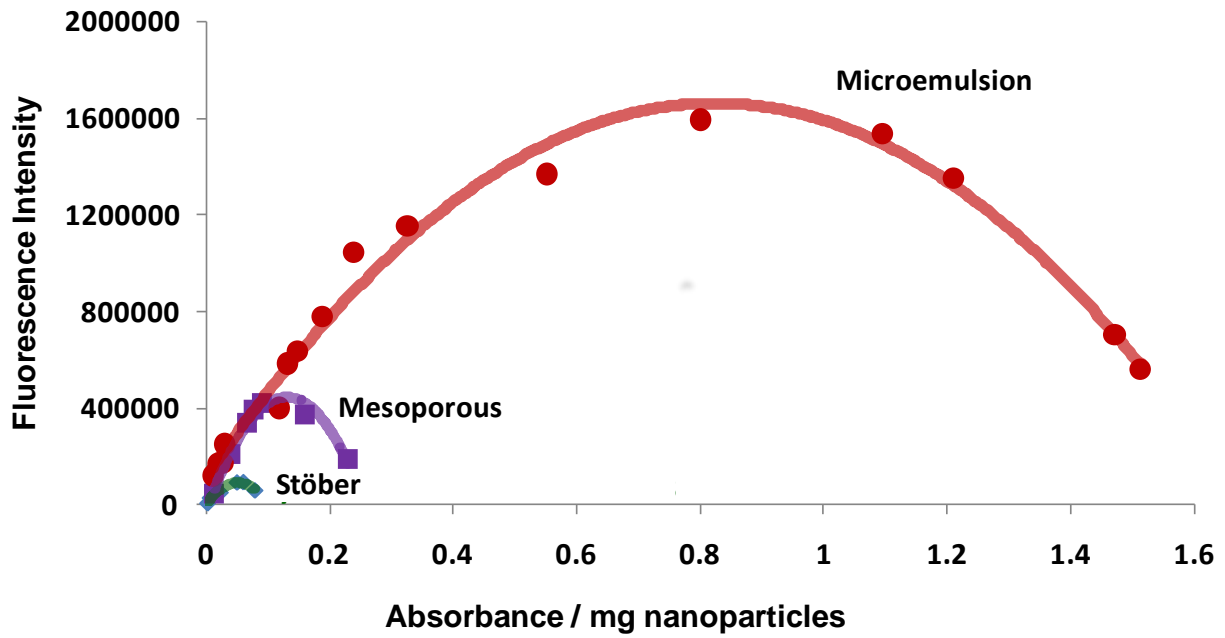


Figure 3-4. Absolute value of photoluminescence of Stöber, mesoporous and microemulsion silica nanoparticles, as a function of their optical density per mg of nanoparticles.

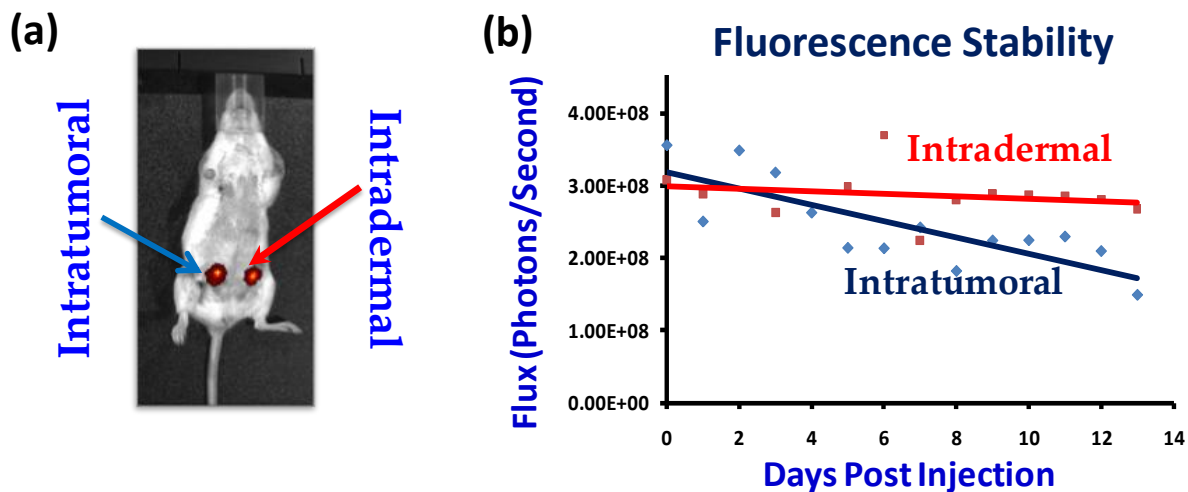


Figure 3-5. (a) Fluorescence image of mice injected with 30 μ l (5 mg/ml) nanoparticles (left side: intratumoral injection, right side: intradermal injection) (b) *in vivo* monitoring of fluorescence signal for 14 days.

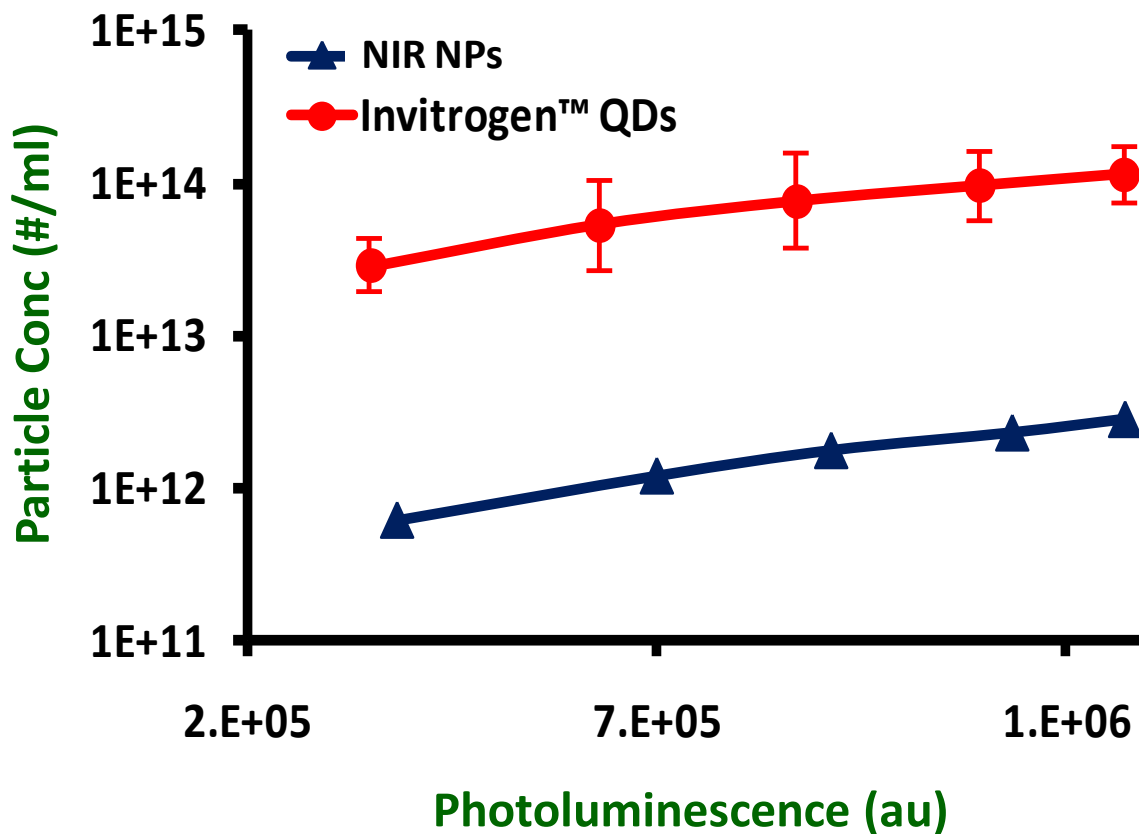


Figure 3-6. Comparison of photoluminescence of NIR dye doped silica nanoparticles and invitrogen QDs (for QDs error bars are too small to be visible).

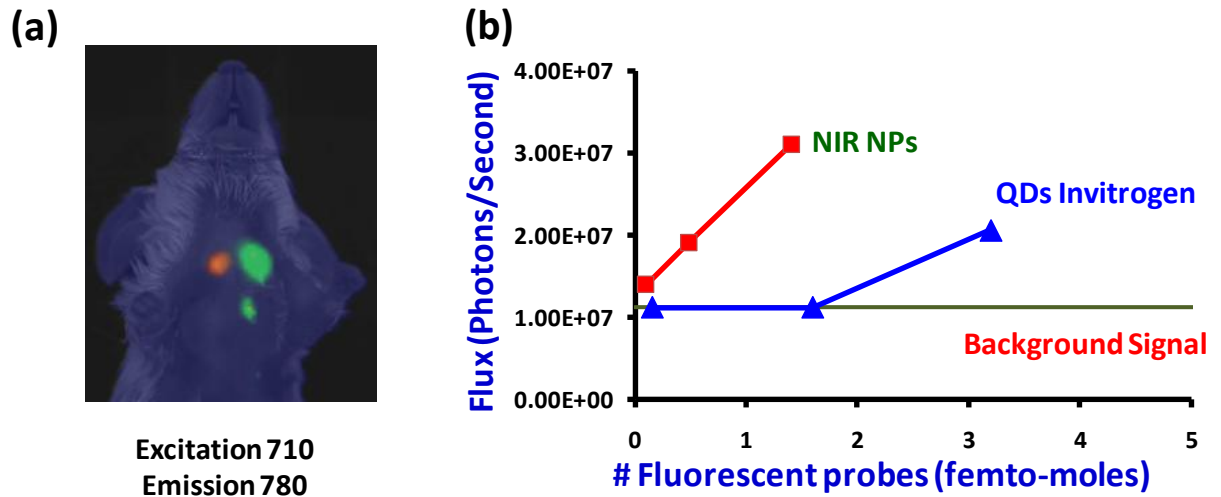


Figure 3-7. (a) In vivo demonstration of sensitivity of NIR dye doped nanoparticles (green) and invitrogen QDs (orange), (b) Calculation of minimum number of probes that can be detected from the photon flux obtained from Xenogen.

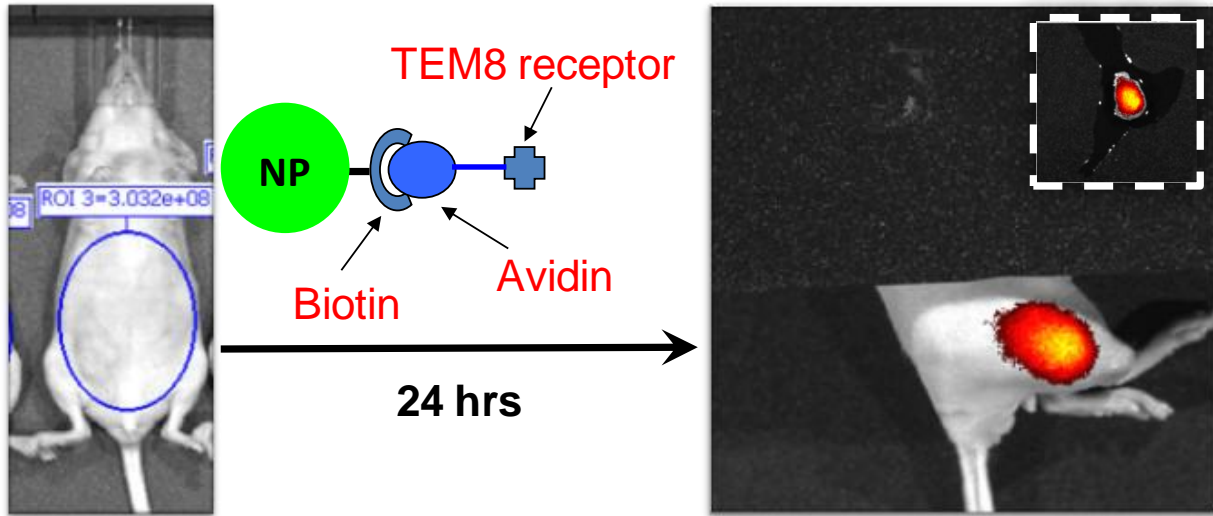


Figure 3-8. Demonstration of in vivo targeting using TEM8 receptor functionalized NIR silica nanoparticles. Fluorescence image on right shows accumulation of particles in tumor 24 h post injection (inset: image of tumor after mouse was sacrificed).

CHAPTER 4 PLASMONIC GOLD SPECKLED SILICA NANOPARTICLES

In this chapter, a new approach for the incorporation of NIR photothermal materials in silica nanoparticles is described, with a view to translate the developed strategy to fluorescent silica nanoparticles.

4.1 Photothermal Materials: Current Status and Limitations

As mentioned in chapter 1, several photothermal nanomaterials are actively being pursued for cancer therapy. Amongst these, gold based nanomaterials have attracted particular attention due to their size and shape dependent plasmonic properties that allows them to absorb and scatter light in the visible to NIR region (optical tunability). Although gold based plasmonic materials possess optical tunability, they lack size/shape tunability. In other words, for a desired optical property such as NIR absorbance only limited shape and size of particles can be achieved due to experimental limitations. For example, synthesis of nanoshells in the sub 100 nm size ranges faces severe challenges due to the requirement of sub 5 nm continuous gold coating on the surface and increased agglomeration because of enhanced van der Waals forces⁸². Although the “right” particle shape and size for nanomedicine applications is still debatable, recent research results have demonstrated that sub 100 nm particles offer substantial advantages for targeting sub cellular processes³⁹. For drug delivery applications 100 nm size particles are barely better than the free drug molecules⁸³⁻⁸⁵. However, particles in the size range 30-50 nm are indicated to be most suitable for tumor targeting applications⁸⁶.

In order to overcome the size/shape restrictions associated with currently used gold based nanomaterials, Zharov et al.⁸⁷⁻⁹⁰ have used clusters of small (10-30 nm) gold

nanoparticles. The interplasmon coupling amongst adjacent gold nanoparticles causes a red shifted plasmon band⁹¹⁻⁹⁴. For example, formation of nanoclusters of gold nanoparticles result in the shift in absorbance peak of single gold nanoparticles from ~525 nm to 700-1000 nm⁸⁹. Gold nanoclusters based on their spatial distribution could potentially combine optically induced thermal, acoustic, and bubble formation effects in a synergistic manner to improve the outcome of diagnostic and therapeutic interventions⁹⁰. The effectiveness of gold nanoclusters has been demonstrated for *in vitro* applications⁸⁸. These clusters upon exposure to NIR pulse or continuous laser are found to be effective in killing tumor cells *in vitro*. Several strategies were suggested to form clusters of gold nanoparticles in living systems. For example, formation of controlled self assembly of monodispersed gold nanoparticles within living cell, after their delivery to the targeted sites such as tumor cells for photothermal therapy purposes. However, *in vivo* realization of this approach has remained elusive so far, primarily due to failure in achieving *in vivo* cluster formation in a controlled manner.

4.2 Proposed Approach: Controlled Deposition of Plasmonic Materials

In this work a modified approach based on Zharov's work was developed for the synthesis of NIR absorbing plasmonic nanoparticles. It was hypothesized that controlled deposition of small gold nanoclusters on the surface of silica nanoparticles would result in the NIR absorbance due to interplasmonic coupling between gold nanoparticles. Once developed, this strategy was used to impart NIR photothermal properties to fluorescent dye doped silica nanoparticles. Extremely small (sub 5 nm) gold nanoparticles were employed for developing this strategy, so that the overall composite particle is not limited by the size and shape of an individual component. In the next

sections, a brief overview on current status of controlled deposition of metal nanoparticles on silica surface is described.

4.3 Controlled Deposition: Current Status

Controlled deposition of metal nanoparticles on surfaces is of prime importance for many biological (biosensing, surface enhanced Raman spectroscopy (SERS), photothermal ablation)^{39,95-97} as well as non biological applications such as catalysis⁹⁸, and nanoelectronics⁹⁹. Charged metallic particles form well separated 2D arrays on planar substrates due to interparticle electrostatic repulsion¹⁰⁰. Control of nanoparticles size, shape, environment and their interspacing governs their overall chemical and physical properties that often are very different from their bulk counterpart. For example, optical properties such as surface plasmon resonance (SPR) and SERS rely on nanoscale features of gold and silver surfaces and catalytic properties of gold nanoparticles deposited on metal oxides are controlled by the size and shape of particles^{98,101}.

Ordered nanoparticles on a planar substrate are being investigated actively for SERS applications. Random aggregates of particles on surfaces lead to the uncontrolled and often unfavorable changes in their size and shape dependent optical properties¹⁰². Several methods have been developed for controlled and aggregation free deposition of gold nanoparticles on planar silica substrates^{103,104}. So far, much less attention has been paid to control the deposition of nanometer size gold on surface of larger size nanoparticles. However, for many applications use of nanoparticles is preferred instead of planar surfaces due to the requirement of large surface area. Agglomeration free and controlled coating of gold nanoparticles on submicron particles is a challenging task. Traditionally, self assembly of gold nanoparticles on submicron

silica surfaces is obtained by either covalent or electrostatic attachment of metallic gold nanoparticles to the organosilane functionalized silica surface¹⁰⁵. Hydrophilic functional group mainly comprising of amines and thiols were coated on silica nanoparticle surface for the attachment of small 1-3 nm gold nanoparticles. Conventionally used methods for the synthesis of these composite nanoparticles are based on mixing of gold and silica colloids. Using this method, control of interparticle spacing and surface coverage is challenging due to the random collision based mechanism of the deposition process. Moreover, composite particles formed by this method lack homogeneity in the overall composition.

4.4 Controlled Deposition: A New Approach

In this research work our aim was to control the assembly of gold nanoparticles on the surface of sub 50 nm size silica particles. For this purpose a novel precipitation-deposition method was developed in the constrained environment of aqueous nanocontainers of reverse micelles. In the precipitation-deposition approach gold-silica nanocomposite were synthesized by first depositing a positively charged gold-ammonia complex, fulminating gold (FG), on the surface of silica particles. Using this method large amount of gold could be deposited in a controlled fashion without destabilizing the microemulsion environment. Subsequently, the gold-complex deposited on the silica surface is reduced to metallic gold form. Synthesis of gold-silica composite nanoparticles by incorporating precipitation-deposition method in microemulsions provides several advantages over the conventionally used methods: (i) this is a one pot synthesis method for the formation of monodisperse gold-silica composite nanoparticles; (ii) synthesis in microemulsion environment provides excellent control over deposition of gold by homogeneous mixing of reactants; (iii) the size of silica

nanoparticles can be tuned precisely over a large range from 30 nm to greater than 150 nm; (iv) the size (1-5 nm) and surface coverage (5-20%) of deposited gold nanodomains can be controlled by either varying the molarity or the volume of the added gold chloride solution; (v) this approach provides aggregation free high surface coverage of gold nanoparticles deposited on well dispersed sub 50 nm silica nanoparticles. Additionally, (vi) this one pot microemulsion synthesis approach allows handling and precise control of composite particles at relatively high concentrations ($\sim 1 \times 10^{13}$ particles/ml compared to $\sim 7 \times 10^{10}$ particles/ml used commonly).

4.5 Results and Discussion

Reverse micelles have been used as nanocontainers to synthesize monodisperse nanomaterials by mixing the reactants down to the molecular level^{106,107}. Uniform mixing of the reactants at the molecular level in a constrained environment provides excellent control over the particle size and homogeneity¹⁰⁸. Microemulsions have been used for the synthesis of metal, ceramic, semiconductor, and composite nanoparticles¹⁰⁹. Composite nanoparticles synthesized by microemulsion methods primarily include silica coated metal nanoparticles. Owing to their high surface energy, synthesis of noble metals like gold and silver nanoparticles leads to their agglomeration inside microemulsions¹¹⁰. Due to the agglomeration issues there are limited number of reports on the synthesis of oxide supported metal nanoparticles synthesized by microemulsion technique. In this work we report a novel method for the synthesis of gold coated silica nanoparticles by one pot microemulsion synthesis.

First silica nanoparticles were synthesized by the ammonia catalyzed hydrolysis of TEOS in a quaternary microemulsion system. In this system size of silica particles can be precisely controlled by changing the water to surfactant molar ratio or by changing

the concentration of ammonia in aqueous phase¹¹¹. Once the silica particles are formed their surface was modified by the deposition of gold speckles. When gold chloride solution is added to the microemulsion, it forms surfactant stabilized nanometer size droplets. The gold chloride present in these newly formed droplets forms a gold-ammonia complex upon collision with silica nanoparticles surrounded by ammonia environment. This gold-ammonia complex was identified as fulminating gold (FG) in many previous reports¹¹². Fulminating gold is positively charged and deposits on the surface of silica nanoparticle by electrostatic attraction. Positively charged FG nanoparticles electrostatically repel each other thereby yielding a speckled coating on the silica particle surface instead of a continuous coating. The surface of silica nanoparticles becomes positively charged after the coating process. Upon addition of a reducing agent, gold ammonia complex reduces to metallic gold nanodomains speckled on silica surface (figure 4-1(a)). As a result of reduction of FG to metallic gold, the overall charge of the composite particles becomes negative (Table 4-1). The change in extinction spectra of GSS particles at different time periods during the synthesis was monitored (figure 4-1(b)). Silica nanoparticles do not scatter or absorb light significantly in the visible region of electromagnetic spectrum and hence have very small extinction coefficient. Upon addition of gold chloride in the microemulsion, extinction coefficient of composite nanoparticles does not change significantly in the visible region. In the UV region of the spectra, increase in extinction was observed due to the formation of FG on silica particle surface. The extinction spectra of microemulsion after addition of reducing agent show a distinct peak at 530 nm. This peak indicates the formation of metallic gold

by the reduction of gold-ammonia complex formed during the previous step. After 530 nm the extinction remains constant throughout the entire region of the spectra.

To demonstrate the role of precipitation as a necessary mediator for the synthesis of GSS particles, gold deposition experiments were performed in the absence of NH_4OH . Upon removal of ammonia by purging N_2 gas, the pH of microemulsion changed from 9 to 6. In absence of ammonia, gold chloride containing droplets did not form precipitate (gold-ammonia complex) and were diluted because of mixing with the water already present in the microemulsion. Addition of reducing agent to this system caused formation of 10-20 nm size gold particles that either randomly deposited on the surface of silica particle or remained isolated in the suspension. The corresponding extinction spectra of a mixture of silica and gold nanoparticles shows single peak at 530 nm and extinction decreases significantly afterwards at longer wavelengths (figure 4-2(a)). Further, upon re-addition of ammonia after its removal from microemulsion formation of gold speckled silica nanoparticles was observed. In this experiment after removal of ammonia, gold chloride solution was added first and then ammonium hydroxide was added in the microemulsion. Figure 4-2(b) shows the similar nature of extinction spectra as was observed for GSS (figure 4-1(b)), indicating that ammonia is required for the formation of gold specks on silica particle surface.

In order to further prove the precipitation-deposition hypothesis silica particles were synthesized in microemulsion by using NaOH as a catalyst instead of ammonia. When gold chloride was added to this system it did not form any precipitate. Upon addition of reducing agent large size gold nanoparticles (10-20 nm size) formed as in above case and were deposited on silica surface. These two sets of particles exhibited

surface plasmon peak in the range 530-550 nm due to the formation of large gold nanoparticles on the surface of silica. There was no absorbance observed in the NIR region of the electromagnetic spectra due to the spherical shape of the gold particles. Figure 4-2(c) shows TEM image and the corresponding extinction spectra of silica nanoparticles formed by using NaOH as a catalyst instead of NH_4OH . NaOH did not form any precipitates with gold chloride solution at the concentrations used in this experiment. In absence of precipitation, addition of reducing agents in microemulsion resulted in the formation of a mixture of gold and silica nanoparticles as was observed for the particles synthesized by removing ammonia from the microemulsion. The mechanism of formation of GSS nanoparticles by precipitation-deposition method, mediated by fulminating-gold, is schematically depicted in figure 4-3.

Understanding the mechanism of GSS formation led to the successful control on self assembly of gold nanoparticles on silica nanoparticle surface. Both size and interparticle distance of gold nanoparticles was controlled by either varying the molarity or volume of gold chloride added during the synthesis. With the increased molarity of gold chloride, size of the deposited gold particles increased and the spacing between them decreased. Figure 4-4(a-c) show HRTEM micrographs of gold speckled silica nanoparticles synthesized by one pot microemulsion method. It is observed that surface of these particles is uniquely speckled with the nanodomains of gold that are highly dispersed on the surface. The size of these gold nanodomains varies between 1-5 nm and their size can be controlled by changing the molarity of gold chloride solution. An increase in size of deposited gold specks was observed with the increase in molarity of gold chloride solution (figure 4-4(a-c)). For this synthesis 125 μl of gold chloride solution

with three different molarities (0.25M, 0.5M, and 1.0M) was added into the microemulsions. The particle size distribution of the gold speckles deposited on silica surface was obtained by analyzing the HRTEM images of nanoparticles (figure 4-4(d)). At least 100 nanoparticles were analyzed for GSS synthesized using each method. Similarly increasing volume of gold chloride resulted in higher surface coverage by gold nanoparticles. In both cases decreasing the distance between the gold nanoparticles caused inter-particle plasmon coupling primarily between nearest neighbors⁹¹. The effect of plasmon coupling can be seen by the broadening of low energy band extending in the NIR region. Figure 4-4(a-c) shows the increase in surface coverage by gold nanoparticles with the increasing volume (100, 200, 300 μ l) of gold chloride solution (0.5M) added into the microemulsion. The size of the deposited gold nanoparticles is similar in all three cases. It should be noticed that even at the highest surface coverage there is no observable aggregation of gold nanoparticles on the surface. Corresponding UV-VIS spectra show increase in absorbance with the increase in surface coverage by gold nanoparticles (figure 4-4(d)).

4.6 Summary

In summary we have demonstrated a new method for the deposition of gold nanoparticles on the surface of silica nanoparticles. Conventional methods for the deposition of gold on silica surface face severe challenges due to aggregation of gold at higher concentrations and lack of control on deposition process. To the best of our knowledge, this is first report where fulminating gold was first formed as a mediator for the formation of metallic gold nanostructures. The positive charge on the FG makes it highly suitable for its deposition on negatively charged surfaces like silica, titania, etc. In addition, this method in combination with microemulsion environment provides excellent

control over gold nanoparticle size and surface coverage on silica nanoparticle surface. Another advantage of using FG as a mediator for the synthesis of pure gold or gold-silica composite is that FG can be handled at very high concentrations without dealing with any agglomeration issues. Hence, the present approach could be very useful for applications requiring large scale synthesis of gold nanoparticles. Using this novel method, size and surface coverage of the deposited gold nanoparticles was controlled on silica surface. Decreasing the spacing between gold nanoparticles allow them to have absorbance in the NIR region of electromagnetic spectrum. In the next chapter their unique photothermal properties that facilitate the use of these materials as NIR photothermal ablation agents will be discussed.

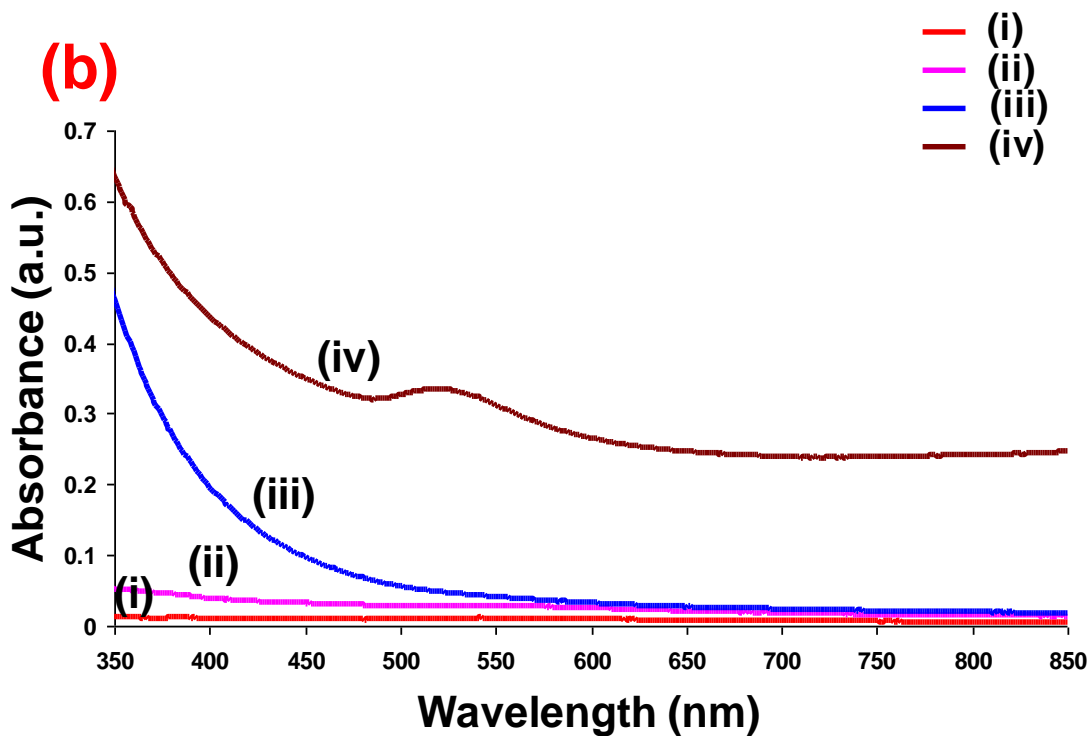
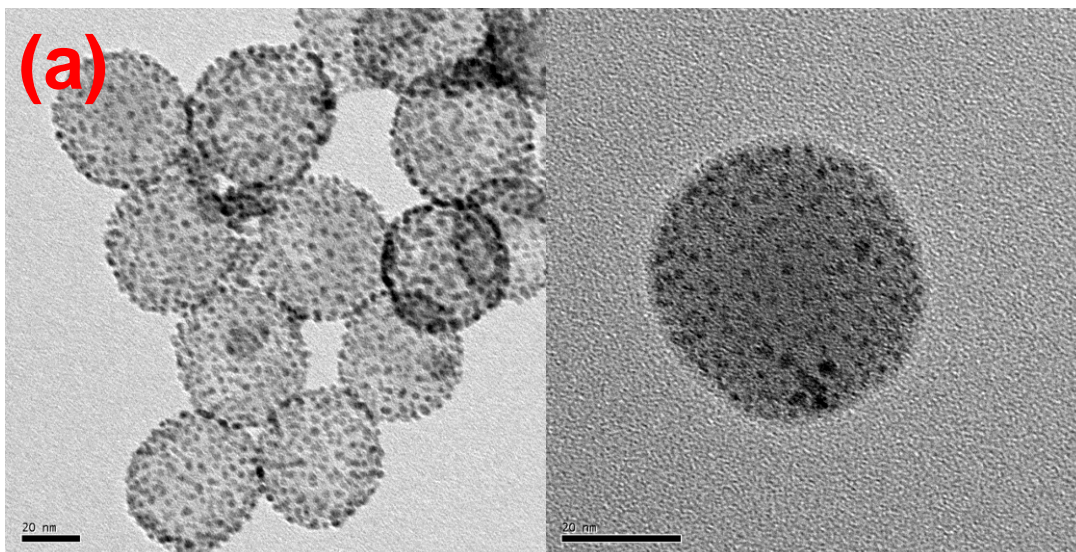


Figure 4-1. (a) Representative TEM images of GSS nanoparticles at different magnifications (scale bar represent 20 nm). (b) extinction spectra of the microemulsion at different stages of synthesis (i) microemulsion alone (ii) silica nanoparticle formation (iii) fulminating gold formation (iv) GSS nanoparticle formation. Extinction spectrum of GSS nanoparticles shows a plasmon peak at 530 nm and a broad absorption peak in the NIR region.

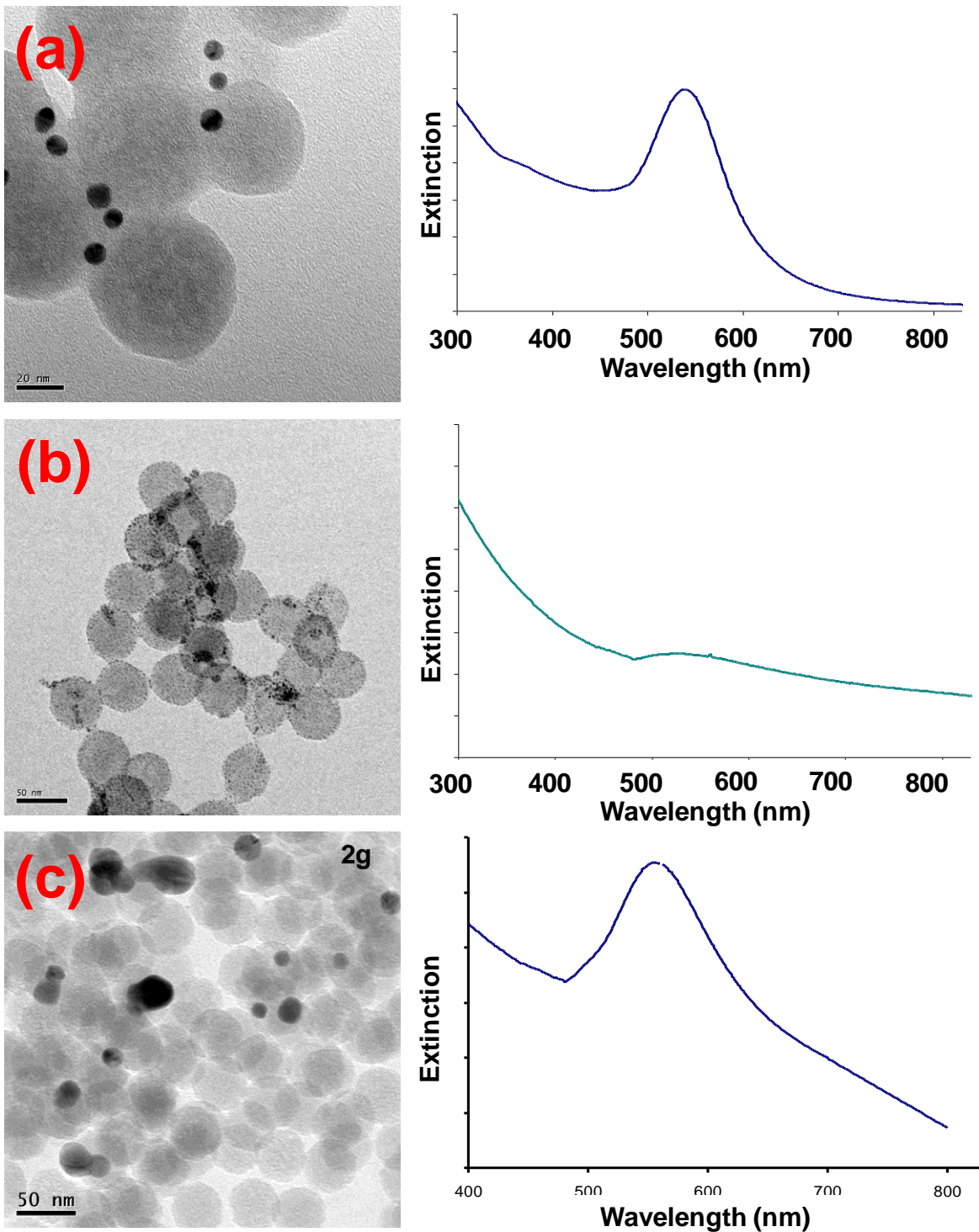


Figure 4-2. TEM images and the corresponding extinction spectra of gold-silica composite nanoparticles formed using different methods (a) after removing ammonia (b) upon re-addition of ammonia and (c) using sodium hydroxide as catalyst.

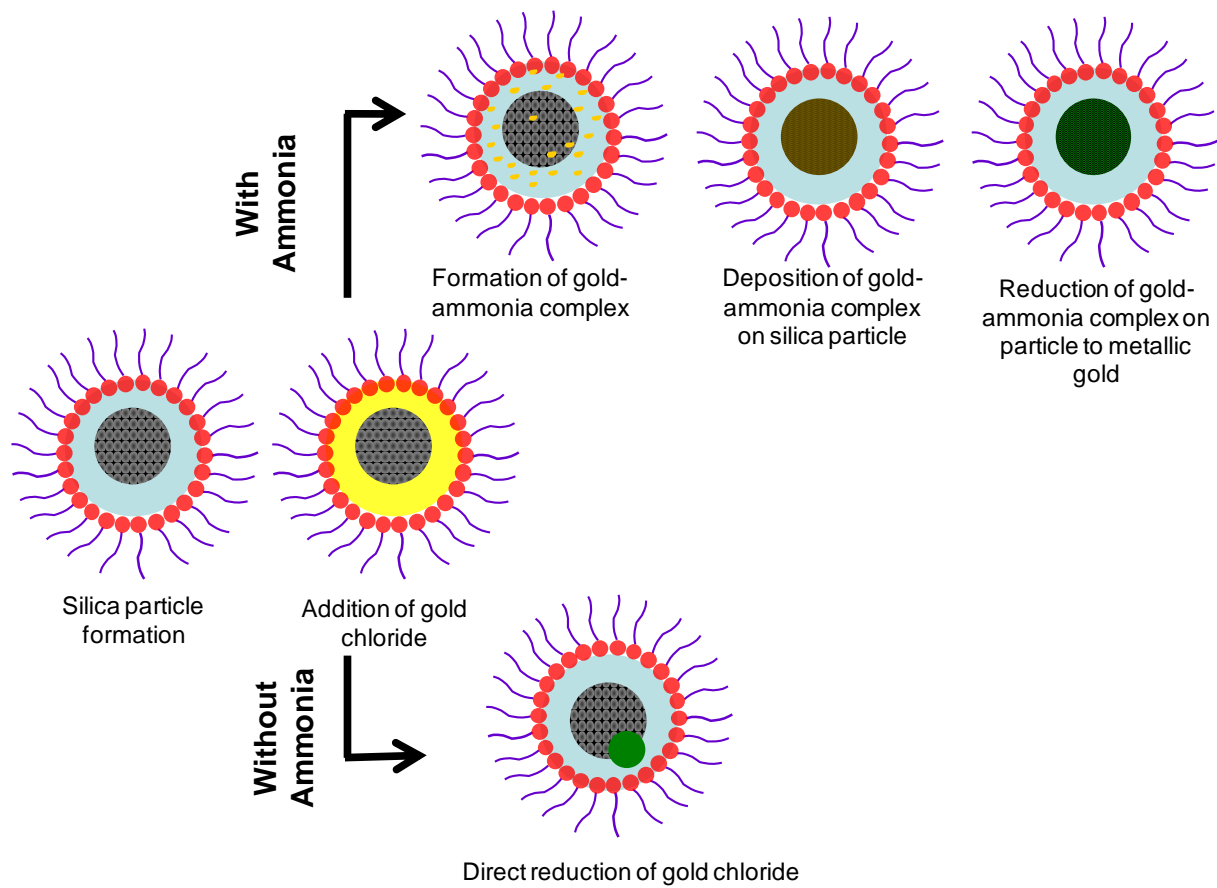


Figure 4-3. Schematic of proposed GSS formation mechanism.

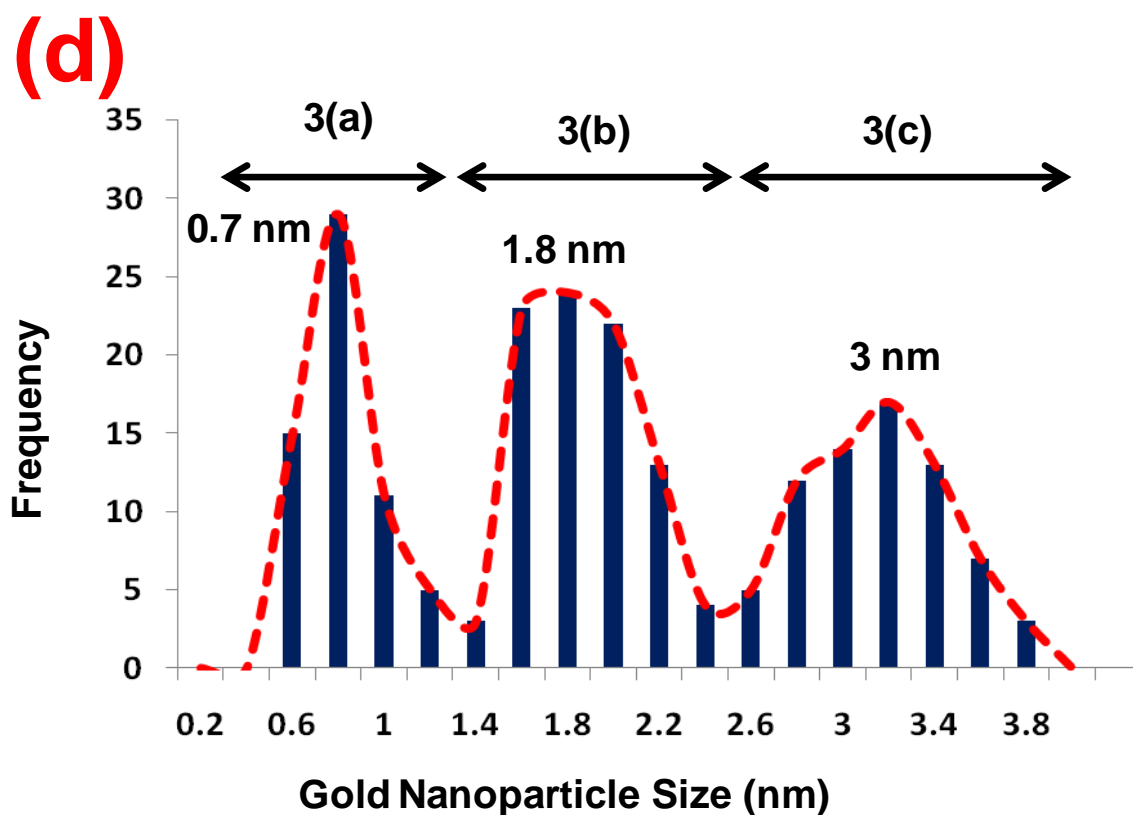
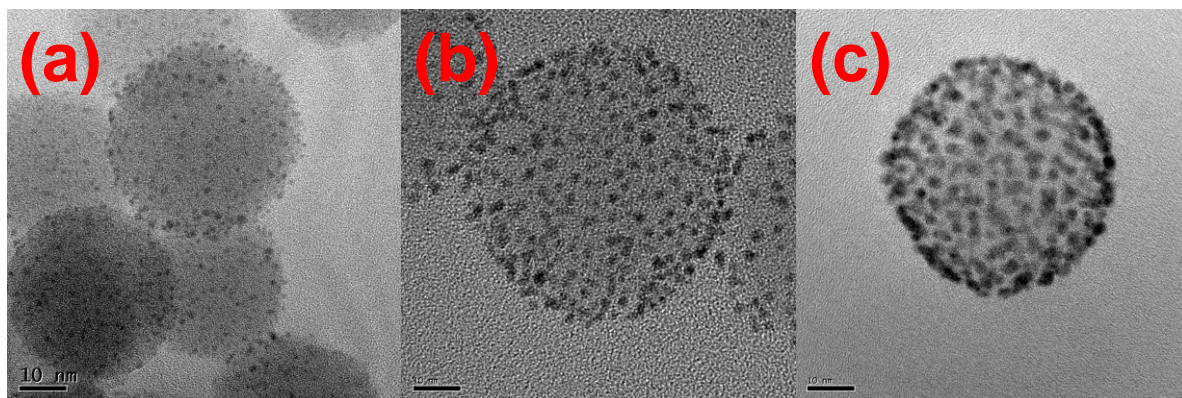
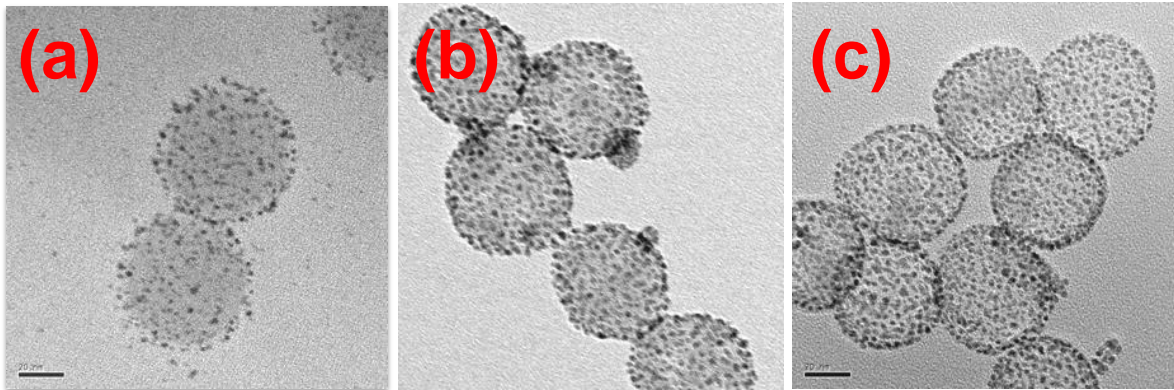


Figure 4-4. TEM images of GSS nanoparticles synthesized using different molarity of gold chloride solution (a) 0.25M (b) 0.5M and (c) 1.0M. Scale bar represents 10 nm in all images. (d) Corresponding particle size distribution of gold nanoparticles on the surface of silica nanoparticles. Particle size was analyzed using HRTEM images at high magnification.



	Volume of 0.5M gold chloride solution	# Gold particles	Surface coverage
4(a)	100 μ l	113 (\pm 19)	6%
4(b)	200 μ l	251 (\pm 21)	13%
4(c)	300 μ l	376 (\pm 26)	20%

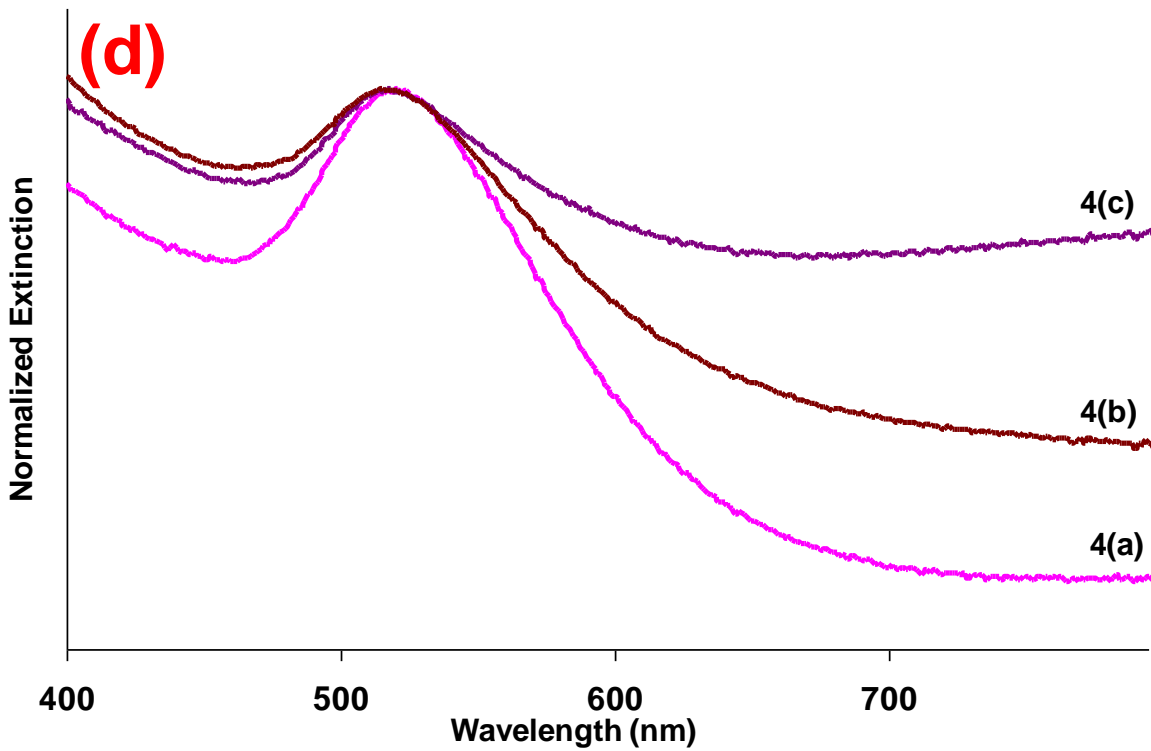


Figure 4-5. TEM images of Gold speckled silica nanoparticles synthesized using different amount of gold chloride solution. (a) 100 μ l (b) 200 μ l (c) 300 μ l. Scale bar represents 20 nm in all images. 4 (d) Extinction spectra of GSS nanoparticles synthesized using different molarity of gold chloride solution.

Table 4-1. Zeta potential (at pH 7 in 1 mM KCl solution) of GSS nanoparticles synthesized using different amount of 3-aminopropyltriethoxysilane (APTS)

Particle	APTS (μ l)	Zeta Potential (mV) Before Coating	Zeta Potential (mV) After Coating	Zeta Potential (mV) After Reduction
GSS	10	-24	20	-15
GSS	20	-12	35	-21
GSS	30	+7	38	-20

CHAPTER 5 APPLICATION OF GSS FOR OPTICAL IMAGING AND PHOTOTHERMAL THERAPY

The size and shape independent optical tunability in gold speckled silica nanoparticles was achieved by utilizing the interplasmonic coupling between nearest neighbor particles when deposited on silica surface. GSS nanoparticles have a silica core whose surface comprises of discontinuous, irregular gold nanodomains, incorporated on the silica exterior and within the pores of the supporting matrix. The multitude of dielectric-metal interfaces and interplasmonic coupling present in the particles makes them absorb a broad spectrum of light from visible to NIR region. These particles upon photoexcitation, generate localized heat due to conversion of photons to phonons through nonradiative decay. In therapeutic applications localized temperature rise of as low as 4 °C is effective in causing cell death by necrosis.

In this chapter, NIR absorbance of GSS nanoparticles was utilized for demonstration of their photothermal properties. Both *in vitro* and *in vivo* experiments were performed to show selective photothermal ablation of tumor cells due to the localized heat generated by the particles. In addition, like other gold based photothermal materials, these particles can be imaged by various optical imaging methods based on their absorbance and scattering properties. Some of the imaging modalities that are generally used include optical coherence tomography, diffuse optical tomography and photoacoustic tomography (PAT). In this study, PAT was used for non-invasive *in vivo* imaging of GSS nanoparticles.

5.1 Therapeutic Properties of GSS

5.1.1 Selection of Particle Size for Photothermal Applications

In contrast to conventionally used gold based photothermal agents, the size of GSS nanoparticles can be tailored to meet the varying particle size requirement for different biological applications. Larger sized particles are prone to rapid clearance from circulation in to liver and spleen and are mostly restricted to the tumor vasculature, the smaller (< 100 nm) particles escape reticuloendothelial system (RES) uptake and permeate into tumor tissues⁴⁵. There is growing evidence that particles in the size range 30-50 nm are preferentially uptaken by tumor cells^{49,113}. In this study, 40 nm GSS nanoparticles were selected for cancer theranostics applications such as tumor targeting, imaging and photothermal ablation. The scanning electron microscope and transmission electron microscope images of 40 nm GSS nanoparticles used in this study are shown in figure 5-1(a) along with their particle size distribution (figure 5-1(b)).

5.1.2 NIR Photothermal Ablation Properties of GSS(*in vitro*)

The broad extinction spectra of the GSS nanoparticles indicate the NIR light absorbing ability of the particles (figure 4-1(b)). The ability to generate heat thereof was tested by measuring the temperature increase of the GSS nanoparticles solution on illumination with NIR light. Using a 785 nm peak wavelength CW NIR laser (output 350 mA) incident on cuvette containing 2 ml (of 10 mg/mL) pegylated GSS nanoparticles for 5 min. A rise in temperature of nearly 15°C (SD ±3) was observed in 5 min on continuous illumination of GSS nanoparticles (figure 5-2). The temperature increase was found to be rapid in first two minutes followed by a decrease in the rate of temperature increase.

After characterizing the heating capability of the GSS nanoparticles, their photothermal ability was demonstrated with the lung A549 cancer cell line. The procedure used for dosing of the cells with the particles has been described in complete detail in chapter 2. The particle uptake experiments were followed by the *in vitro* photothermal ablation of lung A 549 cells using the NIR laser present on the Renishaw InVia Raman Instrument. The low power NIR laser on the Raman Instrument does not cause any damage to the cells even under prolonged exposure times. Additionally the small size of laser spot (20X40 μm), with orientation parallel to the scanning direction, assured that heat diffusion would not exceed beyond two cell wide area (approximately 50 μm). GSS nanoparticles labeled cells were exposed to NIR laser along a linear path followed by cell viability test with trypan blue. Cells exposed to high temperatures can undergo a rapid necrotic death with membranes permeable to trypan blue dye. Figure 5-3(a) and 5-3(b) (magnification) shows the dead cells as stained blue by trypan blue along the path of laser movement, with minimal collateral damage. Only the cells exposed to the laser illumination were found dead and the surrounding cells remained viable. This experiment also demonstrates that the cell death would be selectively limited only to cells labeled with the GSS nanoparticles. This indicates that the localized rise in the temperature of GSS particles leads to the injury and eventual death of the cells. Localized heating achieved with plasmon resonant particles is believed to be the main cause of cell death on exposure to NIR light.

5.1.3 NIR Photothermal Ablation (*in vivo*)

The ability of nanoparticles to induce photothermal ablation *in vivo* is challenging because of issues such as absorbance and scattering by the surrounding tissue, dispersion state of particles, depth and spread of particles, and the wavelength of laser

employed. To evaluate the performance of the GSS nanoparticles to mediate thermal ablation *in vivo*, GSS nanoparticles (300 µg in saline) or saline controls were injected intratumorally into nu/nu mice bearing human breast cancers. Figure 5-4 (a) illustrates a typical experimental setup for photothermal ablation experiments. The tumor region was irradiated with NIR laser (output 350 mA; 500 mW) for 10 min. Figure 5-4 (c) shows ca. 60% necrosis in tumors with GSS nanoparticles and NIR ablation as compared to ca. 30% necrosis in control experiments ($p = 0.001$). It should be noted that the BT474 xenograft tumor model applied in the current research develops a central region of necrosis during tumor progression. Microscopic examination of the untreated BT474 tumors by hematoxylin and eosin (H & E) staining revealed nodular masses composed of large epithelioid cells with pleomorphic nuclei, prominent nucleoli, and numerous atypical mitotic figures. Areas with individual cell necrosis and impending frank necrosis were significantly increased upon tumor ablation with GSS nanoparticles (figure 5-4(b)) as compared to controls (figure 5-4(d)).

5.2 Optical Imaging Properties of GSS Nanoparticles

5.2.1 Photoacoustic Imaging

To investigate the potential of GSS NPs for detection of cancers, their photoacoustic (PA) properties were characterized. Photoacoustic imaging takes advantage of high optical absorption property of gold nanoparticles. Photoexcitation of gold nanomaterials is followed by their subsequent thermoelastic expansion, generating an acoustic signal that can be detected for imaging purposes. GSS NPs were embedded in a phantom at a depth of 10 mm, constructed using Indian ink and 2% agar solution to simulate tissue like extinction. The phantom and acoustic transducer (used for collecting the imaging signal) were immersed in a water tank where it was

illuminated with a Ti:sapphire tunable pulsed laser (See chapter 2 for the details of the experiment). Figure 5-5(a-c) shows photoacoustic images of GSS nanoparticles at increasing concentrations. The photoacoustic signal from GSS nanoparticles was ~18 times higher when compared to the signal from standard photoacoustic contrast agent (Indocyanine green dye) at the same concentration. Bright yellow region with respect to red background shows the relative strength of the photoacoustic signal from the particles (figure 5-5(a-d)).

The potential of GSS NPs as contrast agents for *in vivo* tumor imaging was determined by administering PEGylated gold nanoparticles using PA imaging. For these experiments, breast cancer tumor model inside a mouse was used. Mice were subcutaneously inoculated with 2×10^7 BT474 cells (human breast cancer cells) on the abdominal wall. Experiments were conducted after the tumors had reached approximately 10 mm in size. A volume of 100 μ L of GSS nanoparticle suspension (10 mg/ml) or control saline solution was injected into the tail vein of mouse. The accumulation of PEGylated GSS nanoparticles (40 nm size) inside tumors following systemic administration is expected to occur via an enhanced permeability and retention (EPR) effect. PAT images of mouse tumor were obtained before and after injecting nanoparticles. After 5 hr, the anesthetized mouse was imaged again and the obtained images were reconstructed using inverse algorithm. The accumulation of GSS nanoparticles inside tumor can be visualized in the PA image (figure 5-6(b)). GSS nanoparticles provide excellent contrast between the tumor and surrounding background tissue and have potential to be used in image guided therapy applications. Tumor injected with saline did not show any contrast (data not shown).

5.2.2 Photoacoustic Imaging: Limitations

Although a wide variety of experiments have been performed using gold-based nanomaterials for advanced optical imaging such as PA imaging¹¹⁴⁻¹¹⁷, many questions remain unanswered. For instance, there is lack of information about the quantity of cellular uptake, dosimetry response, movement of particle within cells in *in vitro* studies and establishing distribution of the particles in the tumor vasculature, capillaries, within the necrotic zone, etc., in *in vivo* systems. For comprehensive investigations of these or any other materials in biological systems it is essential to track and image the particles at all times. This could imply monitoring particle uptake at the cellular level, tissue (delivery) and/or the whole body levels. In context of photothermal ablation studies, one of the major limitations of these materials is the ability to image the particles in the tumor region post treatment, performed either by systemic delivery or by direct intratumoral injections. In addition, some of the above mentioned approaches for imaging require specialized instruments for investigations limiting their broad applicability. Therefore, new materials are required to overcome these limitations enabling particle monitoring utilizing widely available instrumentation for facilitating the advancement of nanoparticle-mediated photothermal therapies. Design and synthesis of one such nanomaterial by incorporating fluorescence imaging modality in the GSS nanoparticles is discussed in the next section.

5.3 Luminescent GSS Nanoparticles

For the synthesis of luminescent GSS nanoparticles, fluorescent silica core was first prepared in the microemulsion following the procedure as described earlier using TEOS and APTS-dye conjugates. By using the APTS-fluorescent dye (FITC, Rhodamine, NIR dyes etc) conjugate as one of the precursor in the silica nanoparticle

synthesis, the dyes were covalently coupled in the silica matrix during the hydrolysis and condensation of silanes. The covalent coupling prevents the leaching of the dye from the nanoparticles in biological environments, thus minimizing its contribution to background signal. After the particle formation gold specks were deposited on these particles, using the method described in chapter 4. A distinct feature of the GSS nanoparticles is the discontinuous speckled surface. This is uniquely different from the other NIR absorbing gold nanomaterials such as nanoshells, nanocages, nanorods which present a continuous gold surface. Although the plasmonic property of the gold is known to interact in a complex way with any surrounding fluorescent molecules and in most examples it quenches the fluorescence, the discontinuously speckled GSS doped with high quantum yield fluorescent dyes (QY: FITC = 98%, Rhodamine= 95%) remain brightly fluorescent. The photoluminescence of these particles decreased with the increasing amount of gold speckled on silica surface. The discontinuous gold deposits, as opposed to a continuous gold film, are hypothesized to inhibit complete quenching of the fluorescence of the dye partly due to increased transmission. In case of low quantum yield dye (QY < 40%) such as NIR dyes (IR780, IR820 etc) complete quenching of fluorescence was observed at the surface coverage of gold required to have the desired photothermal efficiency (figure 5-7(a,b)).

In many previous reports, it has been demonstrated that increasing the separation between dye molecules and gold nanoparticles results in decrease in fluorescence quenching. It was hypothesized that increasing the distance between gold specks and dye doped silica core would also result in similar effect. This separation between gold specks and silica core was achieved by postcoating of few nanometer thin silica layer

on dye doped silica core. Varying amount of TEOS and ammonia were added in order to achieve varying thickness of silica shell. After post-coating of silica shell, gold was deposited on core-shell silica nanoparticles. The thickness of coating and amount of gold deposited was optimized in such a way that the resulting particles retain both NIR fluorescence and NIR photothermal properties (figure 5-7(c)).

5.3.1 *in vitro* Fluorescence Experiments

Figure 5-8 shows the confocal image of the lung cancer cells (A549 cancer cell line) labeled with the FITC doped GSS nanoparticles. The green fluorescence from FITC doped GSS nanoparticles shows their presence inside the cells surrounding the nucleus (stained with the blue dye). Figure 5-8(a) indicates the presence of GSS nanoparticles near the nucleus of the cell. This can be observed more definitively in figure 8(b) which shows the z-stacked cross sectional image of the GSS labeled cells. The ability of the GSS nanoparticles to traffic to the nucleus can be an important tool for cellular therapy and genetic transformation. In separate experiments the GSS nanoparticles uptake by the breast cancer cells was analyzed quantitatively as a function of particle dosage by flow cytometry. For this experiment, BT474 cells were treated with FITC labeled GSS nanoparticles and the particle uptake was performed 24h post exposure. A dose dependent uptake of GSS was observed by the cells (figure 5-9). These experiments clearly demonstrate the ability to perform standard fluorescence based lab procedures with GSS nanoparticles to estimate particle uptake/dosimetry and to monitor intracellular localization.

5.3.2 *in vivo* Fluorescence Experiments

NIR dye doped GSS nanoparticles were employed for the *in vivo* fluorescence imaging demonstration of GSS nanoparticles. These particles were imaged using

fluorescence imaging at different point of time after intratumoral injection of 30 μ l (10 mg/ml) nanoparticles. Figure 5-10(a) and (b) show fluorescence images of mice 5 min and 24 h after the nanoparticles injection. It is clear from the image that pegylated GSS nanoparticles move from the tumor site to lymph nodes within 24 h time period. This example clearly demonstrates the potential of GSS nanoparticles for *in vivo* particle monitoring/tracking applications. The knowledge of fate and transport of nanoparticles during and after tumor ablation is of importance for developing therapeutic agents for cancer.

5.4 Next Generation of GSS: Inverse Architecture for 3D Plasmon Coupling

The photothermal performance of GSS can be enhanced by utilizing the 3D coupling between the gold nanoparticles. We hypothesized that the controlled aggregation inside a solid matrix would also lead to the formation of NIR absorbing nanoparticles. Our research approach was divided in two parts we first formed clusters of gold nanoparticles in a solution followed by their encapsulation in a silica matrix. We have used reverse micelles based nanocontainers in microemulsions for the synthesis of ultra small (sub 5 nm) fulminating gold nanoparticles. In general microemulsions are very sensitive to the addition of high strength acid or base solutions. It was observed that Tx-100/nhexanol/cyclohexane based microemulsions are relatively insensitive to acidic gold chloride and basic ammonia solutions. These microemulsions remain stabilized even after the addition of 5-6 M acidic gold chloride solutions. For the synthesis of internally gold speckled silica (IGSS) nanoparticles, up to 1M strength gold chloride solution was used. Upon addition of ammonia to this microemulsion, color of the microemulsion changed from bright orange to pale yellow. The change in color indicating the formation of sub 5 nm FG particles (formation of FG nanoparticles was

also confirmed by destabilizing a part of microemulsion at this stage). Different volume of 1M gold chloride solution was added in the microemulsion to control the number of FG nanoparticles formed inside each nanocontainer. The average number of FG nanoparticles in each nanocontainer can be increased by increasing the volume or molarity of gold chloride added in the synthesis. After the synthesis of clusters of well dispersed FG nanoparticles next challenge was their incorporation in a biocompatible matrix. Fulminating gold nanoclusters were coated in situ by the addition of a silane precursor, TEOS, in the microemulsion. Unlike metallic gold these particles are positively charged, coating with negatively charged silica was easily achieved. By varying the amount of TEOS added, different thickness of silica coating was achieved. Resultant particles were washed with ethanol and water using centrifugation and redispersion method. Washed and surfactant free nanoparticles were dispersed in nanopure water. Upon addition of small amount of sodium borohydrate, the encapsulated fulminating gold gets reduced to metallic gold. By varying the amount of gold chloride added during the synthesis of these nanoparticles, different number of gold nanoparticles can be encapsulated inside the silica matrix. Figure 5-11(a-c) shows the TEM micrograph of IGSS nanoparticles with increasing number of gold nanoparticles encapsulated inside silica matrix. Corresponding UV-VIS spectra shows increase in absorbance in the NIR region of electromagnetic spectra with the increasing concentration of gold nanoparticles. IGSS nanoparticles are characterized by their broad absorption band in NIR region. The 3D interplasmonic coupling between nearest neighbors gives rise to absorbance in near infrared region. Photothermal efficiency of these nanoparticles is compared with GSS and commercial plasmonic photothermal

Nanoshells (figure 5-12). Concentration of these nanoparticles (GSS, IGSS and Nanoshell) required to increase the temperature of their suspension in water by 15 °C was determined. It is clear from these experiments that (1) photothermal efficiency of IGSS and Nanoshells is comparable, (2) both IGSS and Nanoshells have superior photothermal efficiency than GSS.

Further, NIR fluorescence was integrated into these particles to make them suitable for both imaging and therapy. As described earlier, plasmonic nanocomposites can retain fluorescence if a certain separation distance between fluorophore and plasmonic nanoparticles is maintained. APTS conjugated NIR dye was added in the microemulsion with TEOS during the process of silica coating. The co-condensation of dye molecules with TEOS resulted in the incorporation of NIR dye in the silica shell constructed to encapsulate gold nanoclusters. Figure 5-13 illustrates the fluorescent spectra of IGSS nanoparticles before and after the reduction of FG. The decrease in fluorescence is attributed to the fluorescence quenching by metallic gold formation. Gold nanostructures are known to quench fluorescence of organic dyes as well as inorganic quantum dots. NIR fluorescence imaging and photothermal therapeutic capabilities of these nanoparticles were demonstrated *in vivo* in a tumor bearing mice. *In vivo* photothermal ablation experiments were conducted by intratumoral injection of 20 μ l of 0.3 mg/ml IGSS nanoparticles. Figure 5-14 shows the (a) fluorescence and (b) bioluminescence images of mice before and after the photothermal ablation. Extent of decrease in bioluminescence signal after laser ablation indicates the efficacy of photothermal treatment. Photothermal property of these nanoparticles was compared with commercially used nanoshell under similar weight concentrations. For comparing

the photothermal efficiency of the two particles, changes in bioluminescence signal was compared before and after ablation (figure 5-15). In case of IGSS nanoparticles, a decrease of up to 95% was observed while for nanoshell it was approx 50%. The greater decrease in bioluminescence signal for IGSS nanoparticles could be because of (1) higher number of particles due to smaller size (2) different heat transfer mechanism due to silica coating on gold surface and (3) higher heating surface area.

5.5 Summary

In summary, although photothermal ablation has been pursued for a long time, numerous engineering obstacles need to be addressed before image guided treatment of cancer can be realized. In this chapter, the development and functional evaluation of sub 50nm near IR absorbing and luminescent GSS and IGSS nanoparticles amenable for *in vitro* / *in vivo* tracking and photothermal ablation was described. Prepared in one pot, using microemulsion-mediated method, gold is generated and deposited in situ on or inside fluorescently doped silica nanoparticles as 1-5 nm, irregular shaped, randomly present nanodomains. The 2D and 3D plasmonic coupling between nearest neighbor gold deposit are hypothesized to lead to the broad NIR absorption characteristic of the GSS/IGSS nanoparticles and also inhibits complete quenching of the fluorescent of the dye. Being spherical in shape and devoid of any aspect ratio they are independent of any orientation related performance and because of their small size they are easily expected to extravasate to tumor sites *in vivo*. The incorporation of a fluorescent agent within the silica core of these particles enables them to be readily imaged and applicable for use in high throughput *in vitro* fluorescence assays, *ex vivo* fluorescent histopathological analysis and *in vivo* particles tracking/monitoring. Composed of biocompatible materials, the GSS nanoparticles provide both silica and gold surface

enabling well established bio-conjugation strategies. GSS nanoparticles thus have the potential to become theranostic agent for cancer.

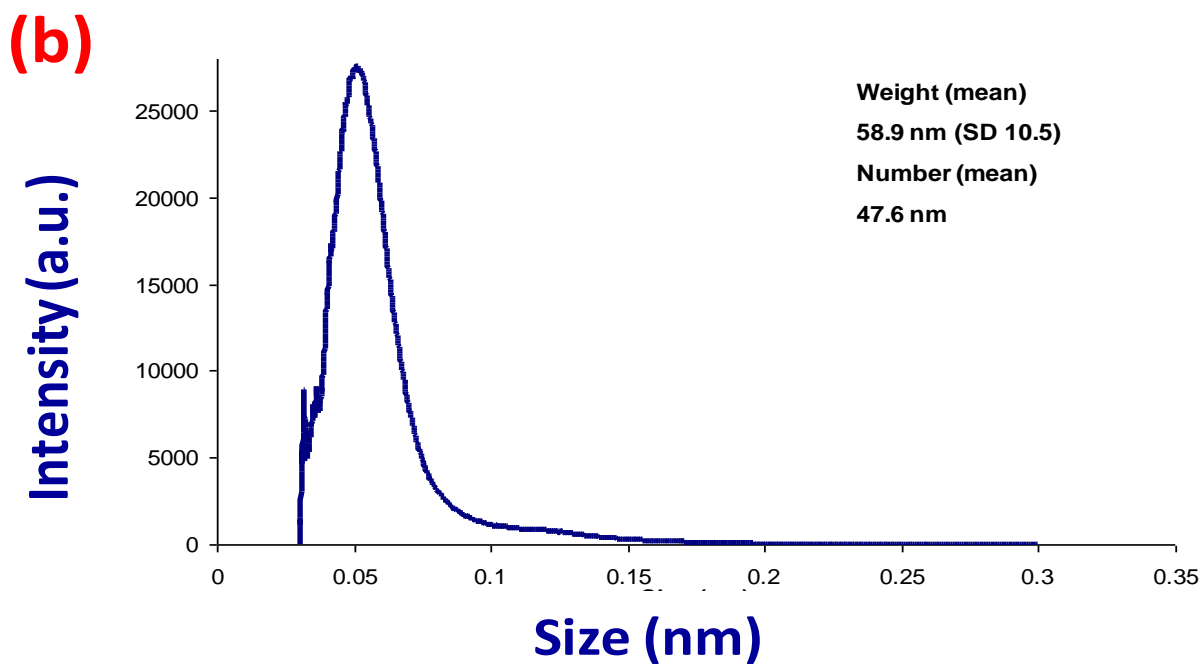
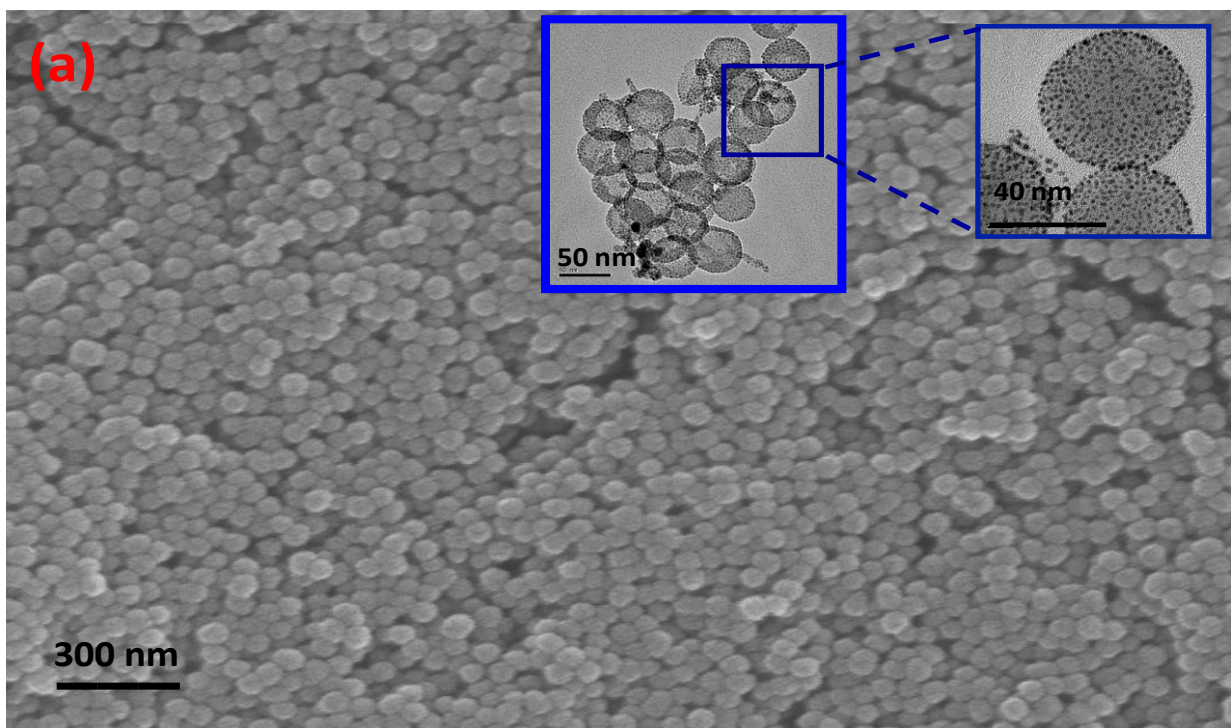


Figure 5-1. (a) SEM image of GSS nanoparticles (Inset in this image show transmission electron microscope image at different magnifications) (b) particle size distribution of GSS nanoparticles measured by disc centrifuge method.

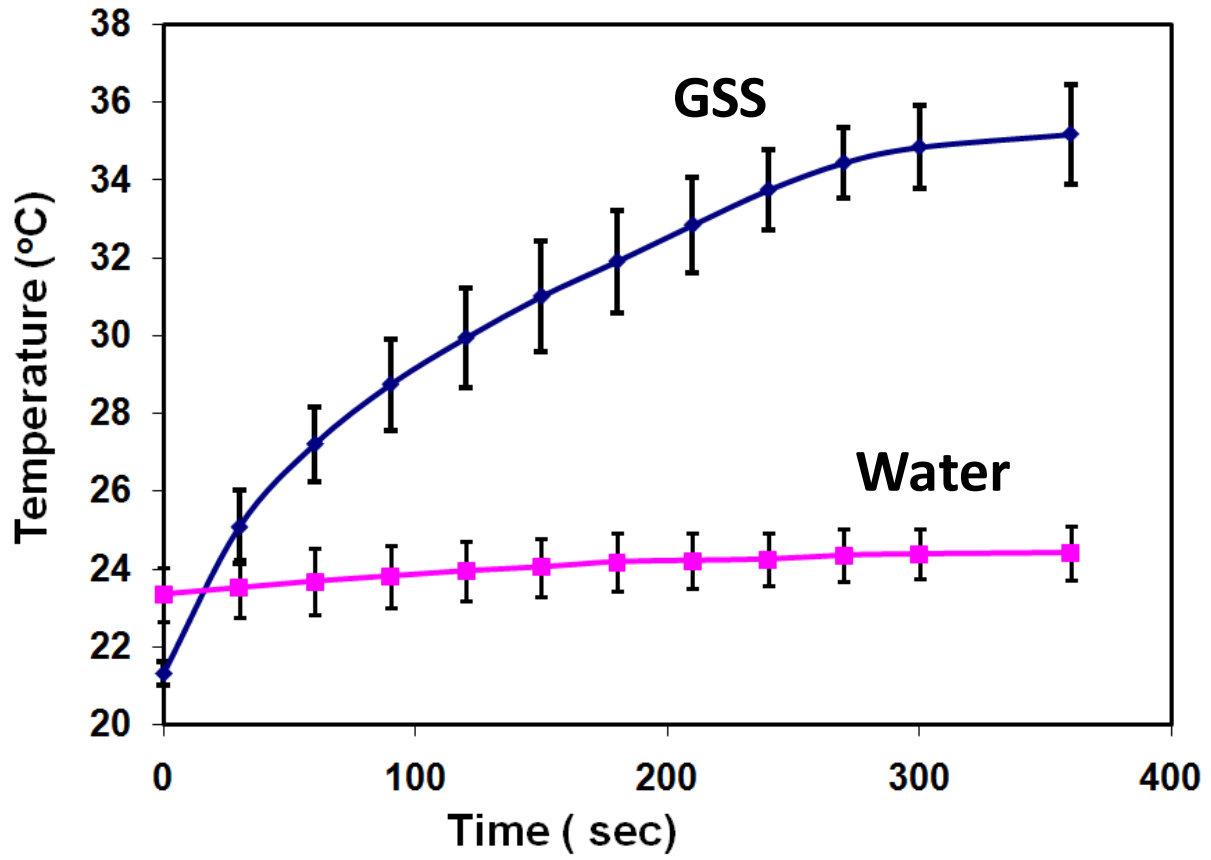


Figure 5-2. Increase in temperature of pegylated GSS nanoparticles suspension in water upon exposure to 500 mW/cm² laser exposure (at 785 nm wavelength).

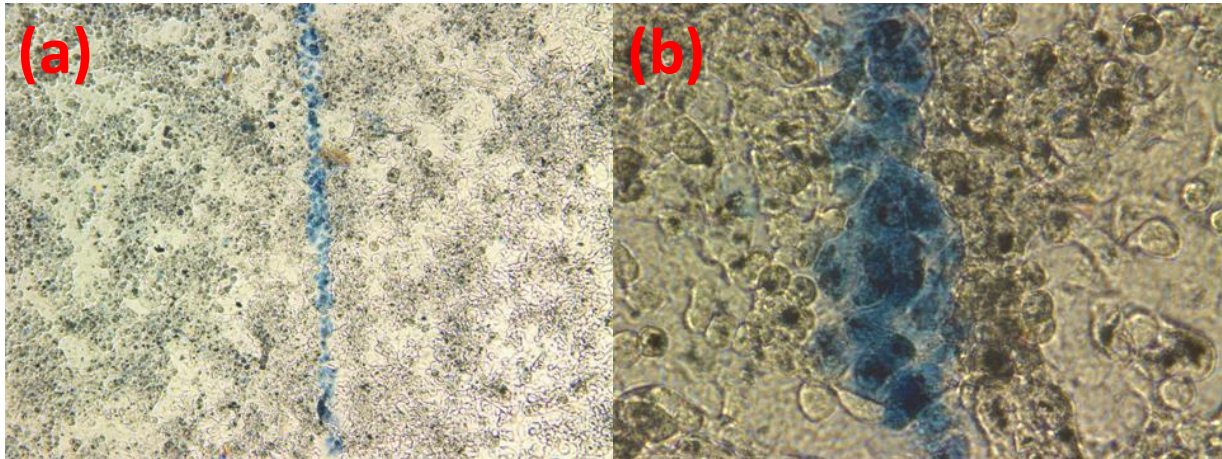


Figure 5-3. (a) Tryphan blue stained dead cells as ablated selectively along the path of NIR laser and unharmed surrounding cells (b) higher magnification image of tryphan blue stained dead cells.

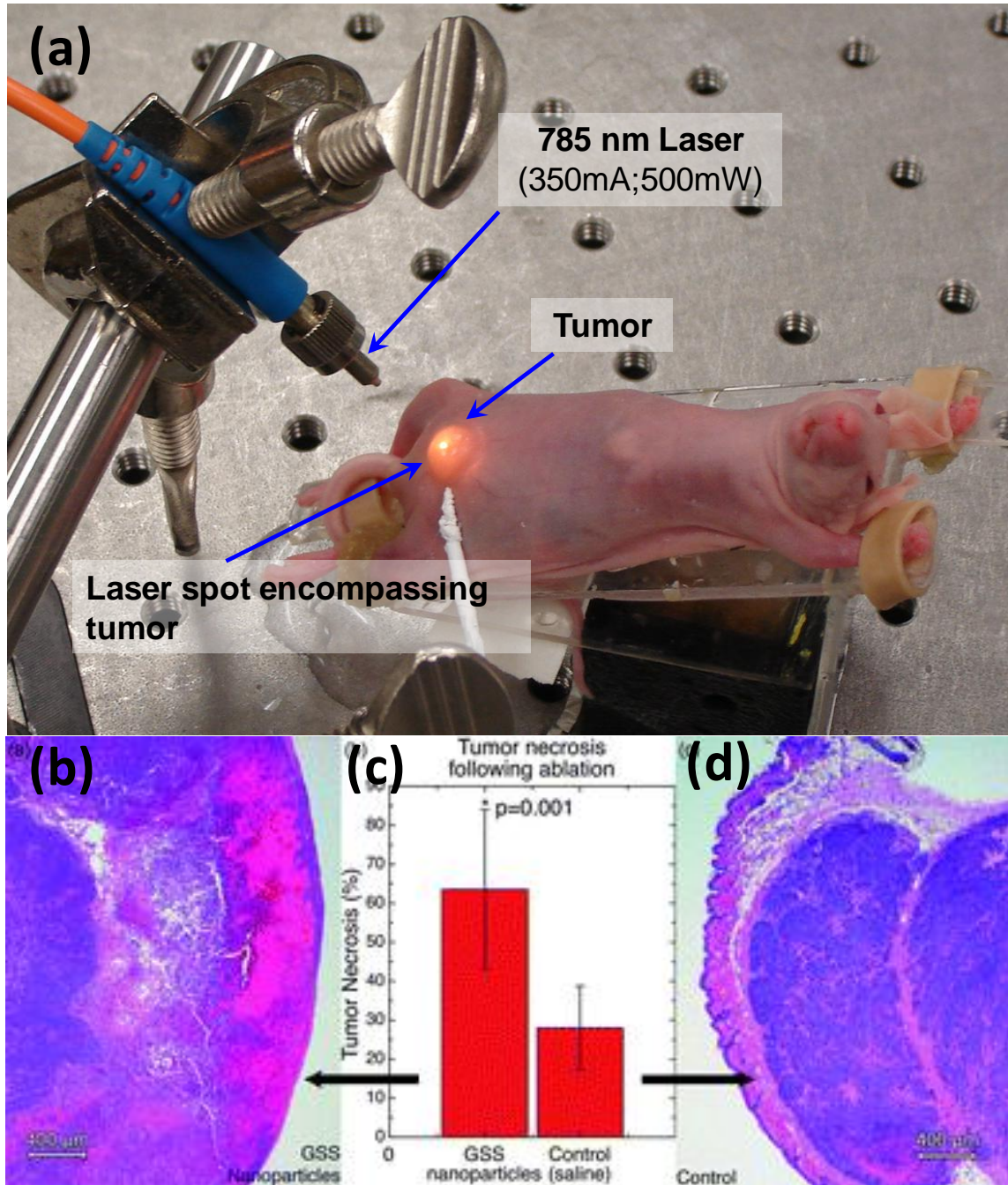


Figure 5-4. (a) Typical experimental setup used for the photothermal ablation of tumor using GSS nanoparticles. Representative H & E stained histological image of ex vivo tumor sections of photo-thermally ablated tumors injected with: (b) GSS nanoparticles, (d) saline injection; (c) significantly more necrosis is observed in tumors treated with GSS compared to control (n = 5).

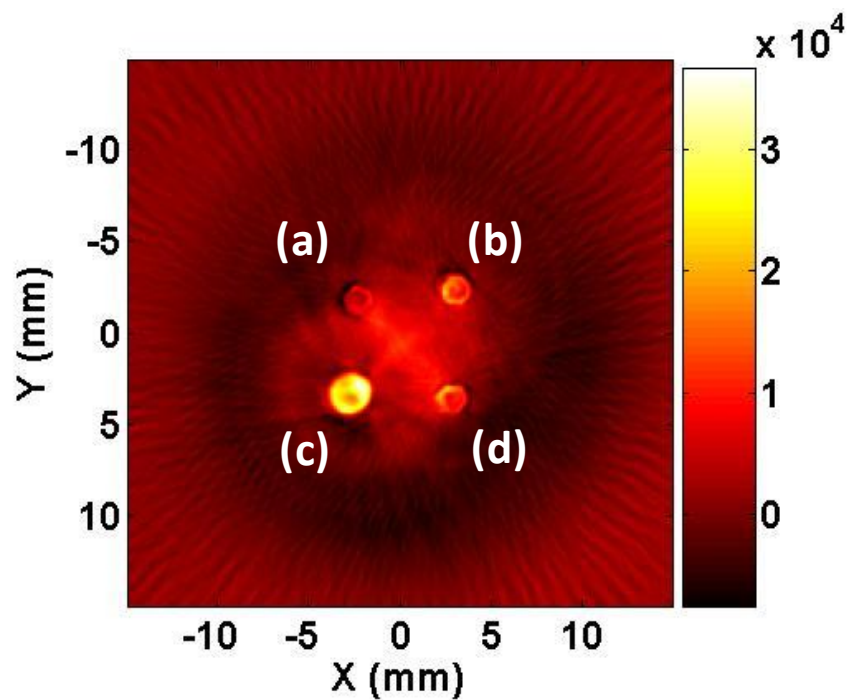
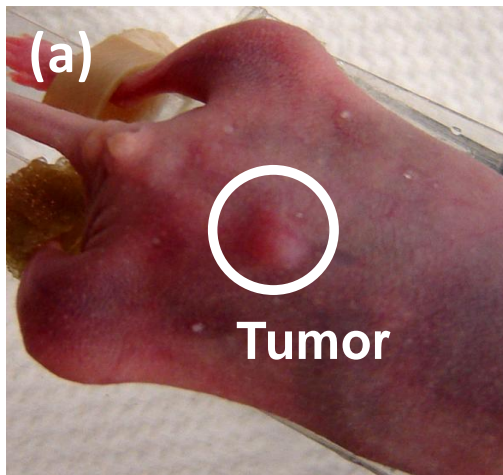


Figure 5-5. (a) Photoacoustic images of GSS nanoparticles in tissue like phantom at increasing concentration (a) 2 mg/ml, (b) 5 mg/ml, and (c) 10 mg/ml. (d) Indocyanine green dye at 5 times higher molar concentration than (c).

Tumor model



PAT Image

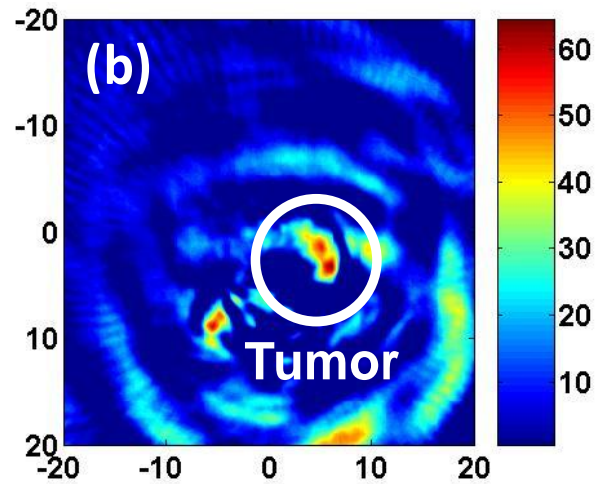


Figure 5-6. (a) Mouse with abdominal tumor (circled) that was used in photoacoustic imaging experiments, (b) photoacoustic image of mouse tumor, imaged 5h after tail vein injection. The location of tumor is circled to guide the eye.

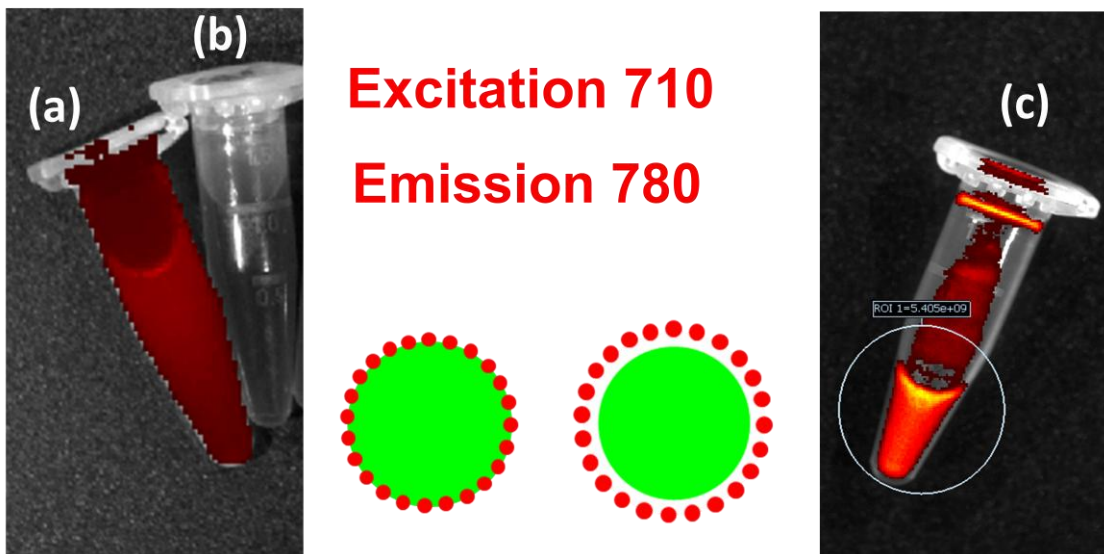


Figure 5-7. Fluorescence images of (a) NIR dye doped silica nanoparticles (fluorescent), (b) NIR dye doped silica nanoparticles after coating with gold specks (fluorescence quenching), and (c) NIR dye doped core with spacer silica shell and then coated with gold specks (fluorescent).

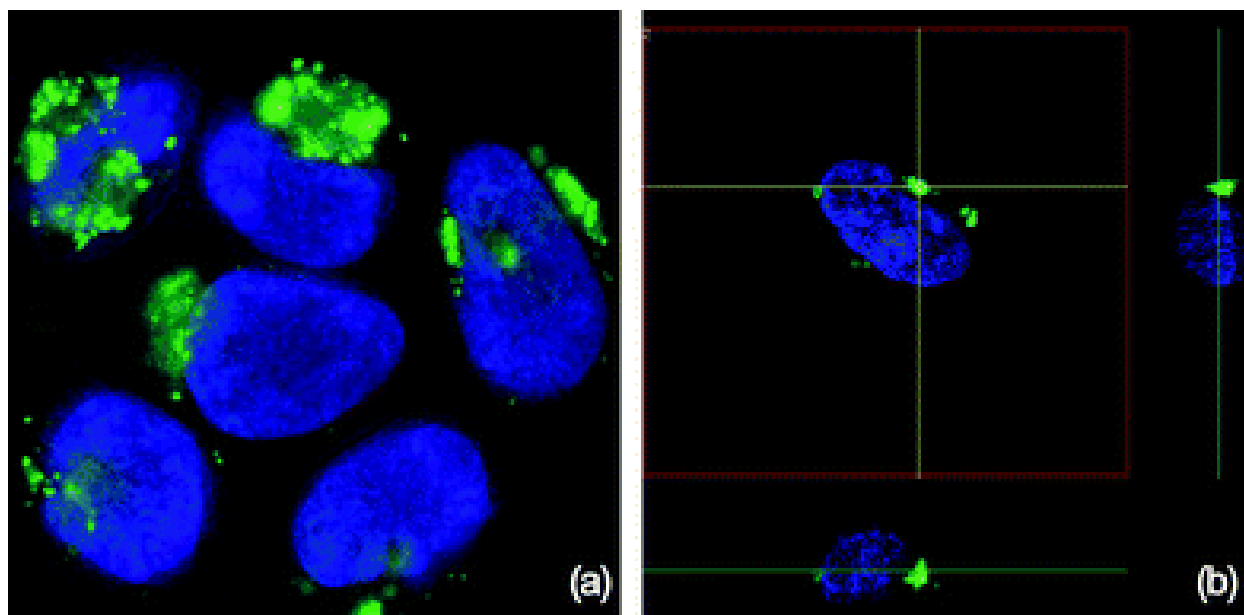


Figure 5-8. (a) Representative confocal microscope picture of lung A549 cells labeled with the FITC doped GSS nanoparticles showing the presence of nanoparticles (green) near the nucleus (blue—stained with Hoechst). (b) A z-position cross section showing the localization of GSS nanoparticles adjacent to the nuclear boundary.

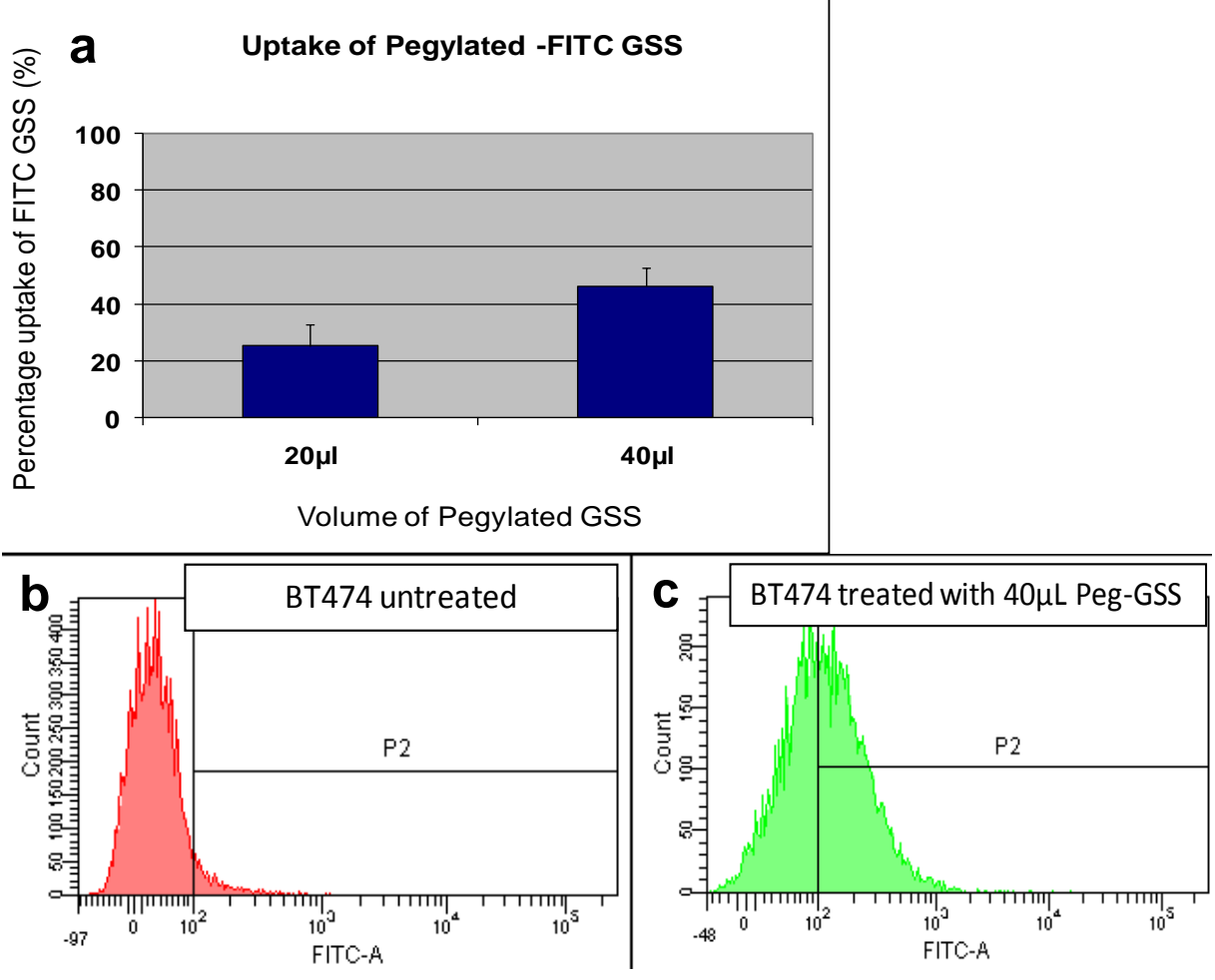


Figure 5-9. (a) Shows the increase in uptake of Pegylated GSS nanoparticles by breast cancer BT474 cells at two different doses (20 and 40 µL of 1 mg/mL); (b) and (c) show the representative FACS spectra of BT474 cells untreated and treated with FITC -GSS.

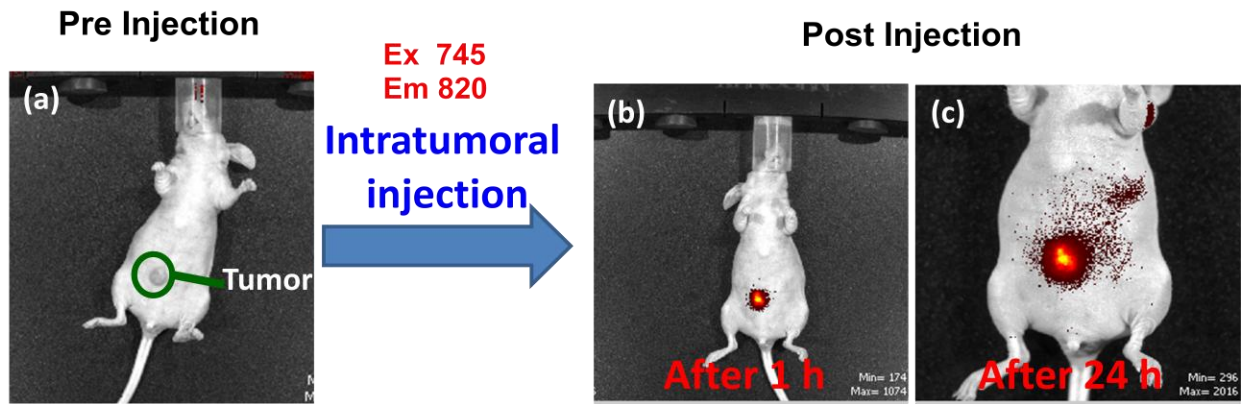


Figure 5-10. Fluorescence imaging of mouse tumor after intratumoral injection of 30 μ l NIR GSS nanoparticles (a) before injection (b) 1 h after injection (c) 24 h after injection. In image (c) particles movement from tumor to lymph nodes can be seen.

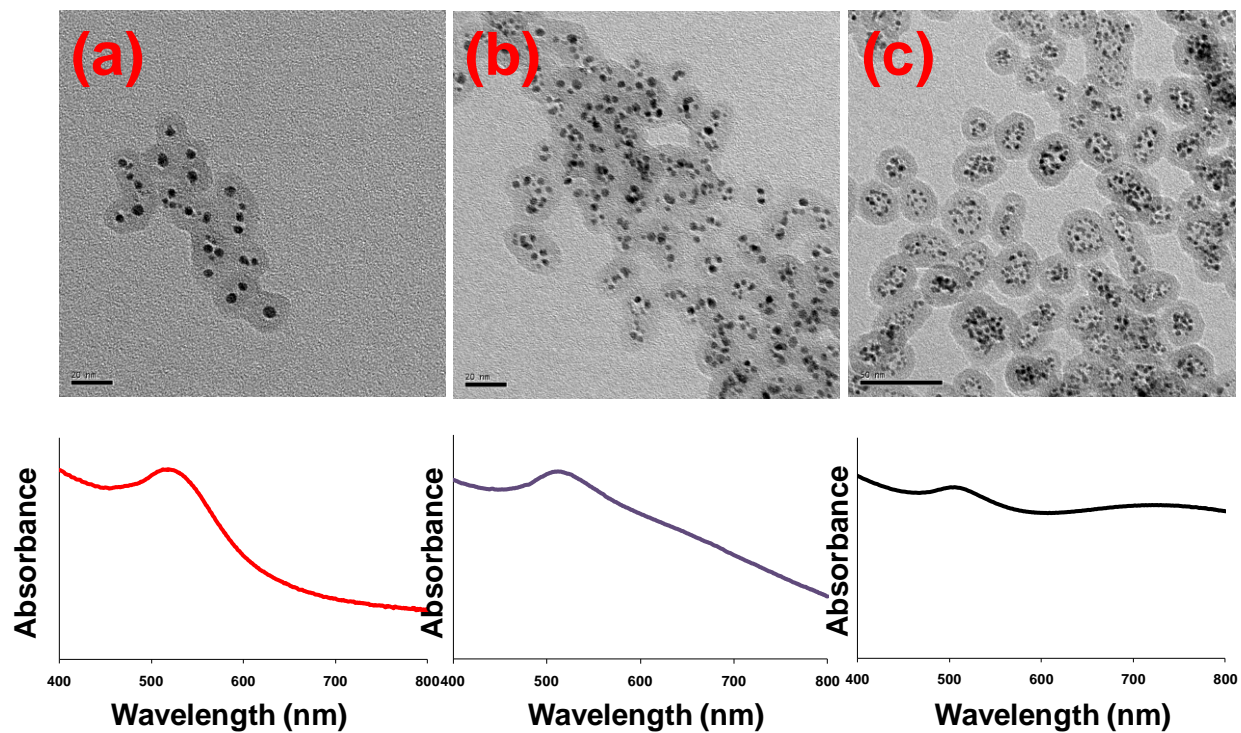


Figure 5-11. TEM images of IGSS nanoparticles synthesized using (a) 50 μl (b) 100 μl and (c) 150 μl volume of 0.5M gold chloride solution. The corresponding absorbance spectra are shown below respective images. In image (a) and (b) bar represents 20 nm, in image (c) bar represents 50 nm.

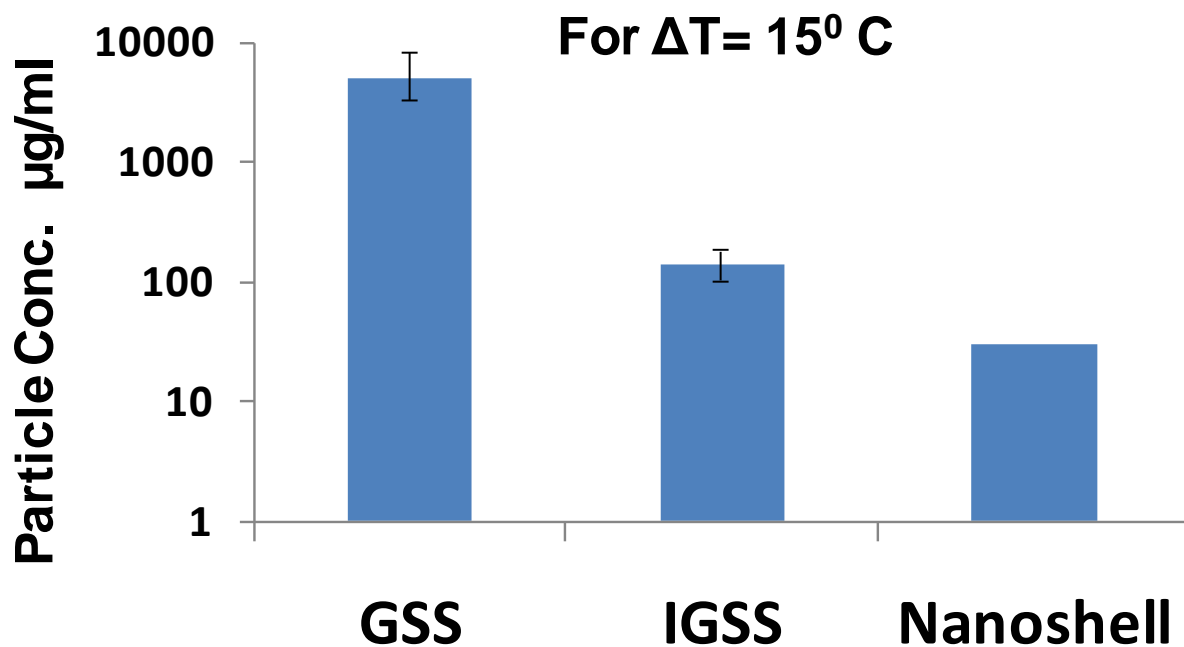


Figure 5-12. Particle concentration required to increase the temperature of 1 ml suspension by 15 °C upon laser irradiation (500 mW/cm²) for 5 minutes.

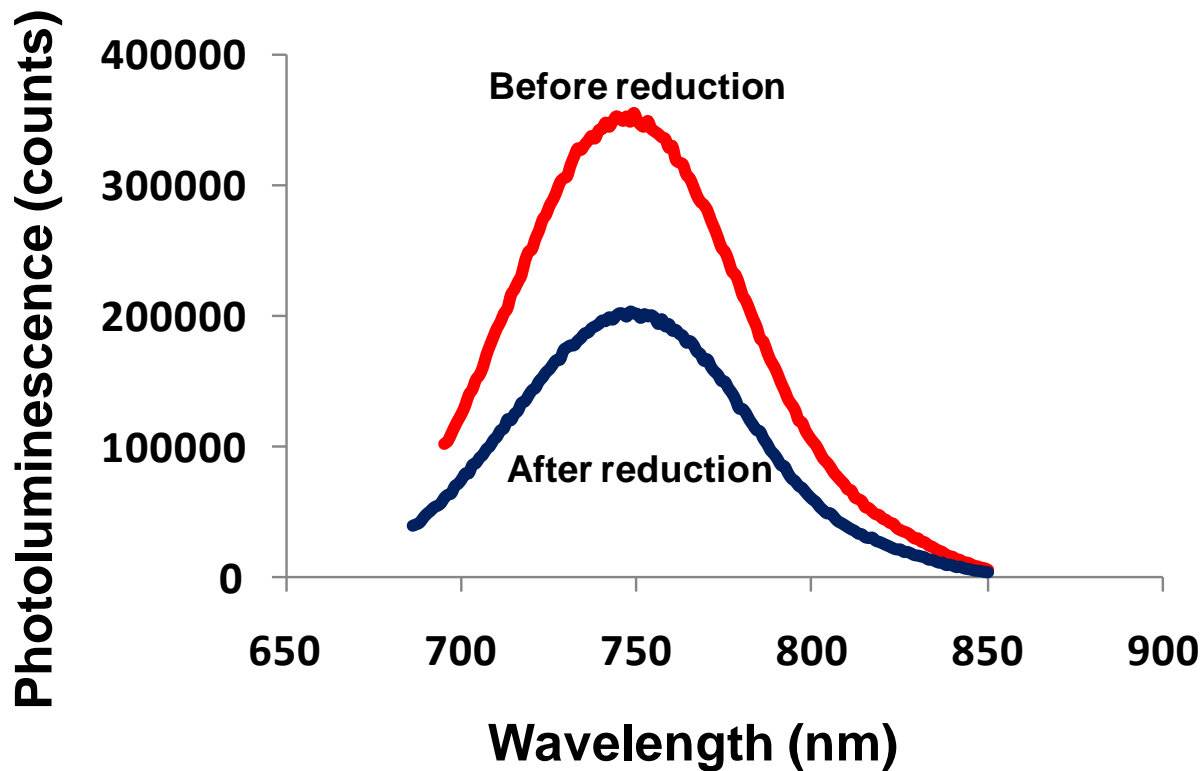
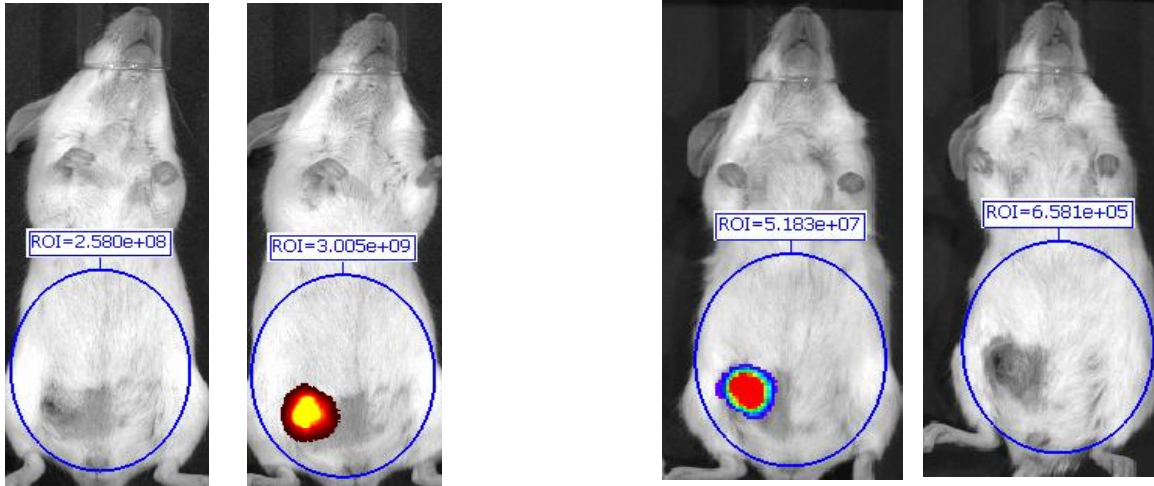


Figure 5-13. Fluorescence spectra showing decrease in fluorescence of luminescent IGSS nanoparticles after reduction of fulminating gold to metallic gold.



(a) Fluorescence Imaging

(b) Bioluminescence Imaging

Figure 5-14. In a typical photothermal ablation experiment (a) Fluorescence imaging before (left mouse) and after (right mouse) injection of luminescent IGSS nanoparticles (b) bioluminescence imaging before (left mouse) and after (right mouse) photothermal ablation experiment.

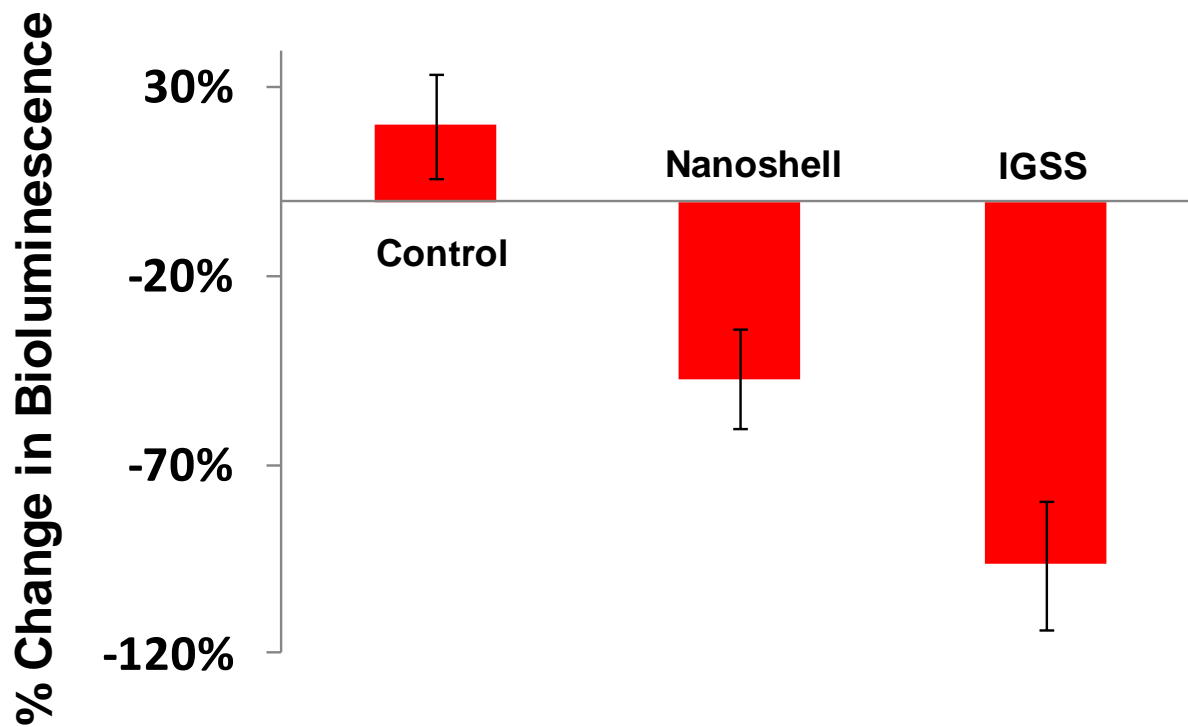


Figure 5-15. Quantification of bioluminescence signal. Y-axis represents % change in bioluminescence before and after photothermal ablation experiment for different particles.

CHAPTER 6 NON-PLASMONIC PHOTOTHERMAL AND LUMINESCENT NANOPARTICLES

Although size independent nanoparticles designed in this work could potentially enhance the tumor accumulation and targeting efficiency, their distribution inside the complex tumor architecture remain uncertain^{118,119}. In all likelihood the distribution of targeted nanoparticles would be highly inhomogeneous and perhaps in aggregated state. Also, the hydrophilic nature of particles restricts their use for intracellular applications due to their inability to move across the cell membrane. The low targeting efficiency of nanomaterials, limited mobility inside tumor due to their relatively large size (compared to molecular probes) and hydrophilic nature could limit their otherwise well established therapeutic potential.

These limitations associated with plasmonic materials provided the impetus to explore alternative strategies for biological applications requiring efficient delivery of therapeutic agents at the site of interest. Ideally, therapeutic agents should be dispersed in such a way that their effect can be experienced homogeneously by all the cells present in the tumor. In other words, molecular level hydrophobic therapeutic agents are more suitable for the effective delivery of therapeutic agents inside a complex structure such as that of tumor¹²⁰. However, hydrophobic molecules are difficult to administer to the site of interest through the intravenous route. Moreover, molecular therapeutic agents lack the advantages associated with nanoparticles such as their ability to enhance intracellular concentration of therapeutic agents, multiple therapeutic agent carrying capability, and their multifunctional aptitude as described in chapter 1.

In order to achieve these seemingly conflicting properties in a single therapeutic probe, “Trojan horse” approach, generally employed for the delivery of bioactive

molecules, was adopted¹²¹. For the realization of this approach, design of smart nanoparticles was conceptualized that have the advantages of both nanoparticles and molecular agents. Nanoparticle can be used as a carrier vehicle for the delivery of molecular photothermal agents at the site of interest. Upon reaching the desired site such as tumor, the release of molecular therapeutic agents could be triggered in such a way that at least entire tumor region is covered by them. Conventional plasmonic nanomaterials and size/shape independent nanomaterials developed in this work are not suitable for this purpose due to their inability to act like a carrier vehicle for molecular therapeutic agents.

In this chapter, we describe a simple approach for the design of non-plasmonic, size independent and optically tunable NIRF-photothermal materials. Hybrid materials based on co-operation of organic-inorganic structures such as mesoporous silica nanoparticles were employed for this purpose. The development of these nanomaterials from the molecular level components makes them ideal for size and shape tunability. Covalent incorporation of NIR fluorescent organic dyes in the silica matrix of mesoporous particles was achieved as described in chapter 2 and chapter 3. The presence of regular pore structure of these materials makes them suitable for the incorporation of multiple therapeutic agents. For example, in this work organic photothermal sensitizers were incorporated in the pores of these nanoparticles. Application of these nanomaterials, doped with multiple dyes, for image guided therapy is presented in this chapter.

6.1 Non-Plasmonic Photothermal and Luminescent Materials

Mesoporous materials are particularly an attractive class of inorganic materials that can be employed as a mechanically robust scaffold for the synthesis of hybrid

materials^{122,123}. Recent advancements in modifying the internal as well as external surfaces of mesoporous silica nanoparticles have made these materials lucrative for biological and biomedical applications^{68,124-126}. These materials have extensively been used for both systematic delivery systems and implantable local delivery devices^{125,127}. Currently these nanoparticles have been used for many other biological applications such as contrast agents for bioimaging (fluorescence, MRI)¹²⁸, biosensors, and gene transfection^{127,129,130}. In this work we have incorporated multiple dyes both within the silica framework during the synthesis and inside the pores of mesoporous silica nanoparticles post synthesis. A silica matrix is preferred due to its biocompatibility, optical transparency, and water dispersibility. Further, the surface of silica nanoparticles can be easily modified using well established surface modification techniques.

6.1.1 Incorporation of Optical Imaging Modality

As described in chapter 3, modified heptamethine cyanine dyes (IR780) were covalently incorporated inside the mesoporous silica framework during synthesis. The photoluminescence of these particles was maximized by optimizing the amount of dye present inside the silica matrix. Increasing the amount of dye, inside the silica matrix, results in lower fluorescence quantum yields; however, their absorption cross section or molar absorptivity increases. A normalized absorbance and emission spectra of mesoporous nanoparticles is presented in figure 6-1. The overall size of nanoparticles as measured by SEM and TEM images was 105 ± 18 nm (figure 6-2(a-b)). Particles synthesized by this method have high surface area (850 ± 62 m²/gm) due to their porous structure also indicated by their TEM images (figure 6-2(b)). This porous structure was used to incorporate therapeutic modality in these nanoparticles as described in the next section.

6.1.2 Incorporation of Therapeutic Modality

In order to impart photothermal properties to these nanoparticles, an organic photothermal sensitizer was incorporated in the pores of mesoporous NIRF nanoparticles. The ideal candidate for this purpose should have low fluorescence quantum yield and low photochemical reactivity in order for it to have good photothermal properties. After photoexcitation, these molecular absorbers can increase the local temperature high enough to cause irreversible photothermal damage to the surrounding cells. Naphthalocyanine dyes are particularly suitable for this purpose as they have intense absorption band ($\epsilon = \sim 10^4\text{-}10^5 \text{ M}^{-1}\text{cm}^{-1}$) in the near infra red region, are non-fluorescent (quantum yield < 0.05), and lack appreciable photochemical activity. Many naphthalocyanine dyes are reported non-linear optical materials that undergo triplet-state adsorption at high laser fluencies. This aspect makes these materials promising for maximizing both photoluminescence at low light fluencies (due to reduced adsorption from naphthalocyanine dyes) and enhanced light absorption induced effect at higher laser fluencies. Several naphthalocyanine dyes are known to generate free radicals in conjunction with the photothermal effect. These materials are considered to be third-generation photodynamic agents and are actively being pursued for clinical applications. The hydrophobic nature of many of these dyes makes them ideal for their encapsulation inside the pores of silica NPs

Although, these dyes are chemically stable, when in the free form they tend to degrade upon exposure to high intensity continuous laser irradiation such as used in photothermal ablation therapies (Table 6-1). Upon 2 min exposure to laser light, all metallonaphthalocyanine dyes (Si, Zn, Mn, Fe) irreversibly changed their solution color from green to yellow in chloroform indicating either degradation of dye or formation of

aggregates. The hydrophobic aromatic nature of many naphthalocyanine dyes leads to the formation and self-assembly of aggregates of dye molecules in aqueous medium. At high concentrations this often results in the formation of structures up to several microns in size that are less effective in absorption of light. As with the heptamethine cyanine dyes, incorporation of naphthalocyanine materials in a silica nanostructure was anticipated to provide the desired localized optical absorption properties for photothermal/photodynamic effects without the complications that are often experienced with free dye materials.

Specifically, a metallo-naphthalocyanine (Si) dye was loaded into the pores of NIR fluorescent mesoporous silica nanoparticles by exposing these nanoparticles to a concentrated solution of dye. These materials due to the presence of multiple dyes are referred to as multidye theranostic (MDT) nanomaterials. Incorporation of dye is confirmed by the presence of a broad peak in the NIR region of electromagnetic spectrum. Once encapsulated inside the particles, the photostability of dye molecules increases drastically. Even after 5 min of 500 mW/cm^2 laser light exposure, a maximum of $5(\pm 1)\%$ change was observed in the optical density of nanoparticles. With an increasing amount of Si-naphthalocyanine dye, the absorbance of the NPs increases but the fluorescence intensity decreases: since emitted photons from the NIR fluorescent dye get absorbed by Si-naphthalocyanine dye molecules.

The photothermal property of NIRF mesoporous nanoparticles was demonstrated by measuring the increase in temperature of MDT nanoparticle suspension upon irradiation with NIR laser source. The increase in temperature of aqueous suspension of MDT nanoparticles and nanoshells with laser irradiation time is plotted in figure 6-3(a).

After 5 minutes of irradiation time a maximum temperature change of 12 °C (± 2 °C) and 18 °C (± 3 °C) was measured for nanoshells and MDT NPs respectively. Both nanoshells and MDT NPs were used at unit optical density. Upon further increase in irradiation time the suspension temperature did not change significantly (data not shown). The higher temperature increase in case of MDT NPs could be due to their higher surface area compared to nanoshells. There was no significant temperature change observed when nanopure water alone (without MDT NPs) was irradiated with laser source for the same duration of time.

6.1.3 *in vivo* Experiments

For *in vivo* experiments fluorescence and photothermal properties of these particles were optimized (figure 6-3(b)). An optimum amount of naphthalocyanine dye was incorporated in the particles such that the photoluminescence (PL) of particles remained high enough to be detected inside the tumor. For the optimized particles the ratio of fluorescent dye: heating dye was approximately 5:1 as calculated from the extinction spectra of MDT particles.

In vivo application of MDT NPs for image guided therapy was demonstrated in an orthotopic murine mammary tumor model that provides immediate feedback to the photothermal therapeutic efficiency of these nanoparticles. Orthotopic primary tumor implantation was chosen because of its importance for the biologically relevant metastatic model development. After intratumoral injection of MDT-NPs, tumor was irradiated with a low power near-infrared laser source for 5 minutes. The fluorescence and bioluminescence images of tumor bearing mice before and after the photothermal treatment are presented in figure 6-4(a-d). To quantitatively assess the tumor destruction, decrease in bioluminescence signal was calculated. A percentage decrease

of up to 95% was observed in mice that were irradiated with NIR laser after intratumoral injection of particles (figure 6-5). The significant decrease in bioluminescence was caused by photoinduced damage of tumor cells. Control groups demonstrated no effect from irradiation and the NIR-NP/ no ablation group was unaltered by the presence of the MDT NIR-NPs. Histologically, a congruent pattern was observed. Figure 6-6 is a presentation of hematoxylin and eosin stained tumor section of control/+ablations, demonstrating a viable tumor nodule and MDT NPs/+ ablation showing areas of necrosis caused by localized heat generation. For the fluorescence signal a decrease of ~18 % in intensity was observed after laser irradiation (figure 6-7). The decrease in fluorescence signal could be due to partial photobleaching of dye or because of particle redistribution and movement during the tumor ablation experiment. However, even one day after ablation the intensity of fluorescence signal remained ~600% higher than the background signal.

6.2 Summary

In summary we have presented the development of MDT NPs for image guided therapy applications. These hybrid inorganic-organic nanoconstructs were designed by integrating multiple dyes within a single mesoporous nanoconstruct. Firstly, a fluorescent dye was incorporated inside the silica matrix such that the dye molecules remain dispersed and protected to yield maximum photoluminescence. Secondly, a nonfluorescent dye was incorporated in the pores of these particles in order to make them photothermal agents for therapeutic applications. The amount of both dyes was varied in such a way that the resulting particles possessed optimized fluorescent and photothermal properties for *in vivo* applications. The porous structure of these nanoparticles can be used for the incorporation of hydrophobic drug molecules. These

preloaded drug molecules can be delivered at a specific site *in vivo* by using a NIR optical source. Further work is needed to demonstrate the potential of these particles for drug delivery purposes.

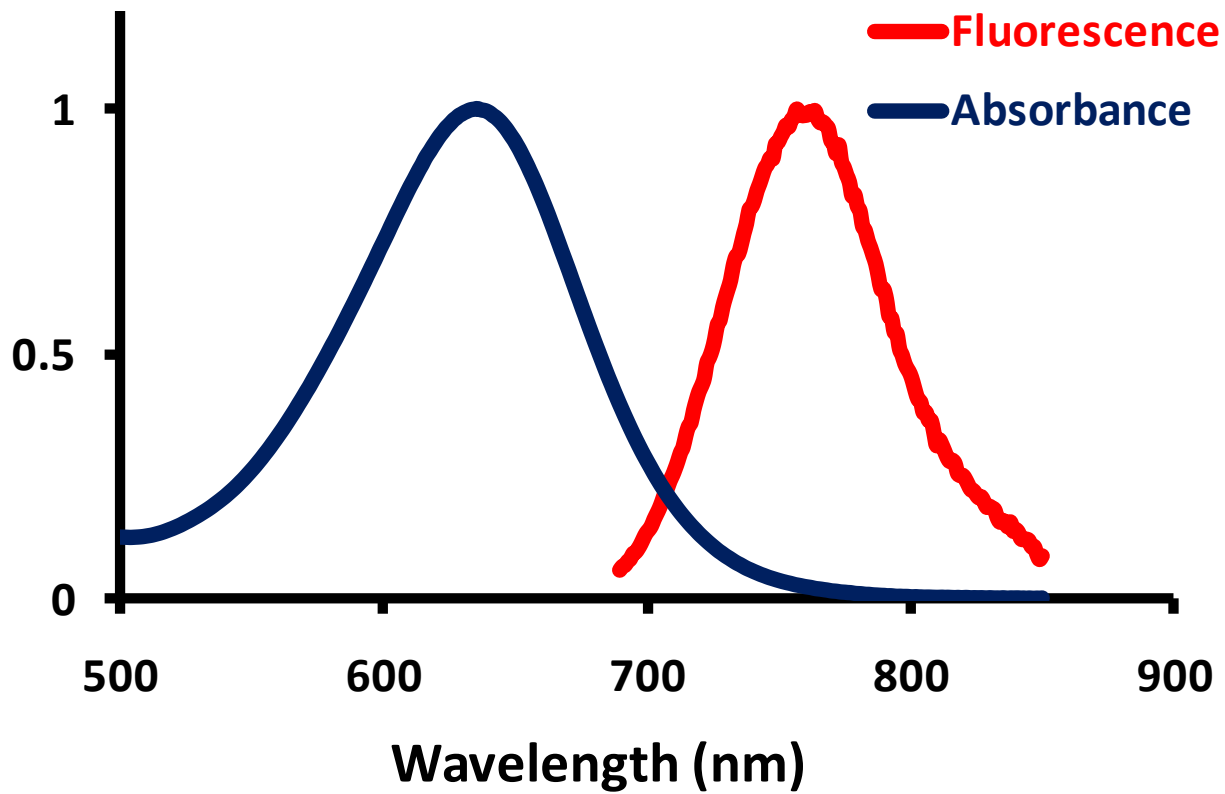


Figure 6-1. Normalized absorbance and fluorescence spectra of NIR fluorescent mesoporous silica nanoparticles. Stokes shift of these particles was ~115 nm.

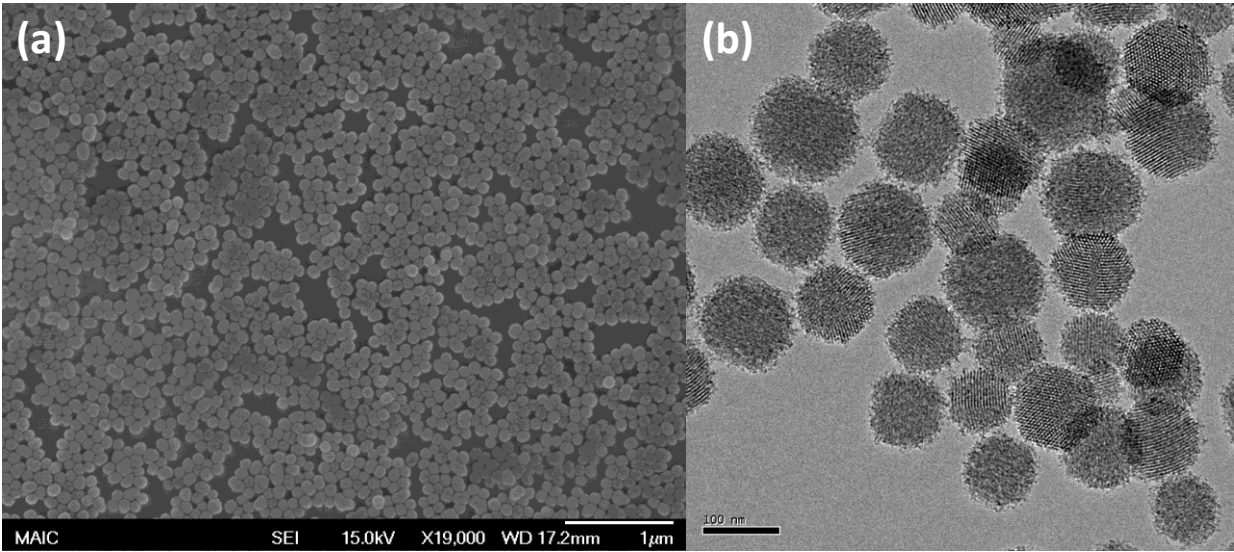


Figure 6-2. (a) Scanning electron microscopy and (b) Transmission electron microscopy images of MDT-NPs.

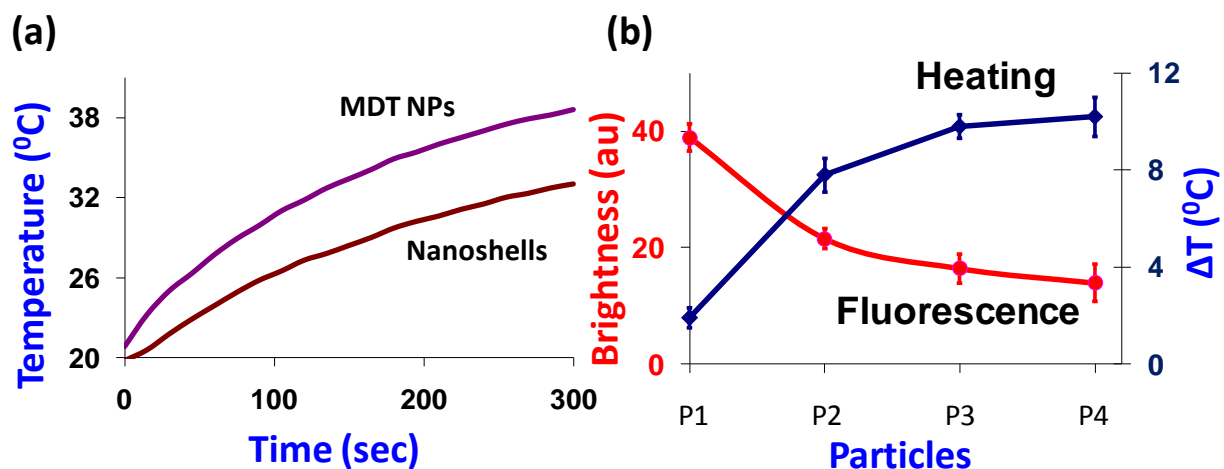


Figure 6-3. (a) Change in temperature of MDT NPs and nanoshells in water suspension when exposed to 500 mW/cm² laser irradiation. The parameters used in the experiment are mentioned in the table below (b) change in fluorescence and heating properties of MDT NPs upon increasing the amount of heating dye encapsulated inside mesoporous silica. Corresponding ratio of heating dye to fluorescence dye is presented in the table below.

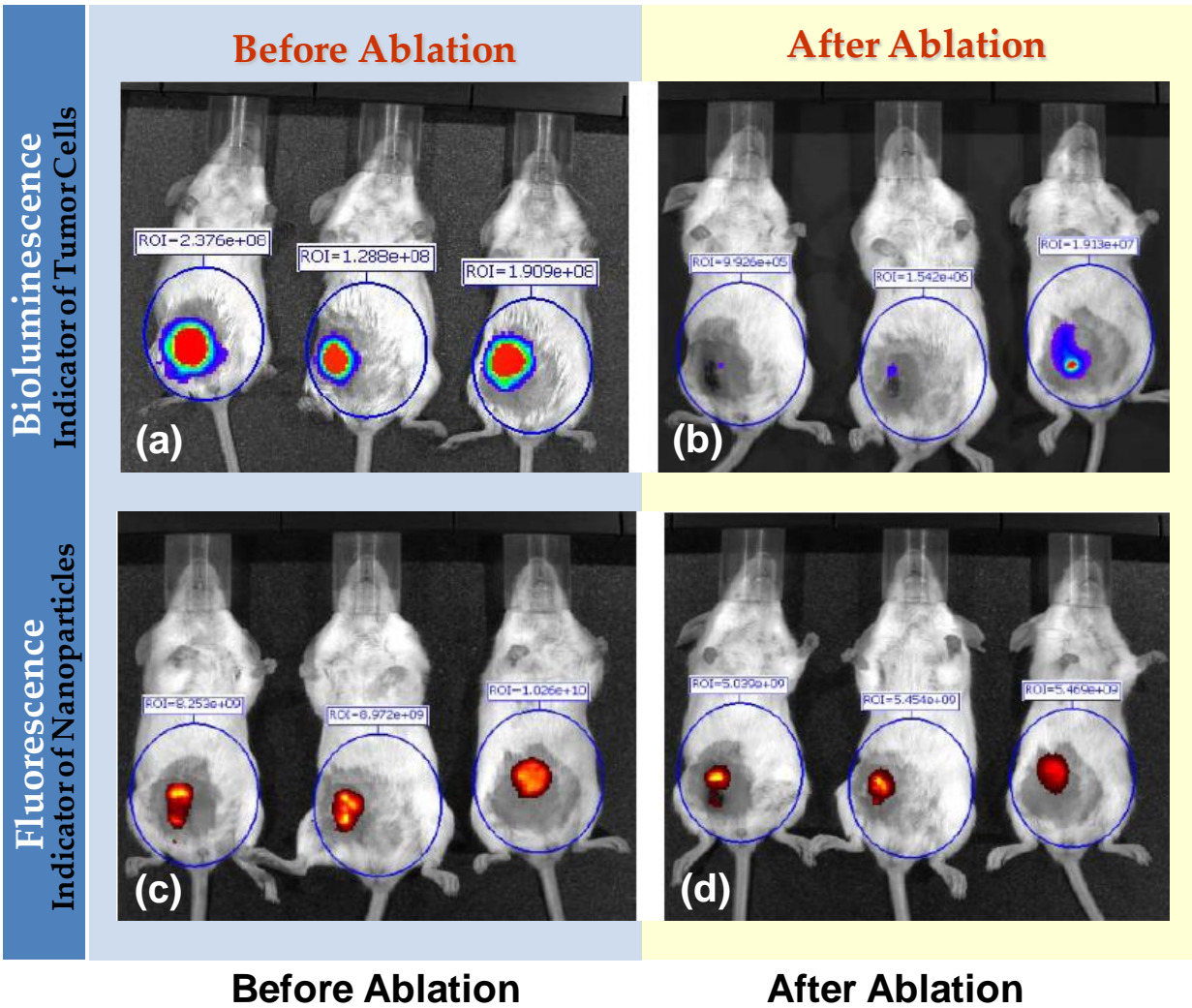


Figure 6-4. Bioluminescence (a,b) and fluorescence images (c,d) of mice before (a,c) and after the photothermal ablation (b,d) using NIR laser.

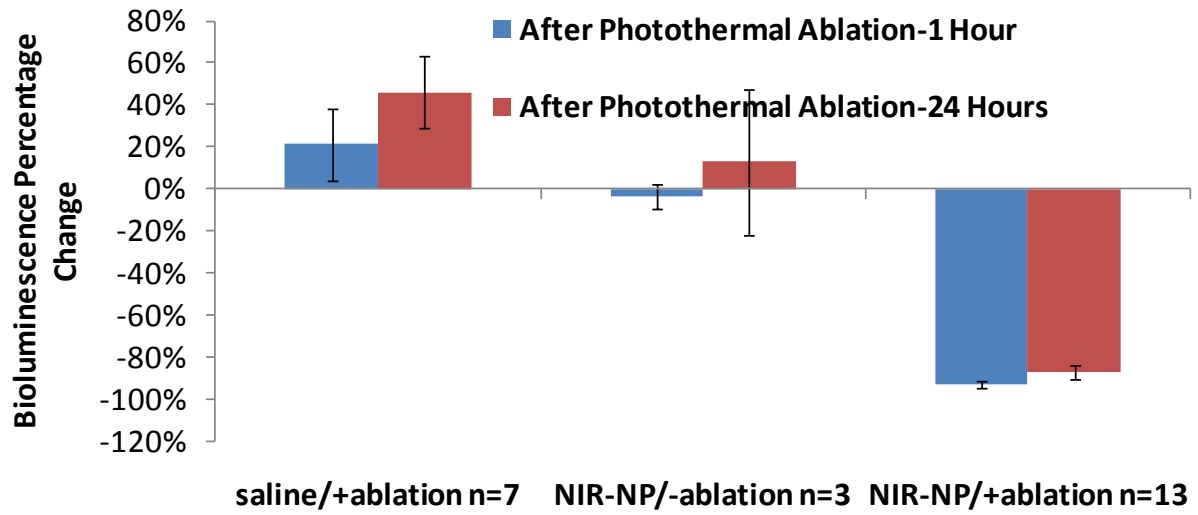


Figure 6-5. Change in bioluminescence signal before and after the tumor ablation measured at different point of time.

Histology: H&E Staining

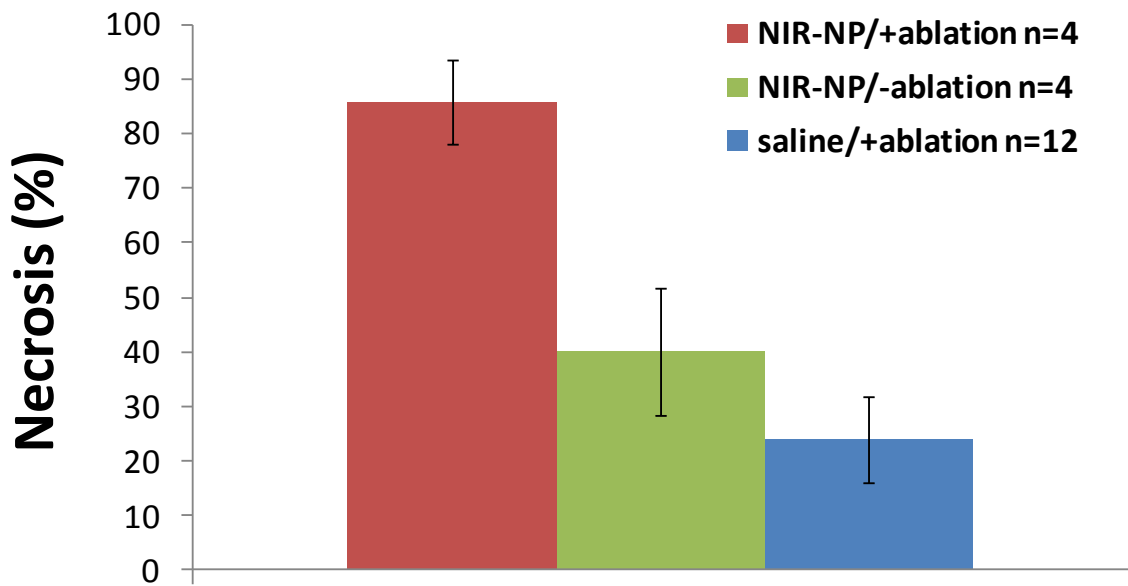
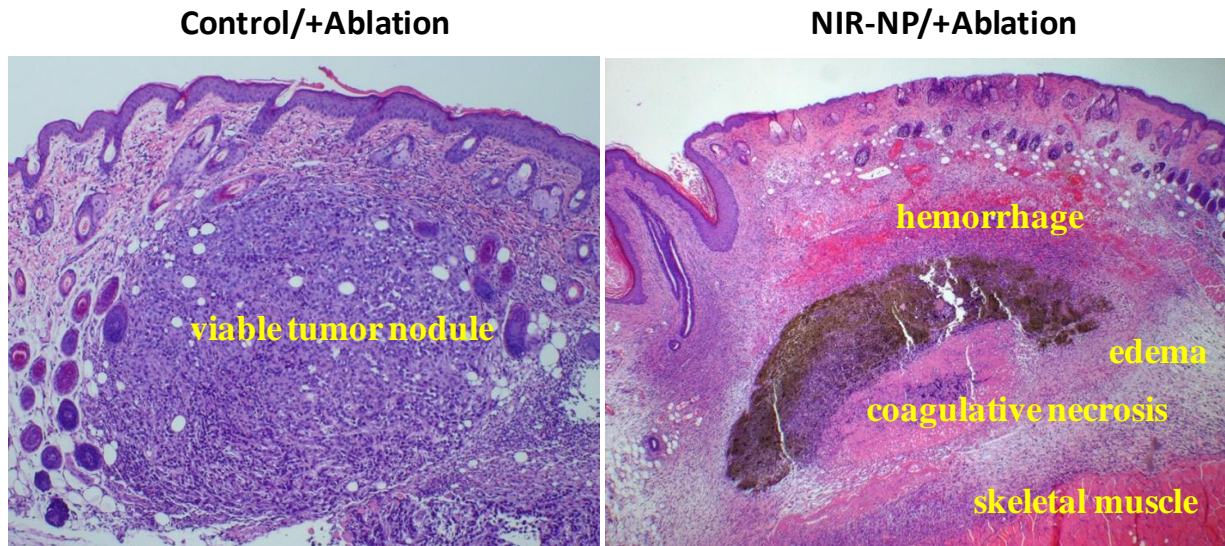


Figure 6-6. Histological sections of tumor (a) Control/+Ablation and (b) MDT-NPs/+Ablation, stained with Hematoxylin and Eosin demonstrate areas of necrosis. (c) histogram showing significantly more necrosis in tumors treated with MDT-NPs.

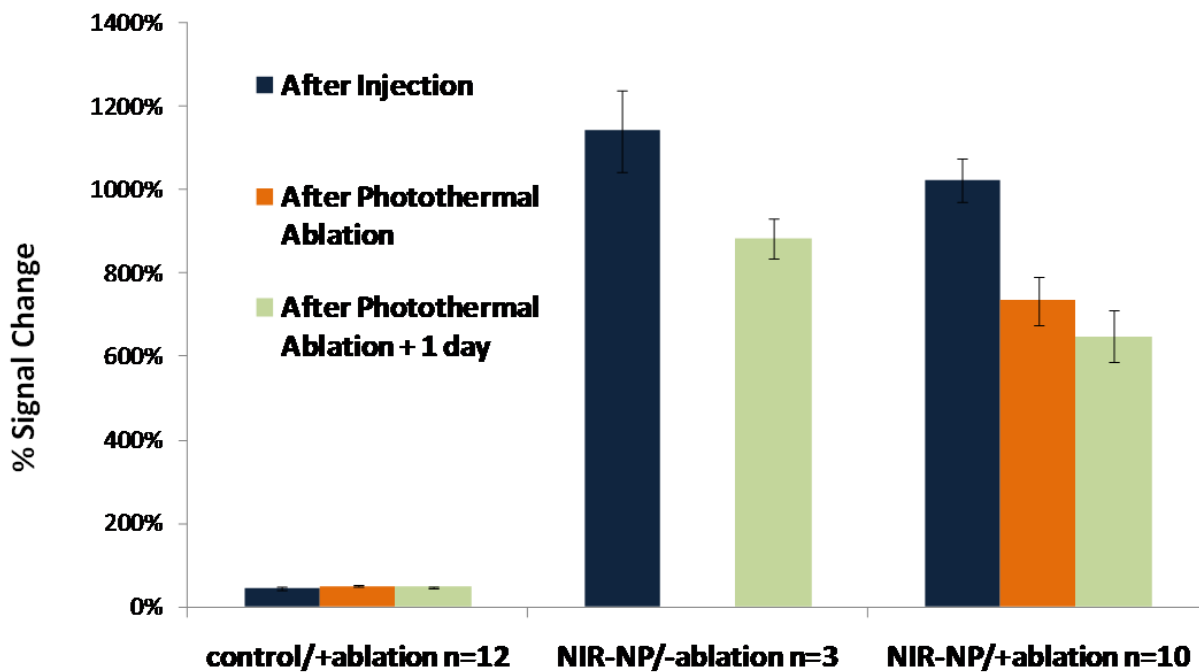


Figure 6-7. Change in fluorescence signal for (a) control/+ablation (b) MDT NPs/-ablation and (c) MDT NPs/+ ablation. Y-axis represents percentage change from background signal that was measured prior to particle injection.

Table 6-1. Effect of laser irradiation on different nahthalocyanine dyes. All dyes were exposed to continuos laser intensity (785 nm, 500 mW/cm²) for 2 min.

Dye	Conc (mg/ml)	Initial OD	Final OD	% Change
Si	0.13	1	0.05 (±0.02)	95
Zn	0.01	1	0.06(±0.02)	94
Fe	0.03	1	0.06(±0.01)	95
Mn	0.08	1	0.05(±0.01)	96

CHAPTER 7 CONCLUSIONS AND FUTURE WORK

7.1 Conclusions

The development of nanoparticulate based imaging contrast agents is anticipated to lead to early detection and localized therapeutic technologies, thereby enhancing treatment efficacy. Of particular importance are near-infrared (NIR) optical nanomaterials as they fulfill the requirement for both, (1) high sensitivity for early stage disease diagnosis (by utilizing radiative fluorescence properties) and (2) localized therapy for treatment of diseases (utilizing their non-radiative photothermal properties). Although, most optical materials possess both of these properties, often materials with superior radiative properties have inferior non-radiative properties. Nanoparticles could potentially offer a common platform to integrate multiple optical materials to achieve the desired imaging and therapeutic properties. However, previous attempts to engineer such nanoparticles were thwarted because of (1) poor chemical/physical photostability of NIR fluorescent dyes, (2) low fluorescence quantum yield, (3) lack of strategies for their incorporation into nanoparticle matrix, and (4) quenching in fluorescence as a result of co-incorporation of photothermal materials. Attempts to prevent quenching resulted in the complication of synthesis protocols. Moreover, the size of overall nanoparticle increased beyond their ability to harvest nanoscale properties such as enhanced size dependent uptake (required size 30-50nm) and renal clearance (required size < 7nm).

The focus of the current research efforts was to synthesize nanoparticles that overcome the limitations associated with previous generations of contrast and therapeutic agents. In the present studies, multifunctional nanoparticles (MNPs) were

strategically engineered through integration of photophysical components such as fluorophores for optical imaging and plasmonic materials for photothermal ablative treatment. Further, these particles were designed in such a way that their size and shape can be tuned according to the requirement in a particular biological application. Several novel design rules/strategies were established for the molecular level design of these MNPs from individual components built from organics, inorganics and metals.

The core of the MNPs was designed by covalently incorporating a fluorescent dye, having NIR excitation and emission properties, into silica NP matrix. Commonly used ICG dye could not be used because of its poor photophysical properties and lack of conjugation ability. Recently developed heptamethine cyanine dyes were selected for this purpose due to their superior photophysical and photochemical properties compared to ICG. These dyes were chemically modified at the meso-chlorine position to enable (1) superior fluorescence properties (QY increased up to ~35% compared to ~4% before modification), (2) further chemical modification for their covalent incorporation into silica nanoparticles, and (3) inherent large Stokes shift (up to 150 nm compared to 20-30 nm before modification), a property required for enhancing the signal to noise ratio in imaging. It was observed that due to the hydrophobic nature of these dyes, they tend to form aggregates in polar environment such as that of silica nanoparticles. Aggregation of dye molecules results in partial or complete loss of their photoluminescence. Following strategies were developed for minimizing the aggregation of dye molecules during their incorporation into silica matrix: (1) by slowing down the growth of silica nanoparticles by addition of dimethylformamide, (2) by dispersing the hydrophobic dye molecules into the core of surfactant (C₁₆TAB) micelles,

and (3) by engineering the microemulsion environment for the synthesis of nanoparticles to employ above two strategies. Microemulsion methods, upon implementation of aforementioned approaches resulted in the formation of brightest particles (photoluminescence increased ~16 times compared to photoluminescence of particles synthesized by slow growth method). Further, dye doped nanoparticles synthesized by microemulsion were ~50 times brighter than the commercially available quantum dots (Invitrogen) when compared by number. It was also established that in microemulsion systems, silica nanoparticles first form at the oil-water interface and then grow towards the center, resolving a long-standing question concerning the growth mechanism in this system. Furthermore, it was established that both quantum yield and molar absorptivity of dye doped nanoparticles need to be considered for maximizing their photoluminescence properties as opposed to focusing on quantum yield alone. The current studies present first report on covalent incorporation of NIR dyes in diverse type of silica nanoparticles matrix (Stöber, mesoporous and microemulsion).

The high sensitivity of NIR NPs, synthesized by microemulsion method, for fluorescence detection was demonstrated by *in vivo* fluorescence imaging at ten time lower concentration than the current gold standard for optical imaging, quantum dots (Invitrogen). Surface modification strategies utilizing biotin-avidin interactions were employed to deliver these nanoparticles to specific sites in tumor endothelium matrix through active targeting. Another unique feature of these particles was their size tunability. Using different methods NIR dye doped silica nanoparticles were synthesized in the size range from 3 nm to 150 nm. In principal, dye molecules can be incorporated

in various nanoparticles independent of their size and shape, making these particles versatile for biological applications.

The next step was to equip these ultra bright NIR fluorescent particles with NIR photothermal properties for the selective destruction of targeted cancer cells using photothermal ablation. A new approach based on interplasmon coupling between gold nanoparticles was developed in order to impart NIR photothermal properties to these nanoparticles. It is well established that upon decreasing the distance between a pair of gold nanoparticles (of the order of their size), their absorbance shifts to the longer wavelengths. In this work, extremely small (1-3 nm) gold nanoparticles were deposited on the surface of dye doped silica nanoparticles. 2D plasmon coupling between nearest neighbor gold nanoparticles was utilized to achieve NIR absorbance properties. A novel microemulsion mediated precipitation-deposition approach was developed to control the size and surface coverage of deposited gold nanoparticles for maximizing their NIR absorbance properties. For 40 nm GSS nanoparticles, maximum NIR absorbance/photothermal properties were accomplished with a surface coverage of ~18% (mean gold nanoparticles size = 3 nm). Further increase in the gold surface coverage, resulted in the destabilization of microemulsion. Luminescent GSS nanoparticles were synthesized on high quantum yield (> 95%) FITC dye doped silica core. Synthesis of GSS nanoparticles on low quantum yield (<40%) NIR heptamethine dye doped silica core resulted in the complete quenching of fluorescence due to the proximity of metal nanoparticles. The separation between dye doped core and gold specks was increased to reduce the quenching of fluorescence by gold nanoparticles. The optimal separation distance was found to be approximately 5 nm. The potential of

these luminescent and NIR absorbing gold speckled silica nanoparticles was demonstrated for image guided therapy of cancer using a human breast cancer model implanted in mice.

While plasmonic materials, developed in this work, have good photothermal properties, they lack the ability to disperse in the entire tumor because of complex architecture of tumor and limitation in targeting efficiency. These limitations could limit their otherwise well established therapeutic potential. In order to overcome this limitation, a different method was employed to impart photothermal properties to NIR fluorescent particles. NIR fluorescent particles were designed to have porous structures in the form of 2-3 nm cylindrical channels. The pores were filled with a hydrophobic dye that has excellent photothermal properties. Upon reaching the tumor site these dye molecules can be released from the pores (by NIR laser irradiation) to cover the surrounding tissue area. Hydrophobic nature and small size of dye molecules enable their transport to intracellular environment as well as intratumoral dispersion. Additionally, the porous structure of these multiple-dye-therapeutic (MDT) nanoparticles can also be utilized to incorporate other functionalities in the particles or drug delivering capability along with multimodal imaging. The imaging and therapeutic capabilities of these nanoparticles were demonstrated *in vivo* and a bioluminescence based model was developed for the semi-quantitative assessment of their photothermal properties. The developed model was compared with conventional assays and in both cases, similar values of %necrosis (>90%) was achieved. Using this model, photothermal efficiency of MDT NPs was also compared with commercial Nanoshells. When both

nanoparticles were used at same weight concentration, the photothermal efficiency of MDT NPs (~94%) was better than that of Nanoshells (~45%).

7.2 Suggestions for Future Work

Although NIR dye doped silica nanoparticles, developed in this study, offer immense potential as contrast agent for *in vivo* biological applications, like other optical contrast agents they suffer from low penetration depth. In addition to improvement in instrumentation, the imaging depth can be increased by further enhancing the fluorescence of these NPs. In an ideal case, for the brightest nanoparticles, the quantum yield of dye molecules should not decrease upon their encapsulation. The decrease in QY is attributed to the aggregation of dye molecules. Hence, the QY/photoluminescence of the particles can be enhanced by using spacer molecules between the dye molecules. For example, co-incorporation of glycerol molecules with heptamethine dyes into silica matrix is expected to enhance the photoluminescence of dye doped nanoparticles. Dye molecules have good dispersion in glycerol as indicated by their high quantum yield (up to 40%) when glycerol was chosen as a solvent. Preliminary experiments performed using co-encapsulation of glycerol and NIR dyes in Stöber silica method showed promising results (4 fold increase in QY). Another issue that needs further investigation is the decrease in fluorescence of heptamethine cyanine dyes in presence of ammonia (catalyst used for the synthesis of silica nanoparticles). A possible route for this study is to investigate chemical changes in the structure of dyes upon addition of ammonia by employing carbon and proton NMR (nuclear magnetic resonance).

In the current studies, it was observed that deposition of gold nanoparticles on dye doped silica core resulted in quenching of fluorescence. However, gold nanoparticles

can also be used to enhance the fluorescence of dye molecules. Even after several years of intense research, the effect of plasmonic materials on fluorophores needs further investigations in order to enhance the fluorescence of dye molecules. GSS nanoparticles could be an attractive system to systematically study the quenching/enhancement of fluorescence as in this system the distance between fluorescent core and gold nanoparticles can be controlled precisely. Further, the novel method, for gold nanoparticles synthesis, developed in the present studies could have several biological as well as non-biological applications. For instance, gold speckled silica (GSS) nanoparticles offer an ideal platform for studying the size dependent catalytic behavior of gold nanoparticles. Gold nanoparticles possess catalytic properties, only when their size is less than 5 nm. As described in chapter 4, the size of gold nanodomains (in sub 5 nm size range) can be controlled in GSS nanoparticles by varying the molarity of gold chloride solution.

Large scale production of novel gold and gold composite nanostructures using fulminating gold (FG) as a mediator is currently being pursued by our research group for biological applications such as NIR photothermal ablation. The application of FG for the synthesis of high concentration colloidal gold nanoparticles is another potential research area. Gold nanoparticles are known to form aggregates due to their high surface energy and often are used in dilute suspensions (typical concentration = 50 mg/liter). Unlike metallic gold, FG remains dispersed even at concentrations up to 50% by weight. This is useful specially for coating applications wherein FG nanoparticles can be coated on a substrate in a dispersed state. After the coating process, FG NPs can be reduced to

metallic gold by either using a reducing agent or by increasing the temperature of the substrate up to few hundred degrees centigrade.

Nonplasmonic MDT nanoparticles need to be further optimized with respect to their heating and fluorescence efficiency. Several metalonaphthalocyanine dyes can be chosen carefully (based on their absorbance) such that the quenching of fluorescence is minimized. Further, different methods for the delivery of hydrophilic as well as hydrophobic drugs, using MDT nanoparticles, should be explored. The photodynamic property of encapsulated dyes in MDT nanoparticles needs to be characterized/quantified using EPR (electron paramagnetic resonance) or fluorescence methods.

In the recent past attempts have been made to integrate fluorescence imaging with other imaging modalities synergistically to enable better diagnosis and help plan for effective therapeutic strategies. Combining the anatomical resolution of MRI with the sensitivity of optical imaging is highly desired and could prove to be a powerful technique for finding and quantifying the size of tumors, especially tumors or metastases that are too small to be detected by MRI alone. Multifunctional nanoparticles developed in this work can be incorporated with MR contrast agents such as iron oxide nanoparticles or gadolinium-chelates. Internally gold-speckled-silica (IGSS) nanoparticles are suitable for the incorporation of 2-3 nm size iron oxide nanoparticles along with the gold nanoparticles. Further, silica matrix of GSS, IGSS, and MDT nanoparticles can be used to incorporate Gd-chelate based contrast agents. In addition, Mn and Fe naphthalocyanine dyes can be incorporated in MDT nanoparticles to potentially provide heating as well as MR contrast.

The *in vivo* targeting efficiency of multifunctional nanoparticles should be studied by utilizing the bioconjugation protocols (e.g. biotin-avidin chemistry) such as developed for TEM8 targeting. The fate and transport of these nanoparticles for *in vivo* applications needs to be further studied using fluorescence property for semi-quantitative analysis and gold (ICP) for quantitative analysis. Specifically, the biodistribution and blood clearance behavior of MNPs in rat model should be carried out using aforementioned analytical techniques. The biodistribution should be studied by quantifying the particle contents in following organs: liver, spleen, lung, kidney and tumor. Blood clearance behavior can be quantified by measuring the blood half life time of the particles. These two parameters are essential in establishing and understanding the particokinetic behavior of MNPs in an *in vivo* environment.

LIST OF REFERENCES

- (1) Etzioni, R.; Urban, N.; Ramsey, S.; McIntosh, M.; Schwartz, S.; Reid, B.; Radich, J.; Anderson, G.; Hartwell, L. *Nature Reviews Cancer* **2003**, *3*, 243.
- (2) Choi, Y. E.; Kwak, J. W.; Park, J. W. *Sensors*, *10*, 428.
- (3) Sharrna, P.; Brown, S.; Walter, G.; Santra, S.; Moudgil, B. *Advances In Colloid And Interface Science* **2006**, *123*, 471.
- (4) Gindy, M. E.; Prud'homme, R. K. *Expert Opinion On Drug Delivery* **2009**, *6*, 865.
- (5) McCarthy, J. R.; Weissleder, R. *Advanced Drug Delivery Reviews* **2008**, *60*, 1241.
- (6) Sanvicens, N.; Marco, M. P. *Trends In Biotechnology* **2008**, *26*, 425.
- (7) Sevick-Muraca, E. M.; Rasmussen, J. C. *Journal Of Biomedical Optics* **2008**, *13*.
- (8) Weissleder, R. *Science* **2006**, *312*, 1168.
- (9) Massoud, T. F.; Gambhir, S. S. *Genes and Development* **2003**, *17*, 545.
- (10) Prasad, P. N. *Biophotonics*; 1 ed.; Wiley-Interscience, 2003.
- (11) Hilderbrand, S. A.; Weissleder, R. *Current Opinion In Chemical Biology* **2010**, *14*, 71.
- (12) Mansfield, J. R. *Current Pharmaceutical Biotechnology* **2010**, *11*, 628.
- (13) Ghoroghchian, P. P.; Therien, M. J.; Hammer, D. A. *Wiley Interdisciplinary Reviews-Nanomedicine And Nanobiotechnology* **2009**, *1*, 156.
- (14) Bremer, C.; Ntziachristos, V.; Mahmood, U.; Tung, C. H.; Weissleder, R. *Radiologe* **2001**, *41*, 131.
- (15) Weissleder, R. *Nature Biotechnology* **2001**, *19*, 316.
- (16) Hilderbrand, S. A.; Weissleder, R. *Current Opinion In Chemical Biology*, *14*, 71.
- (17) Ntziachristos, V.; Bremer, C.; Weissleder, R. *European Radiology* **2003**, *13*, 195.
- (18) Bringley, J. F.; Penner, T. L.; Wang, R. Z.; Harder, J. F.; Harrison, W. J.; Buonemani, L. *Journal Of Colloid And Interface Science* **2008**, *320*, 132.
- (19) Pelley, J. L.; Daar, A. S.; Saner, M. A. *Toxicological Sciences* **2009**, *112*, 276.
- (20) Hardman, R. *Environmental Health Perspectives* **2006**, *114*, 165.

- (21) Yao, G.; Wang, L.; Wu, Y. R.; Smith, J.; Xu, J. S.; Zhao, W. J.; Lee, E. J.; Tan, W. H. *Analytical And Bioanalytical Chemistry* **2006**, 385, 518.
- (22) Burns, A. A.; Vider, J.; Ow, H.; Herz, E.; Penate-Medina, O.; Baumgart, M.; Larson, S. M.; Wiesner, U.; Bradbury, M. *Nano Letters* **2009**, 9, 442.
- (23) Santra, S.; Dutta, D.; Moudgil, B. M. *Food and Bioproducts Processing* **2005**, 83, 136.
- (24) Santra, S.; Wang, K. M.; Tapeç, R.; Tan, W. H. *Journal Of Biomedical Optics* **2001**, 6, 160.
- (25) Altinođlu, E. İ.; Russin, T. J.; Kaiser, J. M.; Barth, B. M.; Eklund, P. C.; Kester, M.; Adair, J. H. *ACS Nano* **2008**, 2, 2075.
- (26) Lee, C. H.; Cheng, S. H.; Wang, Y. J.; Chen, Y. C.; Chen, N. T.; Souris, J.; Chen, C. T.; Mou, C. Y.; Yang, C. S.; Lo, L. W. *Advanced Functional Materials* **2009**, 19, 215.
- (27) Jain, P. K.; Huang, X.; El-Sayed, I. H.; El-Sayed, M. A. *Acc Chem Res* **2008**, 41, 1578.
- (28) Hu, M.; Chen, J. Y.; Li, Z. Y.; Au, L.; Hartland, G. V.; Li, X. D.; Marquez, M.; Xia, Y. N. *Chemical Society Reviews* **2006**, 35, 1084.
- (29) Loo, C.; Lin, A.; Hirsch, L.; Lee, M. H.; Barton, J.; Halas, N. J.; West, J.; Drezek, R. *Technology In Cancer Research & Treatment* **2004**, 3, 33.
- (30) Kang, J.; Yang, J.; Lee, J.; Oh, S. J.; Moon, S.; Lee, H. J.; Lee, S. C.; Son, J. H.; Kim, D.; Lee, K.; Suh, J. S.; Huh, Y. M.; Haam, S. *Journal Of Materials Chemistry* **2009**, 19, 2902.
- (31) Kim, J. W.; Galanzha, E. I.; Shashkov, E. V.; Moon, H. M.; Zharov, V. P. *Nature Nanotechnology* **2009**, 4, 688.
- (32) Lu, W.; Xiong, C. Y.; Zhang, G. D.; Huang, Q.; Zhang, R.; Zhang, J. Z.; Li, C. *Clinical Cancer Research* **2009**, 15, 876.
- (33) von Maltzahn, G.; Centrone, A.; Park, J. H.; Ramanathan, R.; Sailor, M. J.; Hatton, T. A.; Bhatia, S. N. *Advanced Materials* **2009**, 21, 3175.
- (34) Lal, S.; Clare, S. E.; Halas, N. J. *Accounts Of Chemical Research* **2008**, 41, 1842.
- (35) Kim, J.; Piao, Y.; Hyeon, T. *Chemical Society Reviews* **2009**, 38, 372.
- (36) Jarzyna, P. A.; Gianella, A.; Skajaa, T.; Knudsen, G.; Deddens, L. H.; Cormode, D. P.; Fayad, Z. A.; Mulder, W. J. M. *Wiley Interdisciplinary Reviews: Nanomedicine and Nanobiotechnology* **2010**, 2, 138.

- (37) Adisheshaiah, P. P.; Hall, J. B.; McNeil, S. E. *Wiley Interdisciplinary Reviews: Nanomedicine and Nanobiotechnology* **2009**, *2*, 99.
- (38) McNeil, S. E. *Wiley Interdisciplinary Reviews: Nanomedicine and Nanobiotechnology* **2009**, *1*, 264.
- (39) Sharma, P.; Brown, S. C.; Singh, A.; Iwakuma, N.; Pyrgiotakis, G.; Krishna, V.; Knapik, J. A.; Barr, K.; Moudgil, B. M.; Grobmyer, S. R. *Journal Of Materials Chemistry* **2010**, *20*, 5182.
- (40) Altinoğlu, E. İ.; Adair, J. H. *Wiley Interdisciplinary Reviews: Nanomedicine and Nanobiotechnology* **2010**, *Early View*.
- (41) He, X.; Wang, K.; Cheng, Z. *Wiley Interdisciplinary Reviews: Nanomedicine and Nanobiotechnology* **2010**, *2*, 349.
- (42) Huang, X. H.; Jain, P. K.; El-Sayed, I. H.; El-Sayed, M. A. *Lasers In Medical Science* **2008**, *23*, 217.
- (43) Lapotko, D. *Nanomedicine* **2009**, *4*, 813.
- (44) Jain, P. K.; Huang, X. H.; El-Sayed, I. H.; El-Sayed, M. A. *Accounts Of Chemical Research* **2008**, *41*, 1578.
- (45) Longmire, M.; Choyke, P. L.; Kobayashi, H. *Nanomedicine* **2008**, *3*, 703.
- (46) Choi, H. S.; Liu, W.; Misra, P.; Tanaka, E.; Zimmer, J. P.; Ipe, B. I.; Bawendi, M. G.; Frangioni, J. V. *Nature Biotechnology* **2007**, *25*, 1165.
- (47) Arnida; Malugin, A.; Ghandehari, H. *Journal Of Applied Toxicology*, *30*, 212.
- (48) Chithrani, B. D.; Ghazani, A. A.; Chan, W. C. W. *Nano Letters* **2006**, *6*, 662.
- (49) Jiang, W.; Kim, B. Y. S.; Rutka, J. T.; Chan, W. C. W. *Nature Nanotechnology* **2008**, *3*, 145.
- (50) Resch-Genger, U.; Grabolle, M.; Cavaliere-Jaricot, S.; Nitschke, R.; Nann, T. *Nature Methods* **2008**, *5*, 763.
- (51) Jiang, S.; Gnanasammandhan, M. K.; Zhang, Y. *Journal Of The Royal Society Interface* **2010**, *7*, 3.
- (52) Jin, Y. D.; Gao, X. H. *Nature Nanotechnology* **2009**, *4*, 571.
- (53) Bawa, R. *Nanotechnology Law and Business* **2008**, *5*, 135.
- (54) Santra, S.; Tapeç, R.; Theodoropoulou, N.; Dobson, J.; Hebard, A.; Tan, W. H. *Langmuir* **2001**, *17*, 2900.

- (55) Zhao, X. J.; Bagwe, R. P.; Tan, W. H. *Advanced Materials* **2004**, *16*, 173.
- (56) Bagwe, R. P.; Yang, C. Y.; Hilliard, L. R.; Tan, W. H. *Langmuir* **2004**, *20*, 8336.
- (57) Arriagada, F. J.; Osseasare, K. *Colloids And Surfaces* **1992**, *69*, 105.
- (58) Kishida, M.; Tago, T.; Hatsuta, T.; Wakabayashi, K. *Chemistry Letters* **2000**, 1108.
- (59) Arriagada, F. J.; Osseo-Asare, K. *Journal Of Colloid And Interface Science* **1999**, *211*, 210.
- (60) Arriagada, F. J.; Osseo-Asare, K. *Colloids And Surfaces A-Physicochemical And Engineering Aspects* **1999**, *154*, 311.
- (61) Osseo-Asare, K.; Arriagada, F. J. *Journal Of Colloid And Interface Science* **1999**, *218*, 68.
- (62) Arriagada, F. J.; Osseoasare, K. *Colloid Chemistry Of Silica* **1994**, *234*, 113.
- (63) Pileni, M. P. *Journal Of Physical Chemistry* **1993**, *97*, 6961.
- (64) Petit, C.; Lixon, P.; Pileni, M. P. *Journal Of Physical Chemistry* **1993**, *97*, 12974.
- (65) Taleb, A.; Petit, C.; Pileni, M. P. *Chemistry Of Materials* **1997**, *9*, 950.
- (66) Dutta, P. K.; Jakupca, M.; Reddy, K. S. N.; Salvati, L. *Nature* **1995**, *374*, 44.
- (67) Stober, W.; Fink, A.; Bohn, E. *Journal Of Colloid And Interface Science* **1968**, *26*, 62.
- (68) Lin, H. P.; Mou, C. Y. *Accounts Of Chemical Research* **2002**, *35*, 927.
- (69) Wang, J.; Liu, G. D.; Lin, Y. H. *Small* **2006**, *2*, 1134.
- (70) Bergen, J. M.; Von Recum, H. A.; Goodman, T. T.; Massey, A. P.; Pun, S. H. *Macromolecular Bioscience* **2006**, *6*, 506.
- (71) Weissleder, R.; Pittet, M. J. *Nature* **2008**, *452*, 580.
- (72) Lee, H.; Mason, J. C.; Achilefu, S. *Journal Of Organic Chemistry* **2006**, *71*, 7862.
- (73) Bertolino, C. A.; Caputo, G.; Barolo, C.; Viscardi, G.; Coluccia, S. *J Fluoresc* **2006**, *16*, 221.
- (74) Peng, X. J.; Song, F. L.; Lu, E.; Wang, Y. N.; Zhou, W.; Fan, J. L.; Gao, Y. L. *Journal Of The American Chemical Society* **2005**, *127*, 4170.
- (75) Berezin, M. Y.; Lee, H.; Akers, W.; Guo, K.; Goiffon, R. J.; Almutairi, A.; Frechet, J. M. J.; Achilefu, S. *Conf Proc IEEE Eng Med Biol Soc* **2009**, *2009*, 114.

- (76) Ma, D. L.; Kell, A. J.; Tan, S.; Jakubek, Z. J.; Simard, B. *Journal Of Physical Chemistry C* **2009**, *113*, 15974.
- (77) Larson, D. R.; Ow, H.; Vishwasrao, H. D.; Heikal, A. A.; Wiesner, U.; Webb, W. W. *Chemistry Of Materials* **2008**, *20*, 2677.
- (78) Ow, H.; Larson, D. R.; Srivastava, M.; Baird, B. A.; Webb, W. W.; Wiesner, U. *Nano Letters* **2005**, *5*, 113.
- (79) Martini, M.; Montagna, M.; Ou, M.; Tillement, O.; Roux, S.; Perriat, P. *Journal Of Applied Physics* **2009**, *106*.
- (80) Nooney, R. I.; McCahey, C. M. N.; Stranik, O.; Guevel, X. L.; McDonagh, C.; MacCraith, B. D. *Analytical And Bioanalytical Chemistry* **2009**, *393*, 1143.
- (81) Rao, A. V.; Sakhare, H. M.; Tamhankar, A. K.; Shinde, M. L.; Gadave, D. B.; Wagh, P. B. *Materials Chemistry And Physics* **1999**, *60*, 268.
- (82) Rasch, M. R.; Sokolov, K. V.; Korgel, B. A. *Langmuir* **2009**, *25*, 11777.
- (83) Shim, C. K. *Drug Metabolism Reviews* **2008**, *40*, 20.
- (84) Ruoslahti, E.; Bhatia, S. N.; Sailor, M. J. *The Journal of Cell Biology* **2010**, *188*, 759.
- (85) Iyer, A. K.; Khaled, G.; Fang, J.; Maeda, H. *Drug Discovery Today* **2006**, *11*, 812.
- (86) Perrault, S. D.; Walkey, C.; Jennings, T.; Fischer, H. C.; Chan, W. C. W. *Nano Letters* **2009**, *9*, 1909.
- (87) Letfullin, R. R.; Joenathan, C.; George, T. F.; Zharov, V. P. *Nanomedicine* **2006**, *1*, 473.
- (88) Khlebtsov, B.; Zharov, V.; Melnikov, A.; Tuchin, V.; Khlebtsov, N. *Nanotechnology* **2006**, *17*, 5167.
- (89) Zharov, V. P.; Kim, J.-W.; Curiel, D. T.; Everts, M. *Nanomedicine* **2005**, *1*, 326.
- (90) Zharov, V. P.; Galitovskaya, E. N.; Johnson, C.; Kelly, T. *Lasers In Surgery And Medicine* **2005**, *37*, 219.
- (91) Preston, T. C.; Signorell, R. *Acs Nano* **2009**, *3*, 3696.
- (92) Norman, T. J.; Grant, C. D.; Magana, D.; Zhang, J. Z.; Liu, J.; Cao, D. L.; Bridges, F.; Van Buuren, A. *Journal Of Physical Chemistry B* **2002**, *106*, 7005.
- (93) Quinten, M.; Kreibig, U. *Surface Science* **1986**, *172*, 557.

- (94) Thomas, K. G.; Barazzouk, S.; Ipe, B. I.; Joseph, S. T. S.; Kamat, P. V. *Journal Of Physical Chemistry B* **2004**, *108*, 13066.
- (95) Chumanov, G.; Sokolov, K.; Gregory, B. W.; Cotton, T. M. *Journal Of Physical Chemistry* **1995**, *99*, 9466.
- (96) Freeman, R. G.; Grabar, K. C.; Allison, K. J.; Bright, R. M.; Davis, J. A.; Guthrie, A. P.; Hommer, M. B.; Jackson, M. A.; Smith, P. C.; Walter, D. G.; Natan, M. J. *Science* **1995**, *267*, 1629.
- (97) Sharma, P.; Brown, S. C.; Bengtsson, N.; Zhang, Q. Z.; Walter, G. A.; Grobmyer, S. R.; Santra, S.; Jiang, H. B.; Scott, E. W.; Moudgil, B. M. *Chemistry of Materials* **2008**, *20*, 6087.
- (98) Haruta, M. *Cattech* **2002**, *6*, 102.
- (99) Homberger, M.; Simon, U. *Philosophical Transactions Of The Royal Society A-Mathematical Physical And Engineering Sciences*, *368*, 1405.
- (100) Grabar, K. C.; Smith, P. C.; Musick, M. D.; Davis, J. A.; Walter, D. G.; Jackson, M. A.; Guthrie, A. P.; Natan, M. J. *Journal Of The American Chemical Society* **1996**, *118*, 1148.
- (101) Anker, J. N.; Hall, W. P.; Lyandres, O.; Shah, N. C.; Zhao, J.; Van Duyne, R. P. *Nature Materials* **2008**, *7*, 442.
- (102) Bond, G. C.; Thompson, D. T. *Catalysis Reviews-Science And Engineering* **1999**, *41*, 319.
- (103) Sato, T.; Brown, D.; Johnson, B. F. G. *Chemical Communications* **1997**, 1007.
- (104) Andres, R. P.; Bielefeld, J. D.; Henderson, J. I.; Janes, D. B.; Kolagunta, V. R.; Kubiak, C. P.; Mahoney, W. J.; Osifchin, R. G. *Science* **1996**, *273*, 1690.
- (105) Westcott, S. L.; Oldenburg, S. J.; Lee, T. R.; Halas, N. J. *Langmuir* **1998**, *14*, 5396.
- (106) Pillai, V.; Kumar, P.; Hou, M. J.; Ayyub, P.; Shah, D. O. *Advances In Colloid And Interface Science* **1995**, *55*, 241.
- (107) Capek, I. *Advances In Colloid And Interface Science* **2004**, *110*, 49.
- (108) Groger, H.; Gyger, F.; Leidinger, P.; Zurmuhl, C.; Feldmann, C. *Advanced Materials* **2009**, *21*, 1586.
- (109) Uskokovic, V.; Drogenik, M. *Surface Review And Letters* **2005**, *12*, 239.
- (110) Herrera, A. P.; Resto, O.; Briano, J. G.; Rinaldi, C. *Nanotechnology* **2005**, *16*, S618.

- (111) Yao, L.; Xu, G. Y.; Dou, W. L.; Bai, Y. *Colloids And Surfaces A-Physicochemical And Engineering Aspects* **2008**, 316, 8.
- (112) Steinhauser, G.; Evers, J.; Jakob, S.; Klapotke, T. M.; Oehlinger, G. *Gold Bulletin* **2008**, 41, 305.
- (113) Lu, F.; Wu, S. H.; Hung, Y.; Mou, C. Y. *Small* **2009**, 5, 1408.
- (114) Yelin, D.; Oron, D.; Thiberge, S.; Moses, E.; Silberberg, Y. *Optics Express* **2003**, 11, 1385.
- (115) Troutman, T. S.; Barton, J. K.; Romanowski, M. *Optics Letters* **2007**, 32, 1438.
- (116) Adler, D. C.; Huang, S. W.; Huber, R.; Fujimoto, J. G. *Optics Express* **2008**, 16, 4376.
- (117) Lim, Y. T.; Cho, M. Y.; Kim, J. K.; Hwangbo, S.; Chung, B. H. *Chembiochem* **2007**, 8, 2204.
- (118) Choi, M. R.; Bardhan, R.; Badve, S.; Nakshatri, H.; Halas, N. J.; Clare, S. E. *Cancer Research* **2009**, 69, 860S.
- (119) Choi, M. R.; Stanton-Maxey, K. J.; Stanley, J. K.; Levin, C. S.; Bardhan, R.; Akin, D.; Badve, S.; Sturgis, J.; Robinson, J. P.; Bashir, R.; Halas, N. J.; Clare, S. E. *Nano Letters* **2007**, 7, 3759.
- (120) Ruoslahti, E.; Bhatia, S. N.; Sailor, M. J. *Journal Of Cell Biology*, 188, 759.
- (121) Dietz, G. P. H.; Bahr, M. *Molecular And Cellular Neuroscience* **2004**, 27, 85.
- (122) Hoffmann, F.; Cornelius, M.; Morell, J.; Froba, M. *Angewandte Chemie-International Edition* **2006**, 45, 3216.
- (123) Sayari, A.; Hamoudi, S. *Chemistry Of Materials* **2001**, 13, 3151.
- (124) Vinu, A.; Hossain, K. Z.; Ariga, K. *Journal Of Nanoscience And Nanotechnology* **2005**, 5, 347.
- (125) Trewyn, B. G.; Slowing, II; Giri, S.; Chen, H. T.; Lin, V. S. Y. *Accounts Of Chemical Research* **2007**, 40, 846.
- (126) Rosenholm, J. M.; Sahlgren, C.; Linden, M. *Nanoscale* **2010**, 2, 1870.
- (127) Slowing, II; Vivero-Escoto, J. L.; Wu, C. W.; Lin, V. S. Y. *Advanced Drug Delivery Reviews* **2008**, 60, 1278.
- (128) Pasqua, L.; Cundari, S.; Ceresa, C.; Cavaletti, G. *Current Medicinal Chemistry* **2009**, 16, 3054.

- (129) Radu, D. R.; Lai, C. Y.; Jeftinija, K.; Rowe, E. W.; Jeftinija, S.; Lin, V. S. Y. *Journal Of The American Chemical Society* **2004**, *126*, 13216.
- (130) Radu, D. R.; Lai, C.-Y.; Lin, V. S. Y. *Abstracts of Papers American Chemical Society* **2004**, *227*, U1440.

BIOGRAPHICAL SKETCH

Amit Singh was born in Uttar Pradesh, India. He came to the United States in August 2005 to pursue doctoral education with an aim to engage in “good research”. He joined the group of Dr. Brij Moudgil in the Materials Science and Engineering Department at the University of Florida. Amit expects to graduate in spring of 2011 and would like to pursue alternative career options.